Modélisation, simulation, optimisation et commande d'un procédé d'évaporation réactive assistée par plasma pour la production de couches minces d'oxyde de zinc

THÈSE

Présentée et soutenue publiquement le 19 novembre 2019

Pour l'obtention du

Doctorat de l'Université de Lorraine

Spécialité : Génie des Procédés et des Produits et des Molécules

Par : Asdrúbal Antonio RAMÍREZ BOTERO

Composition du jury

Repporteurs :	Isabelle PITAULT, LAGEP, Université de Lyon 1
	Caroline GENTRIC, LGPEA, Université de Nantes
Examinateurs :	Abderrazak LALTIFI, LRGP, Université de Lorraine
	Iván Darío GIL, U. Nacional, Bogotá, Colombie
Invite :	Oscar SUAREZ, U. Nacional, Bogotá, Colombie

Laboratoire Réactions et Génie des Procédés – UMR 7274, CNRS – Université de Lorraine

Modeling, simulation, dynamic optimization and control of a plasma assisted reactive evaporation process for preparation of Zinc Oxide (ZnO) thin films

Asdrúbal Antonio Ramírez Botero

Tesis o trabajo de grado presentada(o) como requisito parcial para optar al título de:

Doctor en Ingeniería Química

Directores:

Ph.D. Iván Darío GIL

Ph.D. Razak LATIFI

Coodirector:

Ph.D. Gerardo GORDILLO

líneas de Investigación:

Procesos y materiales

Grupos de Investigación :

Grupo de Procesos Químicos y Bioquímico

Grupo de Materiales semiconductores y Energía Solar

Universidad Nacional de Colombia

Facultad de Ingeniería, Departamento de Ingeniería Química y Ambiental

Bogotá, Colombia

2019

Acknowledgements

I want to express my sincere thanks to my advisors, Dr Razak Latifi from Université de Lorraine, Dr Gerardo Gordillo Guzman from Universidad Nacional de Colombia and Dr Ivan Dario Gil Guzman from Universidad Nacional de Colombia, who throughout this time has guided me with patience, motivation and knowledge to make possible the culmination of this work. This work was developed under joint supervision by Universidad Nacional de Colombia and Université de Lorraine. Part of the work was carry out in the Semiconductor Materials And solar energy research group at Universidad Nacional de Colombia and the other part Laboratoire Réactions et Génie des Procédés (LRGP) at Université de Lorraine, I would like to express my gratitude to the team of those groups for their hospitality.

Also I want to acknowledge to Campus France, Colciencias and the School of Engineering of Universidad Nacional for their financial assistance, in the different stage of process.

Finally, I want to say tanks to my family for their love, inspiration, support and understanding during the time I had expend to complete this doctoral degree.

Asdrubal Ramirez Botero, June 2019

Nomenclature

v_r	velocity in the r-direction []
v_z	velocity in the z-direction []
r	radial coordinate [m]
r_t	radius of the reactor [m]
z	axial coordinate [m]
L	distance between the lower electrode and the substrate [m]
L_1	distance between the two electrodes [m]
ρ	density of the plasma (constant) [kg cm^{-3}]
P	Pressure [mbar]
v	kinematic viscosity
μ	viscosity of the plasma [kg s^{-2} cm^{-1}]
$V_{w,Zn}$	Zinc Velocity [$\text{Å}/\text{s}$]
V_{w,O_2}	Oxygen Velocity [cm/min]
Re_w	Reynolds number [-]
Q	volumetric flow [cm^3/min]
n_{eo}	is the maximum electron density
C_i	concentration of each species [mol/ m^3]
k_j	is the rate constant of the reaction [s^{-1} cm^3]
D_i	diffusion coefficient [cm^2 s^{-1}]
R_{dep}	Deposition rate
ρ_{ZnO}	Zinc oxide density
s_i	sticking probability
ρ	Resistivity
T	Transmittance
I	Ionization current
$\Phi_{T\rho}$	quality criterion

SCZ	Space Charge Zone
PV	Photovoltaic Device
CIGS	Cu(In,Ga)Se2
CBD	Chemical Bath Deposition
CVD	Chemical Vapor Deposition
PARE	Plasma Assited Reactive Evaporation
ETL	Electron Transpor Layer
DC	Direct Current
RF	Radio Frequency
HTM	Hole Transport Material
GD	Glow Discharge
VI	Virtual Instrument
ADI	Alternative Direction Implicit
FDM	Finite Difference Method
PMP	
BCI	Boundary Condition Iteration
CVI	Control Vector Iteration
TPBVP	Two-Point Boundary Value Problem
NLP	Non Linear Programing
CVP	Control Vector Parametrization

RÉSUMÉ

Dans ce travail, la modélisation, la simulation, l'optimisation dynamique et le contrôle d'un processus d'évaporation réactif assisté par plasma (PARE) pour le dépôt de couches minces d'oxyde de zinc (ZnO) sont proposés. Initialement, un modèle dimensionnel à l'état instable a été développé pour le processus. Ce modèle applique des équilibres dynamiques des matériaux au processus et tient compte du transfert de masse par diffusion et convection, ainsi que des réactions en masse et en surface, afin de déterminer l'évolution temporelle de la concentration de l'espèce ($O_{2(g)}$, $O_{(g)}$, $O^{-}_{(g)}$, $Zn_{(g)}$, $Zn^{+}_{(g)}$ and $ZnO_{(g)}$) présente dans l'ensemble du réacteur et calcule l'épaisseur finale du film. Le cas d'étude correspond à un réacteur pilote exploité par le groupe de recherche sur les matériaux semi-conducteurs et l'énergie solaire (SM & SE) de l'Université nationale de Colombie, où les couches minces de ZnO sont utilisées pour la fabrication de différents types de cellules solaires (cellules solaires inorganiques inversées, cellules solaires organiques et cellules solaires à base de pérovskite). Les équations sont discrétisées spatialement en utilisant des méthodes de différences finies, puis mises en œuvre et résolues dans le temps en utilisant Matlab®. Les résultats de la simulation sont validés au moyen de COMSOL MULTIPHYSICS® qui calcule les mêmes résultats. Cependant, pour compléter les autres objectifs du projet, il continuera à utiliser la méthode des différences finies sous Matlab® car elle offre plus de flexibilité dans la perspective de l'optimisation dynamique et du contrôle du processus PARE. Pour corroborer le modèle, des mesures expérimentales de l'épaisseur du film de ZnO ont été effectuées à l'aide d'un moniteur d'épaisseur sur un réacteur pilote conçu et mis en œuvre par le groupe de recherche sur les matériaux semi-conducteurs et l'énergie solaire (SM & SE) de l'Université nationale de Colombie. Après 90 minutes de temps de dépôt, les résultats simulés et les mesures expérimentales montrent un très bon accord: une différence d'environ 20 nm autour de l'épaisseur finale du film mince, montrant ainsi la grande précision du modèle développé. Le problème d'optimisation dynamique est transformé en un problème de programmation non linéaire (PNL) à l'aide du procédé CVP, c'est-à-dire que les variables de contrôle sont approximées à l'aide de fonctions constantes par morceaux. Il est ensuite implémenté dans Matlab et résolu à l'aide de fmincon optimizer. Deux problèmes d'optimisation différents sont proposés. Dans le premier problème, le débit de Zn ($V_{w,Zn}$) est considéré comme une variable de contrôle ou manipulée $u(t)$ et dans le deuxième problème, le débit de Zn ($V_{w,Zn}$) et le débit d'oxygène (V_{w,O_2}) sont considérés comme des variables manipulées. Les contraintes de qualité sont établies en fonction des études expérimentales réalisées afin de déterminer les propriétés du produit final telles que la transmittance, la résistivité, l'épaisseur du film et les paramètres du réacteur.

Deux problèmes d'optimisation sont résolus en prenant comme variable de contrôle le débit de Zn et le débit d'oxygène afin de minimiser le temps de traitement par lot, tandis que certaines propriétés souhaitées du film mince (transmittance, résistivité et épaisseur) satisfont aux contraintes définies. Le temps de traitement par lot a été réduit de 15% par rapport aux conditions de fonctionnement actuelles du groupe de recherche sur les matériaux semi-conducteurs et l'énergie solaire. Enfin, les profils optimaux du débit de Zn et du débit d'oxygène obtenus dans la partie optimisation ont été utilisés pour développer et simuler un algorithme de contrôle réglementaire à l'aide de la boîte à outils Simulink de Matlab®. Les résultats obtenus dans la simulation de l'algorithme de contrôle montrent que le contrôleur conçu a une performance appropriée en suivant les trajectoires d'écoulement optimales et le rapport idéal Oxygène / Zinc.

Abstract

In this work the modeling, simulation, dynamic optimization and control of a Plasma Assisted Reactive Evaporation process (PARE) for the deposition of Zinc Oxide (ZnO) thin films are proposed. Initially, a dimensional unsteady-state model was developed for the process, this model apply dynamic material balances to the process and accounting for diffusive and convective mass transfer, and bulk and surface reactions in order to establish the space-time evolution of the concentration of the species ($O_{2(g)}$, $O_{(g)}$, $O^{-}_{(g)}$, $Zn_{(g)}$, $Zn^{+}_{(g)}$ and $ZnO_{(g)}$) present throughout the reactor and compute the final film thickness. The case of study corresponds to a pilot reactor operated by the Semiconductor Materials and Solar Energy Research Group (SM&SE) of the Universidad Nacional de Colombia where the ZnO thin films are used for the fabrication of different kind of solar cells (inverted inorganic solar cells, organic solar cells and perovskite based solar cells). The equations are spatially discretized using finite difference methods and then implemented and solved in time using Matlab®. The simulation results are validated by means of COMSOL MULTIPHYSICS® which computes the same results; However, to complete the others objectives of the project it will keep using the finite difference method under Matlab® because it offers more flexibility in the perspective of dynamic optimization and control of PARE process. To corroborate the model, experimental measurements of ZnO film thickness were carried out using a thickness monitor on a pilot reactor designed and implemented by the Semiconductor Materials and Solar-Energy (SM&SE) Research Group at Universidad Nacional de Colombia. After 90 min of deposition time the simulated results and the experimental measurements exhibit a very good agreement, just around 20 nm discrepancy in the final thin film thickness hence showing the high accuracy of the developed model. The dynamic optimization problem is transformed into a non-linear programming (NLP) problem using the CVP method, i.e. the control variables are approximated by means of piecewise constant functions. It is then implemented within Matlab and solved using *fmincon* optimizer. Two different optimization problems are proposed., in the first problem Zn flow rate ($V_{w,Zn}$) is considered as control or manipulated variables $u(t)$ and in the second problem both Zn flow rate ($V_{w,Zn}$) and Oxygen flow rate (V_{w,O_2}) are considered as manipulated variables. Quality constraints are established according to experimental studies that were performed in order to determinate the final product properties such as Transmittance, Resistivity, Film thickness and reactor parameters.

Two optimization problems are solved taking as control variable the Zn flow rate and Oxygen flow rate in order to minimize batch time while some thin film desired properties (transmittance, resistivity and thickness) satisfy the defined constraints. The batch time was reduced in a 15% with respect to the current operating conditions used by the Semiconductor Materials and Solar Energy research Group. Finally, the optimal profiles of the Zn flow rate and Oxygen flow rate that were obtained in the optimization part were used to develop and

simulated a regulatory control algorithm using the Simulink toolbox of Matlab®. The results obtained in the simulation of the control algorithm show that the designed controller has an appropriate performance by following the optimal flow trajectories and the ideal ratio of Oxygen and Zinc.

Keywords: modeling, simulation, advance regulatory control, dynamic optimization, ZnO thin films

List of Figures

Figure 1.1 Evolution of record efficiencies at the laboratory level obtained from emerging technologies during the last years [46]. 26
Figure 1.2 Evolution over the years of the publications that report the use of ZnO in photovoltaic applications [47]. 27
Figure 1.3 Inorganic CusZnSnS4 based photovoltaic device with ZnO as optical window. 28
Figure 1.4 Arquitecture of conventional hybrid perovskite solar cells. [54] 29
Figure 1.5 Architecture of an organic solar cell including electron transport layers (ETL) and hole transport material (HTL) [56]. 30
Figure 2.1 Shows a scheme of the setup designed and implemented to grow ZnO thin films by plasma assisted reactive evaporation. This includes the following units: 33
Figure 2.2 Block diagram of the control system designed to perform the control of the amount of Zn that arrives to the GD zone. 34
Figure 2.3 Close loop response of partial pressure of chamber in plasma assisted reactive evaporation process. 35
Figure 3.1 Modeling scheme of plasma assisted reactive evaporation process. 38
Figure 3.2 Diagram of the experimental setup used for the measurement of the deposition rate of Zn. 41
Figure 3.3 Simulation of the distribution profile of the concentration of O2. 49
Figure 3.4 Simulation of the distribution profile of the concentration of Zn. 50
Figure 3.5 Simulation of the distribution profile of the concentration of ZnO. 50
Figure 3.6 Experimental and simulated final film thickness profile of a typical ZnO film. The inset shows a Knudsen cell with a design that allows to improve the homogeneity in the thickness of the ZnO films. 51
Figure 3.7 Comparison of the experimental measurements of the thickness of ZnO films prepared by reactive evaporation in dependence of the deposition time, with their corresponding simulated values. 52
Figure 4.1 a) Scheme of the system used to measure resistivity, b) distribution of the four probes. 55
Figure 4.2 Setup of the Varian-Cary 5000 spectrophotometer.[74] 56
Figure 4.3 Variation of resistivity, transmittance (at 700 nm) and merit figure (quality criteria $\boldsymbol{\Phi T \rho}$) of ZnO thin films as a function of the glow discharge ion current. 57
Figure 4.4 Variation of resistivity, transmittance (at 700 nm) and figure of merit (quality criteria $\boldsymbol{\Phi T \rho}$) of ZnO thin films as a function of O2-flow. 58
Figure 4.5 Variation of resistivity, transmittance (at 700 nm) and figure of merit (quality criteria $\boldsymbol{\Phi T \rho}$) of ZnO thin films as a function of Zn-flow. 59
Figure 4.6 Spectral transmittance of a typical sample of ZnO, deposited under optimal conditions. 61
Figure 5.1 Example of different types of piecewise controls 69
Figure 5.2 Typical profiles of the Knudsen cell temperature and the partial pressure change DP that allow depositing ZnO with thicknesses, transmittances and resistivities suitable to be used as optical window of solar cells. 72
Figure 5.3 Optimal Zn flow profile for the time minimization 74
Figure 5.4 Optimal Zn flow profile for the time minimization 76
Figure 5.5 Optimal Zn flow profile for the time minimization 77
Figure 6.1 Conceptual diagram for regulatory control (Method I) [90]. 80
Figure 6.2 Conceptual diagram for regulatory control (Method II) [90]. 81

Figure 6.3 Open and closed loop systems [92]. 82
Figure 6.4 First order systems response [93]. 84
Figure 6.5 Second order system response [93]. 85
Figure 6.6 Unit feedback system. Plant: system to control. Controller: Provides the excitement of the plant; It is designed to control the behavior of the entire system. 87
Figure 6.7 Schematic representation of the simulation RC control of the of Plasma Assisted Reactive Evaporation reactor. 88
Figure 6.8 Knudsen cell open loop response. 89
Figure 6.9 (a) Zn flow rate control for the optimal profile in the orange line the Zn flow set point and in the blue line the Zn flow rate reactor values, (b) the optimal oxygen flow rate (c) Manipulated variable (current of the Knudsen cell). 90
Figure 6.10 (a) Zn flow rate control for the optimal profile in the orange line the Zn flow set point and in the blue line the Zn flow rate reactor values, with 10% of the introduction error (b)flow rate of oxygen affected by the advance regulatory control keeping 91

List of Tables

Table 3.1 PARE reactor parameters. 408
Table 3.2 Values of deposition rate of Zn as a function of the Knudsen cell temperature. 38
Table 3.3 Reaction rate constants for the equations 11 to 16. 486
Table 3.4 Diffusion coefficients and initial concentration for each species. 486
Table 5.1 – Optimization results for time minimization using as a control variable Zn flow rate. 731
Table 5.2 Optimization results for time minimization using as a control variables Zn flow rate and oxygen flow rate. 754

Contents

Introduction 20

Outline of the thesis 23

Chapter 1 25

Solar Energy Technology 25

1.1 State of the art of photovoltaic solar technology 25

1.2 Architecture of solar cells based on emerging materials 27

1.2.1 Inorganic solar cells 27

1.2.2 Solar cells based on hybrid organic-inorganic compounds with perovskite structure 28

1.2.3 Organic solar cells 29

Chapter 2 31

Plasma Assisted Reactive Evaporation Process 31

2.1 Kinetics and mechanisms 31

2.2 Reactor engineering 32

2.1.3 Operation conditions 34

Chapter 3 37

Modeling and simulation of Plasma Assisted Reactive Evaporation process 37

3.1 Process description and modeling 38

3.1.1 Flow Field 39

3.1.2 Reactions, mass transport and thin film deposition 41

3.1.3 Reactions, mass transport and thin film deposition 42

3.2 Simulation of a Plasma Assisted Reactive Evaporation process 44

3.1.1 The Finite Difference Method (FDM) 45

3.2.2 Construction of a discretization scheme using ADI method 47

3.3.3 Simulation results 48

Chapter 4 54

Opto-electrical Characterization of ZnO thin films prepared using Plasma Assisted Reactive Evaporation process 54

4.1 Thin film characterization fundamentals 54

4.1.1 Electric Characterization 55

4.1.2 Optical characterization 56

4.2 Influence of deposition conditions on transmittance and resistivity 57

4.2.1 Influence of the ion current of the glow discharge 57

4.2.2 Influence of the oxygen flow 58
4.2.3 Influence of the Zn flow 59
Chapter 5 62
Dynamic optimization and control of Plasma Assisted Reactive Evaporation process 62
5.2 Dynamic optimization fundamentals 63
5.1 Problem definition 63
5.1.1 Analytical methods 65
5.1.2 Numerical methods 66
5.2 Dynamic optimization of Plasma Assisted Reactive Evaporation process 69
5.2.1 Case study: plasma assisted reactive evaporation process 70
5.2.2 Operating conditions: plasma assisted reactive evaporation process 71
5.2.3 Batch time minimization with Zn flow as control variable 72
5.2.4 Batch time minimization with Zinc flow and 0xygen flow as control variables 75
Chapter 6 79
Regulatory Control of Plasma Assisted Reactive Evaporation process 79
6.1 Feedback effects 82
6.2 Modeling and Identification 83
i) First Order Systems 83
ii) Second Order Systems 85
6.3 PID controller 86
6.4 Control simulation of Plasma Assisted Reactive Evaporation process 88
Chapter 7 93
Conclusions and perspectives 93
8. References 97

Introduction

Currently, renewable energies are considered as the main alternative for the energy generation in the near future, due to the fact that the primary resource is inexhaustible and that they generate clean energy that does not affect the environment. On the contrary, nuclear energy and hydrocarbons coming from the oil industry, which dominate the world's energy demand, have secondary effects that negatively affect the environment and climate change of the planet. Therefore, the development of technologies that take advantage of renewable energy sources to generate energy is one of the main alternatives to contribute to the future global energy demand. Within renewable energies, solar energy is presented as one of the most promising since it is a source of clean energy, unlimited and easy to use in most of the planet, additionally does not generate greenhouse gases and requires low maintenance costs.

The generation of electric power from solar energy was a discovery attributed to Alexandre Edmund Becquerel in 1839, who from a galvanic battery observed a small increase in electricity generation when it was affected by solar radiation. The first solar cell was built in 1884 by Charles Fritts with an efficiency of 1% using a selenium wafer with gold electrical contacts [1]. Heinrich Hertz in 1887 described the photoelectric effect but it was Albert Einstein who in 1904 gave the theoretical explanation based on the quantum theory recently proposed by Max Planck [2]. Russel Ohl in 1939 made a significant breakthrough with the discovery and analysis of p-n binding, which was called by him "p-n barrier"; This was the basis for the first modern solar cell, called "light sensitive device" [3], which in 1954, DM Chapin, CS Fuller and GL Pearson, researchers from the Bell laboratory, USA, managed to manufacture, becoming the first solar cell of silicon that reached an efficiency of 6% [4].

Since then, research in this area has focused on the search for materials and architectures that allow improving the conversion efficiency achieved by Chapin and collaborators. In 1960, M. Wolf proposed the use of impurities to increase the absorption spectrum of the cell [5]. A year later, William Shockley and Hans Queisser calculated the theoretical limit of the conversion efficiency for solar cells with single-junction architecture for an energy gap of 1.1 eV, this value was 30% [6] and was corroborated in 1984 by Tom Tiedje, Eli Yablonovitch, George D. Cody and Bonnie G. Brooks, who reported that the theoretical limit for the

efficiency of silicon solar cells is 29.8%, [7]. In 1996 Antonio Martí and G. Araujo proposed a new solar cell architecture, called a tandem cell (stacked cells), whose theoretical limit of efficiency for an infinite number of stacked cells is 86.8% [8]. In 1997, a new cell architecture with intermediate band structure was introduced, proposed by Antonio Luque and Antonio Martí, which allows a theoretical limit of efficiency of 63.2% [9].

Zinc oxide (ZnO) is a semi-conductor material used in different applications, including light emitting diodes, flat panel displays and solar cells. The large use of this material is due to its interesting opto-electronic properties such as large exciton binding energy of 60 meV, a wide band gap, low resistivity, and high transparency in the visible region [10–13]. More specifically, ZnO has been extensively studied to be used as conductive and transparent windows layer in kesterite and chalcopyrite based solar cells [14–16] and recently this compound also began to be used as electron selective layer in inverted organic solar cells [17,18] and as electron transport layer in perovskite based hybrid solar cells [19,20].

Different methods have been used to manufacture ZnO films, such as reactive sputtering [21], Radio Frequency (RF) magnetron sputtering [22], chemical bath deposition (CBD) [23], chemical vapor deposition (CVD) [24], spray pyrolysis [25] and sol-gel techniques [26]. Among these methods, the most favorable technique for large area deposition and mass production is the magnetron RF sputtering. Solar cell based on Cu(In,Ga)Se2 has achieved efficiencies up to 21.7% using RF-sputtered ZnO:Al films from ceramic targets [27]. However, the RF sputtering deposition process has cost limitations in large-area manufacturing, associated with the use of ceramic targets. In contrast, ZnO thin films deposited by Plasma Assisted Reactive Evaporation process (PARE) with Zn as the starting material, could become a better alternative than the RF sputtering method, for large-scale production of photovoltaic modules at a lower cost [28]. Additionally this system allows deposition of thin films of both, i-ZnO and n+-ZnO films due the possibility of change the O_2 density vacancies.

The majority of ZnO thin films are manufactured through batch processes in the microelectronics industry, in these cases a systematic methodologies are needed to optimize product quality specifications under tight constraints on the process. The objective of a generic process unit operation is improving manufacturing efficiency while minimizing plant costs [28].

In the semiconductor industry, despite the extensive body of research, there is still a significant discrepancy between the expected performance and the actual yield that can be accomplished employing the current control methodologies [29]. There are, in essence, two major obstacles to close that gap: (a) the lack of practical in-situ sensors that provide real-time, micro-scale measurements for online applications, and (b) uncertainties in the deposition process that are not captured by the prevalent, nominal models [30].

The main motivation of this work has to do with the development of a reactor for depositing thin films of ZnO using a method based on Plasma Assisted Reactive Evaporation Process (PARE), that allows reproducible growth of this compound with optimized opto-electric properties so that it can be used as optical window in solar cells; for that the modeling, simulation, dynamic optimization and control of a the PARE system are proposed. Taking account the advantages that the PARE process present respect to the most common deposition techniques, the efforts on modeling, optimization and control of this process are an important trouble to solve. To achieve the desired performance specifications in the operation of PARE process is required the development of accurate mathematical models that can be used to design optimal reactor and flow arrangements and test the performance of different control systems. The key issue in the development of a mathematical model for PARE processes is the understanding of the physicochemical phenomena complexity, which arises from factors such as glow discharge chemistry, electron density and energy distribution, ion transport, diffusive and convective mass transfer, bulk and deposition reaction kinetics.

The dynamic optimization studies can be directed to determine the optimal profiles of variables like, temperatures, flow rates and pressures for the PARE process that optimize costs, taking into account criteria like: energy, time, productivity and reproducibility; this costs optimization also has to be attached to specific constraints such as model, operating system and thin film qualities. In earlier studies, a PID- PWM control law was developed to enhance the behavior of the PARE process, however the batch time and energy demand of the process still been very high [28]. Then, the solution of the dynamic optimization problem give as a result the optimal profiles that, will be used for the design of the Advance Regulatory control as set points that could achieve a batch time minimization keeping some quality product specifications such as transmittance high that 80%, resistivity less that $1x10^{-3}$ ohm/cm and thickness around 800 nm.

The optimization and control of the PARE process is a difficult task due that complexity of the physico-chemical phenomena involved and sensitivity to disturbances. The main goal in the operation of the PARE process is to use it to manufacture of ZnO thin films which involves frequent and drastic changes in the process variables whereby the design of an adequate control algorithm is required.

For this research thesis the general objective is to build a dynamic model and solve it through simulation in order to apply dynamic optimization and advanced control techniques, that allow improve the performance of a Plasma Assisted Reactive Evaporation pilot reactor for the preparation of Zinc Oxide (ZnO) thin films with adequate properties to be used in solar cells fabrications. To achieve this, four specific objectives were established:

1. *Build and simulate a dynamic model for a Plasma Assisted Reactive Evaporation pilot reactor to represent the operating conditions and to predict the main state variables*.

2. *Determinate by means of dynamic optimization the optimal time profiles of the main process variables of the Plasma Assisted Reactive Evaporation pilot reactor to minimize the batch time of ZnO thin film production, subject to constraints on the final product quality and reactor configuration.*

3. *Establish experimentally the effect of the operation conditions of the reactor on the optoelectric properties of the thin films of ZnO*.

4. *Develop and implement in a simulation level a control strategy for a Plasma Assisted Reactive Evaporation pilot reactor.*

Outline of the thesis

To accomplish the research objectives it was necessary to follow a methodology which is briefly described bellow in order to explain document structure and its relationship the results obtained. A literature review is presented in chapter 2, which includes the research main topics (i.e. modeling of Plasma Assisted Reactive evaporation process, kinetics and mechanisms, dynamic optimization, Advance regulatory control, etc.). The main characteristics of the plasma assisted reactive evaporation process and the introduction of the effect of the main variables have in the process performance.

In Chapter 3 a description and dynamic model development is presented for the Plasma Assisted Reactive Evaporation process used for synthesis and deposition of ZnO thin films. Also are explained in detail the principal considerations and assumptions that were take into account on the model construction. The final part of this chapter, includes the mathematical solution and an experimental validation of the model.

In chapter 4 experimental results are presented. Those experiments were carry out with the goal of determinate the influence of the most important parameters of the process (Ionization current, Zinc flow and Oxygen flow) in the final properties of the ZnO thin film. The obtained information is used to construct an empiric model equation to give additional information at process model developed in chapter 3 and help with the definition of the operating constraints and quality criteria that will be use in the dynamic optimization.

After the complete solution of the dynamic model and the additional information given for the experiments in chapter 4; in chapter 5 a dynamic optimization study is realized. This chapter have two different sections. In the first one, are presented the fundamental concepts of dynamic optimization in order to have information enough to define optimization problems to be solved. In the second section of this chapter, are presented the optimization problems taking as control variables the Zn flow rate and Oxygen flow rate in order to minimize batch time taking into account the thin film desired qualities (transmittance, resistivity and thickness) and

defined constraints. From this chapter optimal profile of the Zn flow-rate is obtained. The first part of Chapter 6 presents a literature review of Advance Regulatory control. The concepts revised are applied in the second part of the chapter in the design and simulation of the Regulatory control where Zn flow and Oxygen flow are keeping in an ideal ratio for Plasma Assisted Reactive Evaporation. Finally, is reported a simulation in closed loop of a control algorithm which follow the optimal profiles calculated by the solution of the dynamic optimization problem in the chapter 5. In the last part of the chapter is applied a robustness tests on the controller in order to know it performance.

In chapter 7 is discuss the future perspectives of the Plasma assisted Reactive evaporation process and the conclusions of this work.

Chapter 1
Solar Energy Technology

1.1 State of the art of photovoltaic solar technology

The solar cell is a device capable of converting sunlight directly into electricity, through the physical phenomenon called photovoltaic effect, which includes the following processes:

1. Formation of electron-hole pairs in the active layers of the device by the excitation of electrons from the valence band to the conduction band as a consequence of the absorption of photons with energies greater or equal than energy band gap E_g of the semiconductor. The generated carriers are free to participate in the electric transport processes.

2. Diffusion of generated carriers towards the edge of the so-called space charge zone (SCZ)

3. Separation of the charge carriers through the internal electric field ($\vec{E}$) generated in the SCZ and then dragging them towards the electrical contacts. The charge carriers that reach the contacts are extracted to the outside of the solar cell through ohmic contacts, thus generating the photocurrent.

The development of photovoltaic generation devices (PV) for terrestrial use and space applications has been carried out using different technologies known as first, second and third generation [31]. The first generation technology includes modules and solar cells manufactured from monocrystalline GaAs and mono and polycrystalline silicon [32]. However, this technology called first generation photovoltaic despite dominating the world market, due to its high conversion efficiencies and high durability, demands a high production cost. The second generation technology that includes devices manufactured with thin film technology, had as main objective the reduction of the manufacturing cost, which was achieved with cells based on amorphous silicon and polycrystalline inorganic materials based on CdTe and Cu(In,Ga)Se_2. Although the world market for solar

modules is dominated by silicon technology, thin film technology has achieved a great development that allows that there is now also a large manufacturing industry of modules manufactured with this technology; in particular modules based on amorphous silicon (a-Si) [33,34], cadmium telluride (CdTe) [35] and Cu (In, Ga) Se2 (CIGS) [36-38].

Currently, the industry of photovoltaic modules manufactured from thin films of CdTe and CIGS has a great limitation on one hand due to the fact that they use toxic materials such as CdTe, and on the other hand high-cost materials which are not abundant in nature such as the In and the Ga. To solve this limitation in thin film technology, have arisen new devices architectures using new materials, among which are solar cells based on Cu_2ZnSnS_4 compounds with a kesterite structure [39,40] dye sensitized solar cells (DSSC) [41], organic solar cells based on conductive polymers [42,43] and solar cells based on metalorganic compounds with crystalline structure type perovskite, which are characterized by low cost and low environmental impact; the last one have had a rapid increase in their conversion efficiency, reaching values close to 26% [44,45].

The current trend in the field of photovoltaic materials and devices is the implementation of strategies to reduce the manufacturing cost of photovoltaic modules; this has been done mainly through the research of new non-toxic materials, low cost and abundant in nature. The evolution of the efficiencies achieved over time for these new technologies (called emerging) can be seen in Figure 1.1.

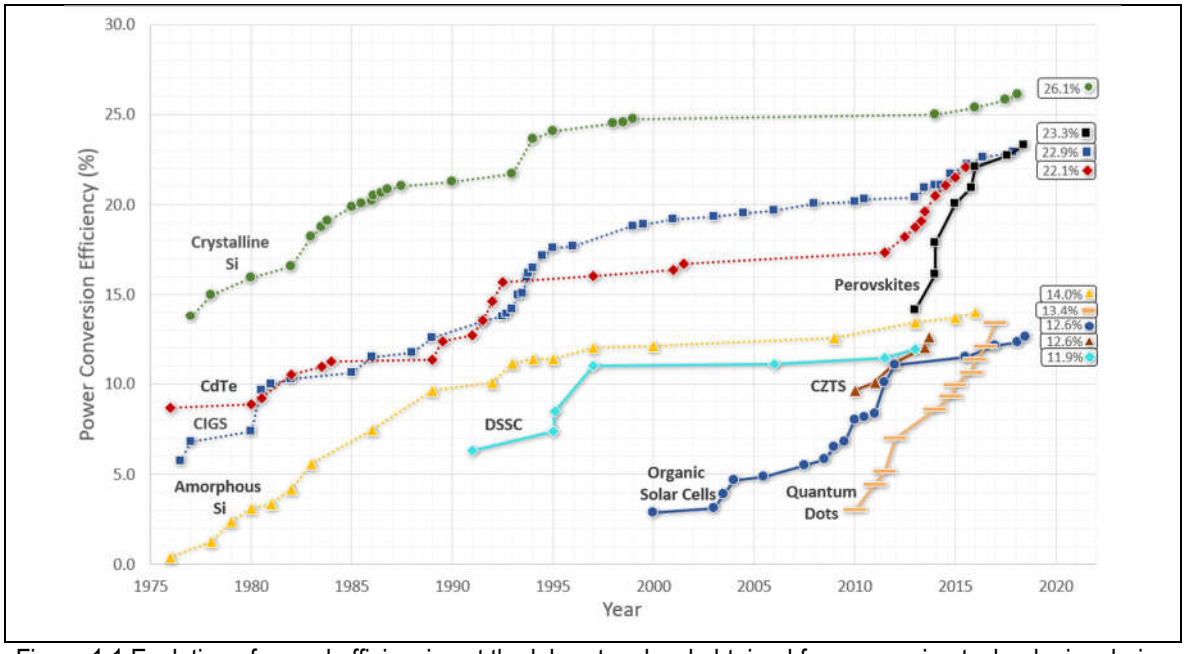

Figure 1.1 Evolution of record efficiencies at the laboratory level obtained from emerging technologies during the last years [46].

Perovskite solar cells have increased in power conversion efficiency at a phenomenal rate compared to other types of photovoltaics. Although this figure only represents lab-based "hero cells", it heralds great promise.

ZnO has been used for a long time in photovoltaic applications due to its unique optical and electrical properties, in particular as a ETL in inorganic, metalorganic and organic solar cells. Figure 1.2 shows the evolution over the years of the publications that report the use of ZnO in photovoltaic applications.

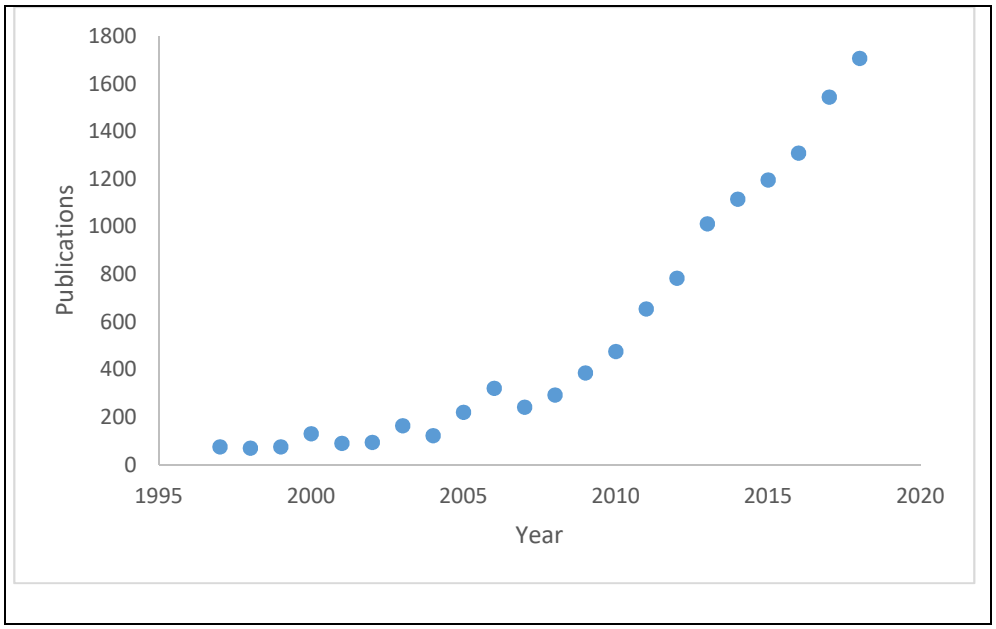

Figure 1.2 Evolution over the years of the publications that report the use of ZnO in photovoltaic applications [47].

ZnO is a semiconductor material of groups II and VI with a bandwidth of 3.2 eV [48,49] which allows it to be used as a ETL in photovoltaic devices. ZnO can grow with three different Zinc structures, Blenda, Rocksalt and wurtzite [48,49].

A wide variety of methods have been used to grow thin films of ZnO with suitable properties to be used for the different applications mentioned above, among which is: CVD, (Chemical Vapor Deposition) [50,51], Direct Current (DC) and RF magnetron sputtering [52,53], Sol-gel spin coating [36], spray pyrolysis [37]. The RF magnetron sputtering method is the most used industrially, however it has some disadvantages such as high production costs and limitation in high deposition areas due to the use of ceramic targets with extrinsic doping. On the other hand the method of Plasma Assisted Reactive Evaporation has greater advantages in terms of costs and greater area of coverage, for this reason developing it at an industrial level would be a great advance in the photovoltaic industry.

1.2 Architecture of solar cells based on emerging materials

1.2.1 Inorganic solar cells

These cells are manufactured with heterojuncion architecture since the n-type material is different from the p-type material. This fact generates discontinuity in the conduction and valence bands, as a consequence of the difference in the gap and in the electronic affinities of the two materials and additionally presence of traps in the interface caused by the differences in the network constant of the two materials .

To reduce the photocurrent losses in heterojunction-type cells, these are manufactured following a concept called optical absorbent-window layer. Figure 1.3 shows the cross-section of a cell with optical absorbent-window layer structure [26].

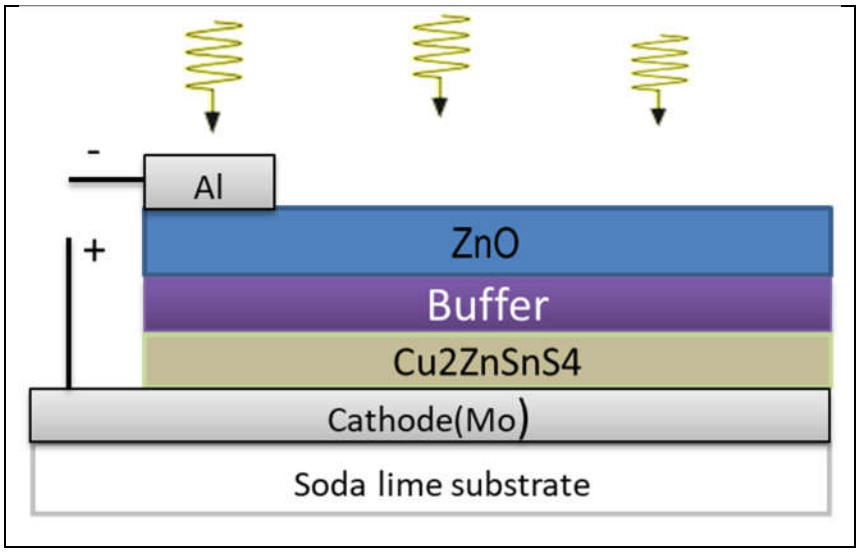

Figure 1.3 Inorganic CusZnSnS4 based photovoltaic device with ZnO as optical window.

The optical window is constituted by the buffer layer and ZnO thin film and its main function is to facilitate that the greater amount of solar radiation reaches the absorbent layer and also to form the electric field in the SCZ that gives rise to the potential difference between the device contacts. In turn, the buffer layer fulfills the function of mechanical coupling between the absorbent layer and the ZnO layer; As the buffer layer has a high absorption coefficient in general, it must be ultrathin (of the order of 60 nm thickness) to achieve a high percentage of radiation reaching the absorbent layer.

1.2.2 Solar cells based on hybrid organic-inorganic compounds with perovskite structure

This type of cell has a new architecture based on the concept of heterojunction; This includes a thin layer of a n-type semiconductor material that acts as an electron transport layer (ETL), a p-type layer that acts as a hole

transport material (HTM) and an active layer of a intrinsic metal-organic material characterized by having a perovskite crystalline structure (see figure 1.4).

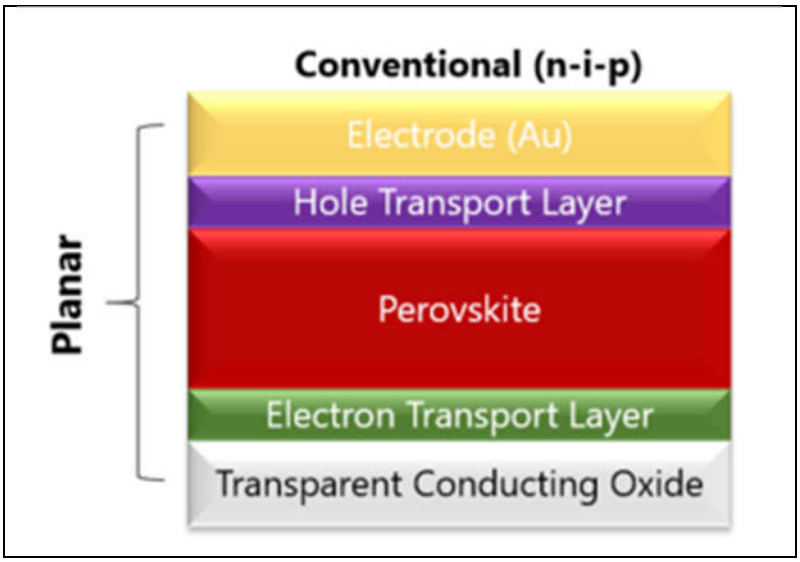

Figure 1.4 Arquitecture of conventional hybrid perovskite solar cells. [54]

The ZnO thin films are generally used as ETL and as Hole Transport Material, P3HT or spiro-MeOTAD; Perovskite is used as the active layer. The highest efficiencies in this type of cells have been achieved with TiO_2, spiro-MeOTAD as ETL and HTM respectively; however this architecture presents low stability caused by the Perovskite degradation in a humid environment and by diffusion processes generated at the interface with TiO_2. For this reason the use of ZnO as ETL is presented as one of the best options for this architecture in its step to industrial level.

1.2.3 Organic solar cells

The organic photovoltaic devices have a different operation than the heterojuncture type inorganic devices.
The photocurrent generation in an organic solar cell follows the following processes [55]:

1. Absorption of radiation by the active layer (constituted by a mixture of donor and acceptor material with domains of the order of 20 nm) and formation of an excited state (exciton).
2. Exciton diffusion, up to the donor-acceptor interface.
3. Dissociation of the exciton by the electric field existing in the SCZ formed near the donor / acceptor junction and generation of free carriers.

4. Carrier drag (holes in the donor material and electrons in the acceptor), induced by the electric field in the area of space charge.
5. Selective transfer of carriers from the active layer to the electrodes.

The photogeneration of electrical current in an organic cell can be improved by the selective transfer of carriers from the active layer to the electrodes; this is achieved by incorporating into the structure of the device selective electron and hole transport layers, between the interfaces active-anode and active-cathode, respectively. Additionally, the ETL allow protection of the active layer, as well as quasi-ohmic contact with the electrodes [56]. In the case of solar cells based on polymers, the best results have been obtained using PEDOT:PSS (poly-ethylenedioxythiophene: polystyrene sulfonic acid) as HTM. While ZnO has been used as ETL. In Figure 1.5 you can see the architecture of this type of cells.

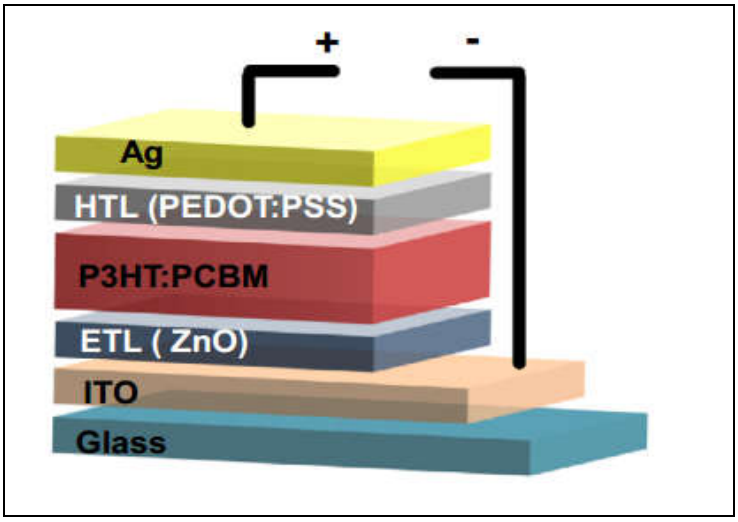

Figure 1.5 Architecture of an organic solar cell including electron transport layers (ETL) and hole transport material (HTL) [56].

Chapter 2
Plasma Assisted Reactive Evaporation Process

2.1 Kinetics and mechanisms

The ZnO thin films are deposited using a route based on the plasma assisted reactive evaporation (PARE), which consists of evaporating Zn in the presence of oxygen, so that there takes place a chemical reaction that gives place to the formation of the ZnO. As the Zn in the presence of O_2 oxidize very slowly at room temperature, it is necessary to ionize both Zn and O_2 to accelerate the chemical reaction between these two species. The ionization is achieved through glow discharge (GD) that includes different ionized species that increase the rate of chemical reaction and therefore the rate of growth of ZnO film. Under the conditions of current and pressure used in the PARE process, the generated plasma is a non-thermal that implies that the most probable mechanism of ionization of the gas inside the plasma is direct ionization of neutral particles (atoms, molecules or radical) by electron impact. Plasma species that do not deposit and unreacted are pumped radially outwards**.** The bias voltage applied between the electrodes to generate the glow discharge induces the following processes:

i) Dissociation of O_2 followed by supply of sufficient energy to ionize the atoms of oxygen present.

ii) When Zn vapor enters into the region of glow discharge can be generated zinc positively ionized species.

iii) Once the precursor species (O and Zn) are ionized, they can be neutralized by binary collision through the process of recombination and removal of ions

iv) Finally the ZnO(g) generated in the plasma is diffused toward the substrate to form the thin film; during this process the ZnO(g) can interact with the plasma and can also be ionized.

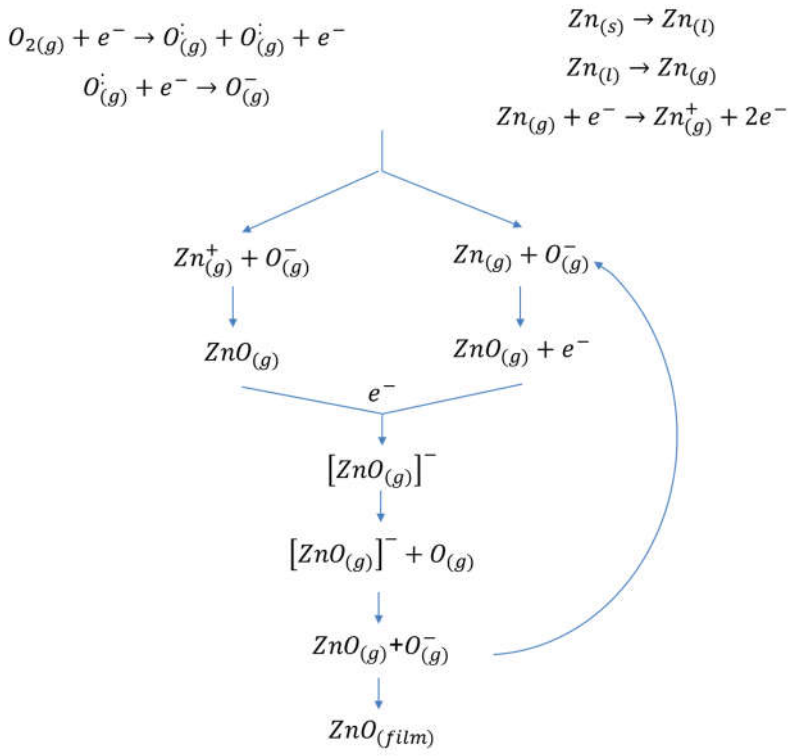

2.2 Reactor engineering

The PARE reactor was designed and developed as result of previous research work and nowadays it is available in the SM&SE laboratory of the Universidad Nacional de Colombia. For the design of the reactor that allows generating a stable GD confined in the space between the electrodes, it took into account the Paschen law that relates the voltage for the initiation of the discharge and the product of the pressure by the separation distance between the electrodes [57]. Fig. 2.1 shows a scheme of the setup to grow ZnO thin films by plasma assisted reactive evaporation. This includes the following units:

(a) Vacuum system, consisting of a mechanical pump and a trap of liquid nitrogen that allows getting a base pressure of 10−4 mbar, prior to the introduction of oxygen.

(b) Reactor where takes place the chemical reaction of precursors (O_2 and Zn) giving rise to the formation of the ZnO. This includes parallel flat electrodes supported by a structure of teflon and a DC power supply (2000 V, 200 mA) regulated in both voltage and current, used to activate the GD (see insert of Fig. 2.1).

(c) Source of evaporation of zinc (effusion Knudsen cell).

(d) Electronic mass flow controller.

(e) Control unit, whose main function is to control the amount of zinc that arrives to the GD zone, which is provided by evaporation from the Knudsen cell. The functions of control, measurement, acquisition, processing and data visualization are made through a virtual instrument developed with LabVIEW. The hardware used includes: the Compact Field Point-1804 module (cFP-1804), who performs the communication with the PC through the RS232 port, an analog input module cFP-TC-120 to acquire the voltage signal from the thermocouple type K used as temperature sensor and an analog input module cFP-AIO-611 to acquire the voltage signal from de Pirani Gauge used as sensor of the change of partial pressure inside the chamber.

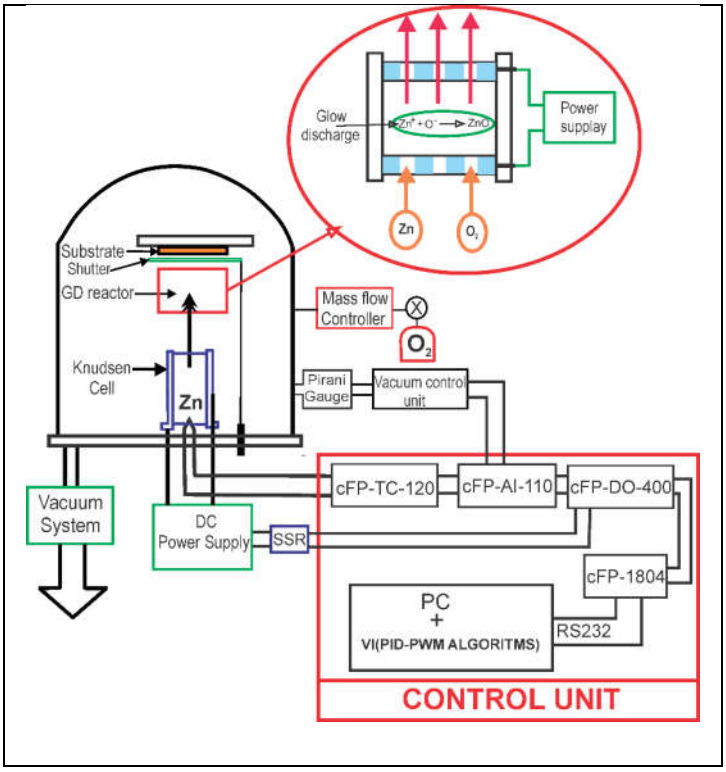

Figure 2.1 Scheme of the setup designed and implemented to grow ZnO thin films by plasma assisted reactive evaporation.

To get conditions to deposit in a reproducibly way ZnO films with thickness, transmittance and resistivity suitable to be used as optical window in solar cells, it is necessary to control very accurately the current of ions of the glow discharge and the flow of both oxygen and zinc that arrives to the area of the plasma. The current of ions generated during the GD and the oxygen introduced into the deposition chamber are controlled with good accuracy using a power supply regulated in current and an electronic flow mass controller, respectively; however, an accurate and reproducible control of the amount of Zn arriving to the GD zone is very difficult to manipulated mainly due to the high vapor pressure of Zn and to the fact that the temperature at which starts

the evaporation of the zinc changes significantly with the room humidity and the moisture absorbed in the walls of the chamber and the electrodes.

Since the amount of Zn arriving to the GD zone is the parameter that most critically affect both the reproducibility and the opto-electrical properties of the ZnO films, it was necessary to develop a tool that allows to do a control it. This was achieved through a virtual instrument (VI) with facilities to control the flow of evaporated Zn. The VI developed include a PID-PWM algorithm to perform the control of the process in two steps, in the first one the temperature ramp of the Knudsen cell is controlled up to reaching a temperature of 400 ◦C using a K-type thermocouple (TC) as sensor. When this temperature is reached, it begins the second step that incorporates a control of the partial pressure (DP) inside the chamber that decreases when Zn starts evaporating and goes in the Glow discharge zone using, in this case a pirani gauge is used as a sensor (PT).

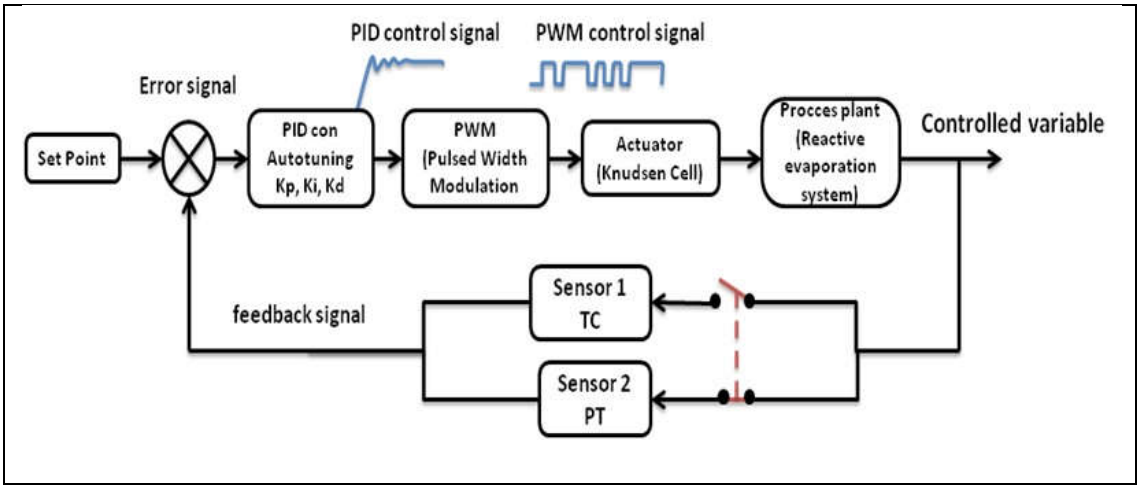

Figure 2.2 Block diagram of the control system designed to perform the control of the amount of Zn that arrives to the GD zone.

2.1.3 Operation conditions

Figure 2.2 shows a block diagram of the control system designed for each of the stages following a schema in closed loop; from the feedback signal generated by the sensors TC and PT is determined the error signal with respect to the desired value (set point); this error signal enters to the PID control algorithm which generates an analog control signal that is modulated by amplitude of pulses through a PWM algorithm. The incorporation of the PWM algorithm was made to be able to control the power of the analog power source used to supply current to the Knudsen cell. The power of this source can only be controlled by varying the frequency of a system on/off.

The effectiveness and reliability of the developed system was verified by obtaining with a reasonable degree of reproducibility of a large number of ZnO thin films with thicknesses, transmittances and resistivities suitable for use as transparent and conductive window layer and as a diffusion barrier in solar cells. However due the Zn intrinsic characteristics, the process has some limitations because the PID-PWM control law implemented cannot stabilize with high precision the partial pressure in the chamber (see Fig.2.3-a) generating long batch times and high materials lost. The main issue arise from the nonlinear behavior of the partial pressure variable, which is explicable by the high vapor pressure of the Zinc (In the Fig. 2.3-b can be seen the abrupt change of the partial pressure of the chamber).

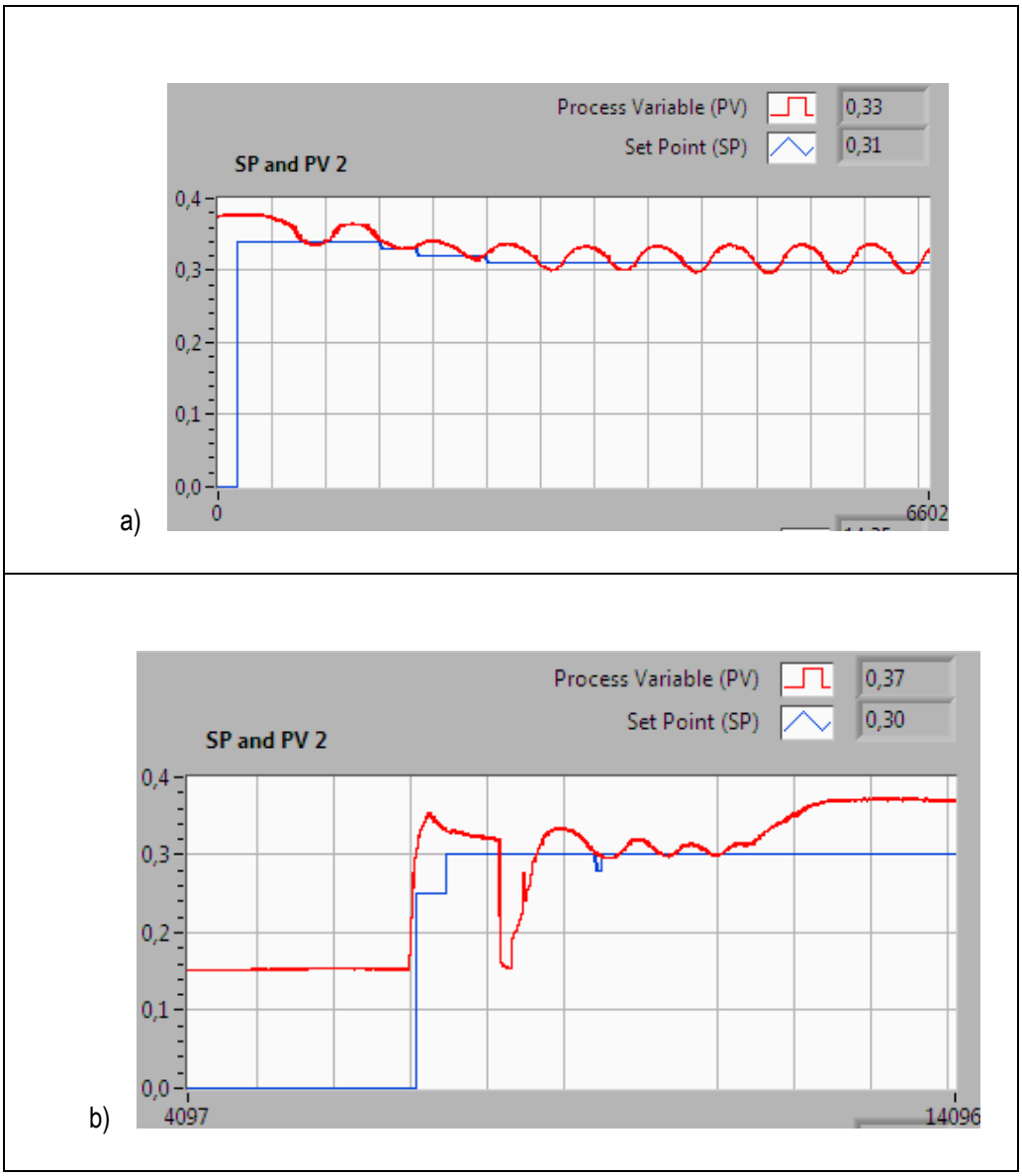

Figure 2.3 Close loop response of partial pressure of chamber in plasma assisted reactive evaporation process.

Taking into account the difficulties describe above it is necessary developed a dynamic model that allows a dynamic optimization of the process and a nonlinear control to perform in an efficient way the partial pressure of chamber, which is the main variable that influences the reaction behavior and thus the final thin films properties.

Chapter 3

Modeling and simulation of Plasma Assisted Reactive Evaporation process

The advantages that the PARE process present with respect to the most common deposition techniques, motivate its investigation in this work, and more specifically its modeling, simulation and experimentation. The objective is to optimize the conditions of synthesis of ZnO films in order to improve both its opto-electric properties and its reproducibility.

The optimal design and operation of PARE processes that achieve the desired performance specifications require the development of an accurate mathematical model. The key issue in the modeling process is the understanding and characterization of the physico-chemical phenomena involved in such processes, including glow discharge chemistry, electron density and energy distribution, ion transport, diffusive and convective mass transfer, bulk and deposition reaction kinetics. Since no model of reactive evaporation process is reported at least in the open literature, the develop of a model to compute the process behavior is very important, however could not be too complex to be used in the optimization and control tasks. It is however noteworthy that some dynamic models for plasma enhanced chemical vapor deposition, Knudsen effusion method and radial flow plasma reactor are developed [58-63], and will be used as references for this work.

This chapters is focused in the development of the dynamic model for Plasma Assisted Reactive Evaporation process used for synthesis and deposition of ZnO thin films. The initial elements necessary for the model building are described below.

3.1 Process description and modeling

Figure 3.1 shows a representation of the setup of the PARE process. It includes parallel electrodes to generate the plasma and Knudsen effusion cell type Zn evaporation source. The objective of the process is to deposit 800 nm thickness of ZnO thin films on an 5x5 cm soda-lime glass substrate, which is placed above the top electrode.

The reactor is simultaneously feed with Zn vapor from the Knudsen cell and oxygen whose flowrate is measured by means of an electronic flow mass controller. The flow rate and composition of the influents gas stream will be assumed uniform. A DC power supply with current regulation is used to generate the plasma (i.e. chemically reactive mixture of ions, electrons and radicals) produced by the mixture of O_2 and Zn. The resulting ZnO molecules and Zn are then transported by convection and diffusion to the surface of the substrate where condensates form a thin film. Plasma species that do not deposit and unreacted are pumped outwards. In the next sections, a first principle model for the PARE reactor represented in Figure 3.1 is developed.

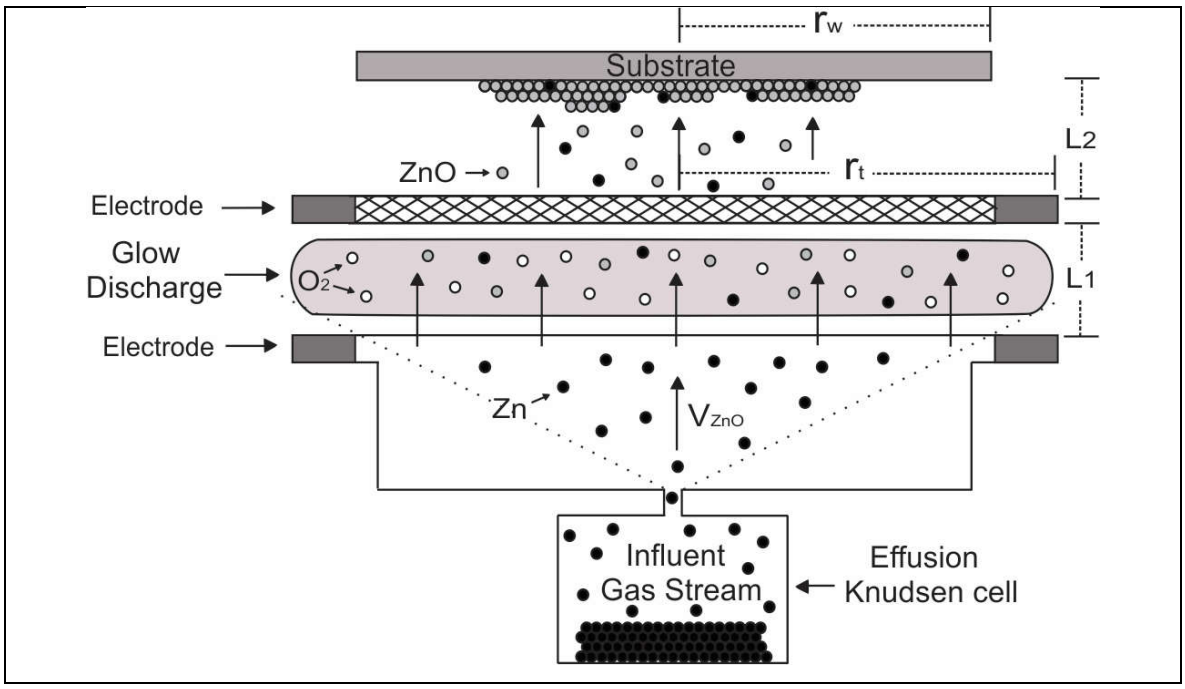

Figure 3.1 Modeling scheme of plasma assisted reactive evaporation process.

3.1.1 Flow Field

The gas flow inside the PARE reactor resembles a three-dimensional axisymmetric stagnant flow. Under the following standard assumptions: (i) plasma is considered as a continuum medium, (ii) constant physical properties of the gas, (iii) negligible volume change of the reacting gases, and (iv) azimuthal reactor symmetry; the velocity vector field inside the PARE reactor can be computed from the following steady-state Navier-Stokes and continuity equations [62]:

$$\frac{\partial v_r}{\partial t} + v_r \frac{\partial v_r}{\partial r} + v_z \frac{\partial v_r}{\partial z} = -\frac{1}{\rho}\frac{\partial P}{\partial r} + \nu\left(\frac{\partial^2 v_r}{\partial r^2} + \frac{1}{r}\frac{\partial v_r}{\partial_r} - \frac{v_r}{r^2} + \frac{\partial^2 v_r}{\partial z^2}\right) \quad (3.1a)$$

$$\frac{\partial v_r}{\partial t} + v_r \frac{\partial v_r}{\partial r} + v_z \frac{\partial v_r}{\partial z} = -\frac{1}{\rho}\frac{\partial P}{\partial z} + \nu\left(\frac{\partial^2 v_z}{\partial r^2} + \frac{1}{r}\frac{\partial v_z}{\partial_r} + \frac{\partial^2 v_z}{\partial z^2}\right) \quad (3.1b)$$

$$\frac{\partial v_r}{\partial r} + \frac{v_r}{r} + \frac{\partial v_z}{\partial z} = 0 \quad (3.1c)$$

The associated boundary conditions for Zn vapor flow are:

$$v_r(r,0) = 0, \quad v_z(r,0) = v_{w,ZnO_2},\ v_r(r,L) = 0,\ v_z(r,L) = 0 \quad (3.1d)$$

where v_r is the velocity in the r-direction, v_z is the velocity in the z-direction, $r \in [0, r_t]$ is the radial coordinate, r_t is the radius of the reactor, $z \in [0, L]$ is the axial coordinate, L is the distance between the lower electrode and the substrate, L_1 is the distance between the two electrodes, ρ is the density of the plasma (constant), P is the pressure, ν is the kinematic viscosity defined as $\nu = \mu/\rho$, μ is the viscosity of the plasma, v_w is the velocity of the oxygen that feeds the reactor.

The expressions of v_{r,ZnO_2} and v_{z,ZnO_2} obtained from the analytical solution of the Navier-Stokes and continuity equations (Eqs. (3.1)) are given as [62]:

$$v_{r,i}(z,r) = \frac{V_{w,ZnO_2}}{L} r\left[-\frac{3}{4}\psi^2 + \frac{3}{4} + Re_{w,ZnO_2}\left(-\frac{1}{160}\psi^6 + \frac{3}{32}\psi^4 + \frac{1}{4}\psi^3 - \frac{117}{1120}\psi^2 - \frac{1}{4}\psi\frac{19}{1120}\right)\right] \quad (3.2a)$$

$$v_{z,i}(z) = V_{w,ZnO_2}\left[-\frac{1}{4}\psi^3 + \frac{3}{4}\psi + \frac{1}{2} + Re_{w,ZnO_2}\left(-\frac{1}{1120}\psi^7 + \frac{3}{160}\psi^5 + \frac{1}{16}\psi^4 - \frac{39}{1120}\psi^3 - \frac{1}{8}\psi^2 + \frac{19}{1120}\psi + \frac{1}{16}\right)\right] \quad (3.2b)$$

Where i $\psi = 2z/L - 1$ and Re_{w,ZnO_2} the wall Reynolds number defined as $Re_{w,ZnO_2} = V_{w,ZnO_2}L/4\nu$. Using the values presented in Table 3.1 and assuming that v_z is only a function of *z*, the value of Re_w calculated for the reactor shown in Fig. 3.1 is found to be equal to 0.45.

Table 3.1 PARE reactor parameters.

$Q(T,P)$	20 cm^3/min
N_h	1010
l_h	0.2 cm
P	1,3-3,1x10^{-2} mbar
L_1	2 cm
L_2	7.3 cm
L	9.3 cm
r_t	3.75 cm
r_w	2.6 cm
n_{eo}	5x10^{-9} cm^{-3} [67]
$\boldsymbol{\mu}$	3.2659x10^{-6} kg s^{-2} cm^{-1}
ρ	2.233x10^{-1} kg cm^{-3}

The velocity at the top electrode of the supplied O_2 gas is assumed to be uniform and can be calculated as : $\boldsymbol{V_{w,O_2} = Q(T,P)/N_h \pi r_h^2}$, where $\boldsymbol{Q(T,P)}$ is the volumetric flow rate of the O_2 precursor gas at the operating conditions of the reactor, $\boldsymbol{N_h}$ is the number of holes on the top electrode, $\boldsymbol{r_h}$ is the radius of each hole.

Taking into account the fact that Zn comes from an isothermal Knudsen effusion evaporation source with a very small exit orifice (0.5 - 2.0 mm), the velocity of Zn arriving at the bottom electrode ($\boldsymbol{V_{w,Zn}}$) is assumed to be uniform [64]. In this work we assume that $\boldsymbol{V_{w,Zn}}$ is proportional to the deposition rate of Zn ($\boldsymbol{V_{w,Zn} \sim d(\Delta l)/dt}$), experimentally measured by means of a quartz crystal microbalance (QCM), which is an extremely sensitive mass sensor able to detect mass changes in the nanogram (10^{-9} g) scale.

The experimental setup used to determine the velocity of Zn arriving at the bottom electrode by measuring the Zn deposition rate is shown in Fig. 3.2. The corresponding values of the deposition rate at different evaporation temperature are presented in Table 3.2.

Table 3.2 Values of deposition rate of Zn as a function of the Knudsen cell temperature.

T ($°C$)	Zn deposition rate (Å/s)
390	0
400	0.4
410	0.9
420	1.4
430	1.6
440	1.8
450	1.9
460	2.0
480	2.2

As expected, the deposition rate increases with the Knudsen cell temperature.

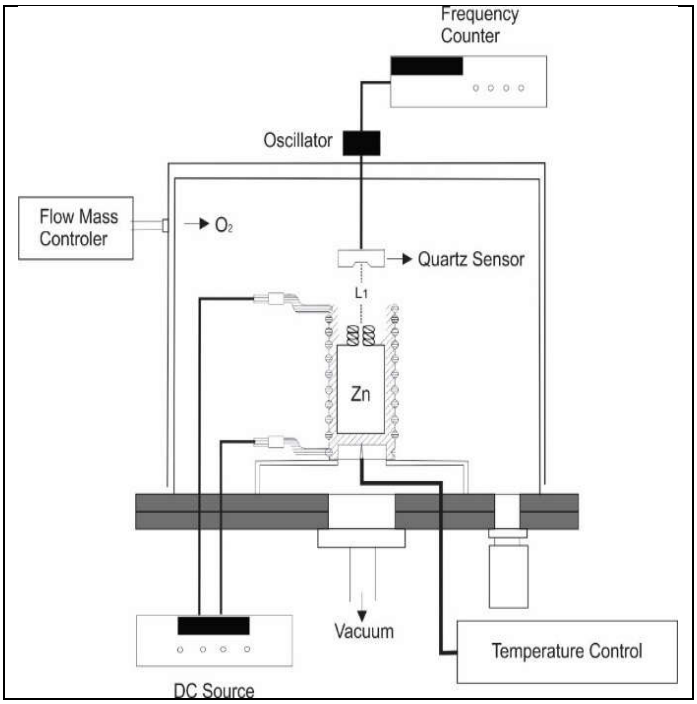

Figure 3.2 Diagram of the experimental setup used for the measurement of the deposition rate of Zn.

3.1.2 Reactions, mass transport and thin film deposition

Since under the operating conditions of 10^{-3} mbar and 600V DC bias voltage, the secondary electron emission can be assumed as negligible and the glow discharge is mainly sustained by bulk ionization, the steady-state electron density $\boldsymbol{n_e}(\mathbf{r}, \mathbf{z})$ is therefore assumed to be uniform throughout the discharge zone and is given by the following relation:

$$\boldsymbol{n_e}(\mathbf{r}, \mathbf{z}) = \boldsymbol{n_{eo}} \tag{3.3}$$

where $\boldsymbol{n_{eo}}$ is the maximum electron density in the reactor which depends on the power dissipated in the plasma, the plasma volume and the effective electric field. The value of $\boldsymbol{n_{eo}}$ is estimated on the basis of information reported in [65,66] using experimental data obtained with a Langmuir probe.

3.1.3 Reactions, mass transport and thin film deposition

Regarding the reactions that take place in the bulk of the plasma, it is assumed that the difference of potential applied between the electrodes to generate the glow discharge induces the following processes:

(i) Dissociation of O_2 followed by supply of sufficient energy to ionize the atoms of oxygen present. Initially, the following species are generated:

$$\boldsymbol{O_{2(g)} + e^- \rightarrow O_{(g)}^{\cdot} + O_{(g)}^{\cdot} + e^-} \quad (3.4)$$

$$\boldsymbol{O_{(g)}^{\cdot} + e^- \rightarrow O_{(g)}^-} \quad (3.5)$$

$$\boldsymbol{O_{2(g)} + e^- \rightarrow O_{(g)}^{\cdot} + O_{(g)}^-} \quad (3.6)$$

$$\boldsymbol{O_{2(g)} + e^- \rightarrow O_{(g)}^+ + O_{(g)}^- + e^-} \quad (3.7)$$

(ii) When Zn vapor enters the region of glow discharge, the following reaction takes place:

$$\boldsymbol{Zn_{(g)} + e^- \rightarrow Zn_{(g)}^+ + 2e^-} \quad (3.8)$$

(iii) Once the precursor species (i.e. O and Zn) are ionized, they can be neutralized by binary collisions through the process of recombination and removal of ions:

$$\boldsymbol{Zn_{(g)}^+ + O_{(g)}^- \rightarrow ZnO_{(g)}} \quad (3.9)$$

$$\boldsymbol{Zn_{(g)} + O_{2(g)} \rightarrow ZnO_{(g)} + O_{(g)}^{\cdot}} \quad (3.10)$$

(iv) Finally, the ZnO(g) generated in the plasma diffuses toward the substrate to form a thin film. e^- is the electron, $\boldsymbol{O_{2(g)}}$ the gaseous oxygen, $\boldsymbol{O_{(g)}^{\cdot}}$ the oxygen radical, $\boldsymbol{O_{(g)}^-}$ the ionized oxygen, $\boldsymbol{Zn_{(g)}}$ is the zinc atom, $\boldsymbol{Zn_{(g)}^+}$ the ionized zinc and $\boldsymbol{ZnO_{(g)}}$ is the gaseous zinc oxide.

Assuming that the effective reaction rates can be expressed as a product of the dissociation constants, electron density and reactant species concentrations, the following expressions can be written for the rate of change of the concentration $\boldsymbol{r_{x,i}}$ of the species involved in the reactions (3.4-3.10):

$$\boldsymbol{r_{x,1} = -k_1 n_e C_1 - k_3 n_e C_1 - k_4 n_e C_1 - k_7 C_4 C_1} \quad (3.11)$$

$$\boldsymbol{r_{x,2} = 2k_1 n_e C_1 - k_2 n_e C_2 + k_3 n_e C_1 + k_7 C_1 C_4} \quad (3.12)$$

$$r_{x,3} = k_2 n_e C_2 + k_3 n_e C_1 + k_4 n_e C_1 - k_6 C_3 C_5 \quad (3.13)$$

$$r_{x,4} = -k_5 n_e C_4 - k_7 C_4 C_1 \quad (3.14)$$

$$r_{x,5} = k_5 n_e C_4 - k_6 C_5 C_3 \quad (3.15)$$

$$r_{x,6} = k_6 C_5 C_3 + k_7 C_1 C_4 \quad (3.16)$$

$$r_{x,7} = k_4 n_e C_1 \quad (3.17)$$

where the subscripts $i = 1, 2, 3, 4, 5, 6 \; and \; 7$ correspond to $O_{2(g)}$, $O_{(g)}$, $O^-_{(g)}$, $Zn_{(g)}$, $Zn^+_{(g)}$, $ZnO_{(g)}$and $O^+_{(g)}$ respectively; C_i is the concentration of each species and k_j is the rate constant of the reaction *j* (*j*=1,2,…,7) (3.4-3.10).

Applying dynamic material balances to the process and accounting for diffusive and convective mass transfer, and bulk and surface reactions, a mathematical model that describes the spatio-temporal evolution of the concentration of the species throughout the reactor is developed. This model consists of six nonlinear parabolic partial differential equations and can be written in the following compact form:

$$\frac{\partial c_i}{\partial t} = D_i \left(\frac{\partial^2 c_i}{\partial r^2} + \frac{1}{r} \frac{\partial c_i}{\partial_r} + \frac{\partial^2 c_i}{\partial z^2} \right) - \left(v_{r,O_2} + v_{r,Zn} \right) \frac{\partial c_i}{\partial r} - \left(v_{z,O_2} + v_{z,Zn} \right) \frac{\partial c_i}{\partial z} +$$
$$r_{x,i}(n_e, C_1, C_2, C_3, C_4, C_5, C_6), \; i = 1, \ldots, 6 \quad (3.18)$$

where D_i is the diffusion coefficient of the *i*th species and v_{z,O_2} and $v_{z,Zn}$ are the analytic solutions of the Navier-Stokes and continuity equations.

The associated boundary conditions are given as:

$$\frac{\partial c_i}{\partial r}(t, 0, z) = 0; \quad i = 1, \ldots, 6 \quad (3.19)$$

$$\frac{\partial c_i}{\partial r}(t, r_t, z) = 0; \; i = 1, 2, 3 \; and \; 5 \quad (3.20)$$

$$c_i(t, r_t, z) = 0; \; i = 4 \; and \; 6 \quad (3.21)$$

$$c_i(t, r, O) = c_{w,i}(t, r); \quad i = 1, \ldots, 6 \quad (3.22)$$

$$\frac{\partial c_i}{\partial z}(t, r, L_1) = 0; \quad i = 2, 3 \; and \; 5 \quad (3.23)$$

$$c_i(t, r, L) = 0; \; i = 4 \; and \; 6 \quad (3.24)$$

$$\frac{\partial c_1}{\partial z}(t, r, L) = 0 \quad (3.25)$$

and the initial conditions are:

$$\boldsymbol{c(0,r,z) = c_i^0(r,z)\ i = 1,\dots,6} \tag{3.26}$$

where $\boldsymbol{r}$ is the radius of the wafer, $\boldsymbol{c_{w,i}(t)}$ is the concentration of the specific species in the feed, and $\boldsymbol{c_i^0(r,z)}$ is the concentration of the species initially in the chamber. The boundary conditions (3.24) express the instantaneous consumption of Zn and ZnO on the substrate surface and the reactor walls, and the boundary condition (3.22) accounts for no mass flux of $\boldsymbol{O_{(g)}^{\cdot}}$, $\boldsymbol{O_{(g)}^{-}}$ and $\boldsymbol{Zn_{(g)}^{+}}$ outside the glow discharge zone. The boundary conditions (3.20) accounts for the non-reaction of the species $\boldsymbol{O_{2(g)}}$, $\boldsymbol{O_{(g)}^{\cdot}}$, $\boldsymbol{O_{(g)}^{-}}$ and $\boldsymbol{Zn_{(g)}^{+}}$ with the substrate and the reactor walls. The deposition rate of ZnO on the substrate is calculated by means of the following equation:

$$\boldsymbol{R_{dep}(t,r) = \frac{1}{\rho_{ZnO}}\left[\sum_{i=1}^{7} s_i D_i \frac{\partial c_i}{\partial r}(t,r,L)\right]} \tag{3.27}$$

where ρ_{ZnO} is the density of ZnO and s_i represents the percentage of the flux of the *i*th species towards the surface leading to deposition of zinc oxide (sticking probability).

3.2 Simulation of a Plasma Assisted Reactive Evaporation process

The PARE model equations (3.1-3.3 and 3.18-3.27) were solved using numerical techniques. More specifically, the finite difference method was initially used to discretize the spatial derivatives of Eqs. (3.18-3.27) in *r* and *z* directions using 75x75 discretization points. It was verified that further increase in the number of discretization points in both *r* and *z* directions results in insignificant improvements in the accuracy of the computed solution. Then, the time integration of the resulting (75x75) large set of ordinary differential equations was performed using the alternate direction implicit (ADI) method. In all the simulation runs, the reactor was initially assumed to be filled with pure oxygen. The computation algorithm was implemented within Matlab® and the simulations results were compared to those obtained using COMSOL Multiphysics software. Very similar results were achieved by the two methods. However, we will keep using the finite difference method under Matlab® because it offers more flexibility in the perspective of dynamic optimization and control of PARE process.

3.2.1 The Finite Difference Method (FDM)

The finite difference approximations for derivatives are one of the simplest and of the oldest methods to solve differential equations. It was already known by L. Euler 1768, in one dimension of space and was probably extended to dimension two by C. Runge 1908. The advent of finite difference techniques in numerical applications began in the early 1950s and their development was stimulated by the emergence of computers that offered a convenient framework for dealing with complex problems of science and technology. Theoretical results have been obtained during the last five decades regarding the accuracy, stability and convergence of the finite difference method for partial differential equations [70].

General principle

The principle of finite difference methods (FDM) consist in convert a linear (non-linear) ODE (Ordinary Differential Equations) /PDE (Partial differential equations) into a system of linear (non-linear) equations, which can then be solved by matrix algebra techniques. This is made approximating the differential operator by replacing the derivatives in the equation using differential quotients. The domain is partitioned in space and in time and approximations of the solution are computed at the space or time points. The error between the numerical solution and the exact solution is determined by the error that is commited by going from a differential operator to a difference operator. This error is called the discretization error or truncation error. The term truncation error reflects the fact that a finite part of a Taylor series is used in the approximation.

Derivation from Taylor's polynomial

First, assuming the function whose derivatives are to be approximated is properly-behaved, by Taylor's theorem, we can create a Taylor series expansion

$$f(x_0 + h) = f(x_0) + \frac{f\prime(x_0)}{1!}h + \frac{f^{(2)}(x_0)}{2!}h^2 + \cdots + \frac{f^n(x_0)}{n!}h^n + R_n(x) \quad (3.28)$$

where $n!$ denotes the factorial of n, and $R_n(x)$ is a discretization error, denoting the difference between the Taylor polynomial of degree *n* and the original function.

In FDM to approximate the ODE/PDE equations, three forms are commonly considered: forward, backward, and central differences. Assuming that $R_1(x)$ is sufficiently small, the approximation of the first derivative of "f" is presented below; first truncating the Taylor polynomial:

$$f(x_0 + h) = f(x_0) + f'(x_0)h + R_1(x) \quad (3.29)$$

Dividing across by h gives:

$$\frac{f(x_0+h)}{h} = \frac{f(x_0)}{h} + f'(x_0) + \frac{R_1(x)}{h} \quad (3.30)$$

Solving for $f'(x_0)$

$$f'(x_0) = \frac{f(x+h)-f(x)}{h} - \frac{R_1(x)}{h} \quad (3.31)$$

The First forward difference, First backward difference, First centered difference, Second forward difference, second backward difference, second centered difference, are presented in equations 3.32 to 3.37 respectivedly.

$$f'(x_i) = \frac{f(x_{i+1})-f(x_i)}{x_{i+1}-x_i} \quad (3.32)$$

$$f'(x_i) = \frac{f(x_i)-f(x_{i-1})}{x_i-x_{i-1}} \quad (3.33)$$

$$f'(x_i) = \frac{f(x_{i+1})-f(x_{i-1})}{2h} \quad (3.34)$$

$$f''(x_i) = \frac{f(x_i)-2f(x_{i-1})+f(x_{i-2})}{h^2} \quad (3.35)$$

$$f''(x_i) = \frac{f(x_{i+2})-2f(x_{i+1})+f(x_i)}{h^2} \quad (3.36)$$

$$f''(x_i) = \frac{f(x_{i+1})-2f(x_i)+f(x_{i-1})}{h^2} \quad (3.37)$$

Using this approximation it is possible to construct different discretization schemes for ODE/PDE in first or second order, the most commonly used are, implicit, explicit, krack Nicholson and Alternative Direction Implicit (ADI) methods . Taking into account the characteristic of the model was develop which is two dimensional partial differential equations use the ADI method is a good alternative to construct the discretization scheme.

3.2.2 Construction of a discretization scheme using ADI method

The construction of the ADI scheme is developed in two steps. In the first step is constructed an implicit scheme with $z\ (j)$ fixed by applying First backward difference in time $t_{n+\frac{1}{2}}$ for $\frac{\partial u}{\partial t}$ and Second centered difference is space for $\frac{\partial^2 u}{\partial r^2}$, such as is show below.

$$\frac{u_{i,j}^{n+\frac{1}{2}}-u_{i,j}^{n}}{\frac{\Delta t}{2}} = D_1\left(\frac{u_{i+1,j}^{n+\frac{1}{2}}-2u_{i,j}^{n+\frac{1}{2}}+u_{i-1,j}^{n+\frac{1}{2}}}{(\Delta r)^2}+\frac{u_{i,j+1}^{n}-2u_{i,j}^{n}+u_{i,j-1}^{n}}{(\Delta z)^2}\right)+\left(\frac{D_1}{r}-v_{r,ZnO_2}\right)\left(\frac{u_{i+1,j}^{n+\frac{1}{2}}-u_{i-1,j}^{n+1/2}}{2\Delta r}\right)-$$
$$v_{z,ZnO_2}\left(\frac{u_{i,j+1}^{n}-u_{i,j-1}^{n}}{2\Delta z}\right)-(k_1n_e+k_3n_e+k_4n_e+k_1u_{4,i,j}^{n})u_{i,j}^{n} \quad (3.38)$$

In the second step is constructed an implicit scheme with $r\ (i)$ fixed by applying First backward difference in time t_{n+1} for $\frac{\partial u}{\partial t}$ and Second centered difference is space for $\frac{\partial^2 u}{\partial z^2}$, such as is show below.

$$\frac{u_{i,j}^{n+1}-u_{i,j}^{n+\frac{1}{2}}}{\frac{\Delta t}{2}} = D_1\left(\frac{u_{i+1,j}^{n+\frac{1}{2}}-2u_{i,j}^{n+\frac{1}{2}}+u_{i-1,j}^{n+\frac{1}{2}}}{(\Delta r)^2}+\frac{u_{i,j+1}^{n+1}-2u_{i,j}^{n+1}+u_{i,j-1}^{n+1}}{(\Delta z)^2}\right)+\left(\frac{D_1}{r}-v_{r,ZnO_2}\right)\left(\frac{u_{i+1,j}^{n+\frac{1}{2}}-u_{i-1,j}^{n+1/2}}{2\Delta r}\right)-$$
$$v_{z,ZnO_2}\left(\frac{u_{i,j+1}^{n+1}-u_{i,j-1}^{n+1}}{2\Delta z}\right)-(k_1n_e+k_3n_e+k_4n_e+k_1u_{4,i,j}^{n})u_{i,j}^{n+\frac{1}{2}} \quad (3.39)$$

Both equations can be written in a tridiagonal form. Define:

$$\Delta r = \Delta z = h \quad (3.40)$$
$$\alpha = \frac{D_1\Delta t}{2(\Delta r)^2} \quad (3.41)$$
$$\beta = \frac{D_1\Delta t}{2(\Delta z)^2} \quad (3.42)$$
$$\Phi = \frac{\Delta t}{4\Delta r}\left(\frac{D_1}{r}-v_{r,ZnO_2}\right) \quad (3.43)$$
$$\gamma = \frac{\Delta t v_{z,ZnO_2}}{4\Delta z} \quad (3.44)$$

Then is obtained:

$$-1(\alpha+\Phi)u_{i+1,j}^{n+\frac{1}{2}}+(1+2\alpha)u_{i,j}^{n+\frac{1}{2}}+(\Phi-\alpha)u_{i-1,j}^{n+\frac{1}{2}} = (\beta-\gamma)u_{i,j+1}^{n}+(1-2\beta-k_1n_e-k_3n_e-$$
$$k_4n_e-k_1u_{4,i,j}^{n})u_{i,j}^{n}+(\beta+\gamma)u_{i,j-1}^{n} \quad (3.45)$$

$$(\gamma-\beta)u_{i,j+1}^{n+1}+(1+2\beta)u_{i,j}^{n+1}-(\gamma+\beta)u_{i,j-1}^{n+1} = (\alpha+\Phi)u_{i+1,j}^{n+\frac{1}{2}}+(1-2\alpha-k_1n_e-k_3n_e-$$
$$k_4n_e-k_1u_{4,i,j}^{n})u_{i,j}^{n+\frac{1}{2}}+(\alpha-\Phi)u_{i-1,j}^{n+\frac{1}{2}} \quad (3.46)$$

The solution is computed by solving the two following tridiagonal matrix system:

$$\boldsymbol{A u_{i,j}^{n+1/2} = B u_{i,j}^{n} + b} \quad (3.46)$$

$$\boldsymbol{C u_{i,j}^{n+1} = D u_{i,j}^{n+1/2} + b} \quad (3.47)$$

Where $\boldsymbol{b}$ are the boundary conditions.

3.2.3 Simulation results

The operating conditions and the reactor parameters are given in Table 3.1, the reaction rate constants are presented in Table 3.3; and finally the physico-chemical properties of the species are listed in Table 3.4. It is worth mentioning that: (i) the physical properties of the plasma (e.g. viscosity) were computed by assuming that the plasma consists of pure oxygen, (ii) the density of the mixture was calculated from the ideal gas law, and (iii) the diffusion coefficients of radicals and ZnO were calculated from equations based on Lennard-Jones potential under the assumption that all the species diffuse through pure oxygen.

Table 3.3 Reaction rate constants for the equations 3.11 to 3.16.

Reaction	Rate constant	Units	Reference
$\boldsymbol{O_{2(g)} + e^- \rightarrow O_{(g)}^{\cdot} + O_{(g)}^{\cdot} + e^-}$	$\boldsymbol{k_1 = 5.761 \text{ x } 10^{-18}}$	s^{-1} cm^3	[69]
$\boldsymbol{O_{(g)}^{\cdot} + e^- \rightarrow O_{(g)}^-}$	$\boldsymbol{k_2 = 1.00 \text{ x } 10^{-31}}$	s^{-1} cm^3	[68]
$\boldsymbol{O_{2(g)} + e^- \rightarrow O_{(g)}^{\cdot} + O_{(g)}^-}$	$\boldsymbol{k_3 = 1.479 \text{ x } 10^{-11}}$	s^{-1} cm^3	[68]
$\boldsymbol{Zn_{(g)} + e^- \rightarrow Zn_{(g)}^+ + 2e^-}$	$\boldsymbol{k_5 = 1.300 \text{ x } 10^{-11}}$	s^{-1} cm^3	[67]
$\boldsymbol{Zn_{(g)}^+ + O_{(g)}^- \rightarrow ZnO_{(g)}}$	$\boldsymbol{k_6 = 1.000 \text{ x } 10^{-13}}$	s^{-1} mol^{-1} cm^3	[67]
$\boldsymbol{Zn_{(g)} + O_{2(g)} \rightarrow ZnO_{(g)} + O_{(g)}^{\cdot}}$	$\boldsymbol{k_7 = 3.735 \text{ x } 10^{-18}}$	s^{-1} mol^{-1} cm^3	[67]

Table 3. 4 Diffusion coefficients and initial concentration for each species.

Properties	$\boldsymbol{O_{2(g)}}$	$\boldsymbol{O_{(g)}^{\cdot}}$	$\boldsymbol{O_{(g)}^-}$	$\boldsymbol{Zn_{(g)}}$	$\boldsymbol{Zn_{(g)}^+}$	$\boldsymbol{ZnO_{(g)}}$
D_i (cm^2 s^{-1})	14.37	17.60	17.60	16.65	16.65	23.45
$c_{w,i}/c_i$	0.5	0	0	0.5	0	0

Figure 3.3 shows the profile of the steady-state oxygen concentration $O_{2(g)}$ inside the reactor. It can be seen that the concentration of O_2 is radially uniform, but varies in the axial direction. More specifically, it is higher at the lower edge of the reactor, and decreases with the axial position towards the top edge.

In Figure 3.4 it is observed that the Zn concentration is not uniform in both radial and axial directions. At the edge of the substrate, Zn concentration is lower due to the fact that the flow of Zn from the Knudsen cell is greater in the central region than on the edge of the substrate, additionally Zn is deposited in the reactor walls. On the other hand, the concentration of Zn in the lower zone of the reactor is greater than in the upper zone, because part of the Zn is consumed by the dissociation reactions, $Zn^{+}_{(g)} + O^{-}_{(g)} \rightarrow ZnO_{(g)}$ which is immediately deposited on the substrate.

Figure 3.5 shows the profiles of the steady-state concentration of zinc oxide. As expected, the maximum steady-state concentration is located in the lower central region of the reactor. This behavior is due to the fact that, on the one hand the flow of Zn is high in the central region of the reactor and on the other hand the molecules of ZnO formed at the bottom of the reactor diffuse towards the substrate and the chamber walls.

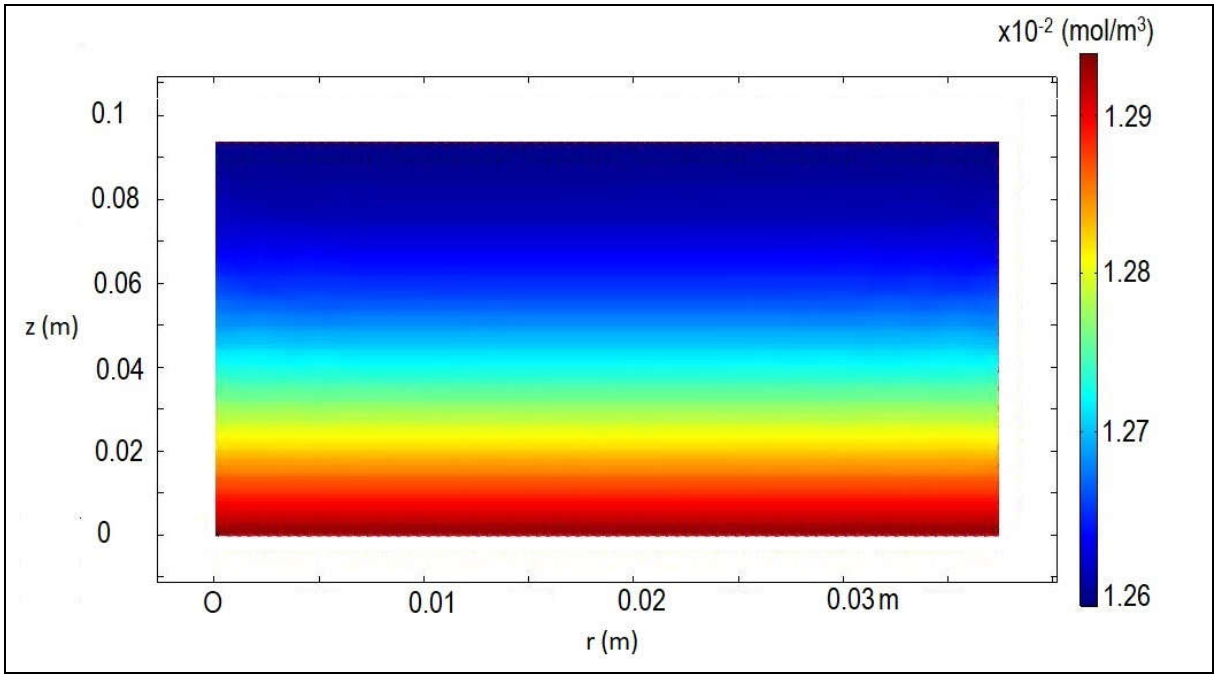

Figure 3.3 Simulation of the distribution profile of the concentration of O2.

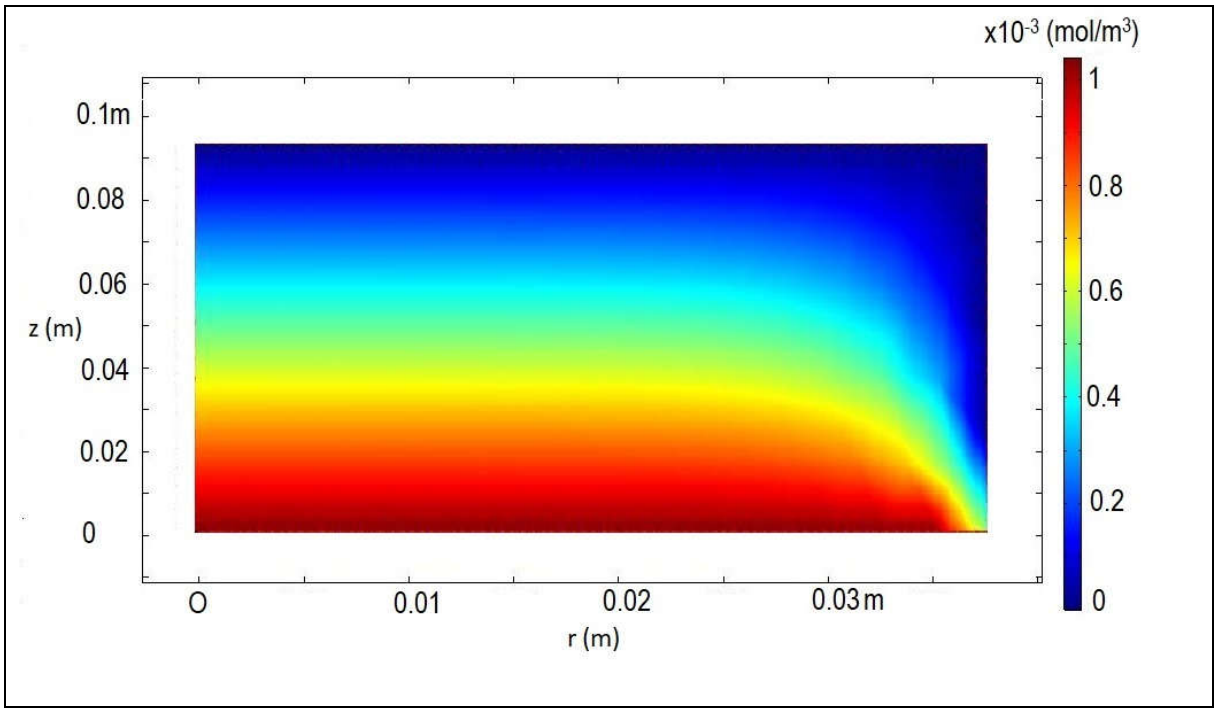

Figure 3.4 Simulation of the distribution profile of the concentration of Zn.

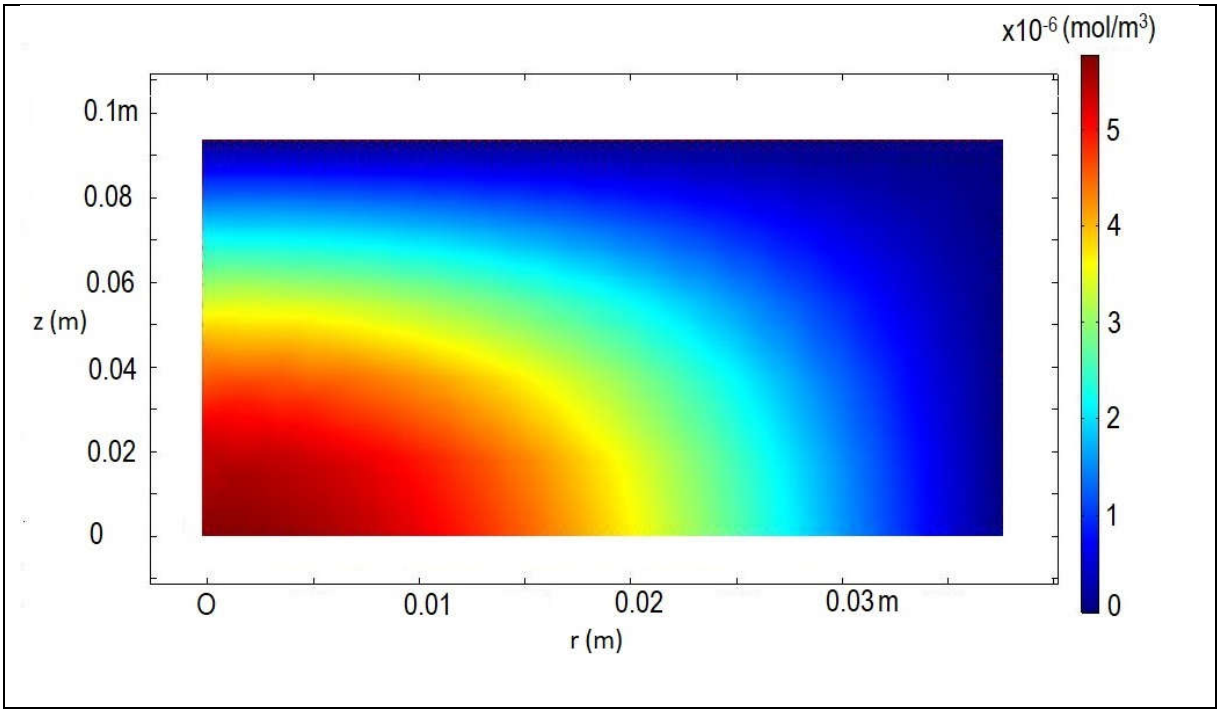

Figure 3.5 Simulation of the distribution profile of the concentration of ZnO.

In the *r*-axis: 0 mm is the center of the substrate, 37.5 mm is the edge of the substrate and 93.0 mm is the edge of the reactor; in the *z*-axis: 0 mm is the Knudsen cell hole and 93.0 mm is the substrate surface, the

non-uniform concentration of ZnO and Zn on the substrate surface leads to a non-uniform profile of deposition rate of zinc oxide thin film along the radius of the substrate. This behavior is coherent with the fact that the ZnO formed in the reactor diffuses simultaneously to the substrate and to the walls of the chamber, leading hence to the growth of thin films of ZnO with a non-uniform final film thickness profile as the ones shown in Fig.3.6. The latter compares the model predictions to the measured values of the ZnO final film thickness versus the radial position in the chamber. The very good agreement observed highlights the high quality of the developed model of PARE with no identification of unknown parameters from experimental measurements.

On the other hand, the high inhomogeneity of the thickness exhibited by the ZnO layers deposited using a Knudsen cell (as shown in Fig. 3.6) to evaporate the Zn can be considerably improved by the use of a Knudsen cell of cross section whose surface is similar to that of the substrate and which comprises several exit holes, as presented in inset of Figure 3.6.

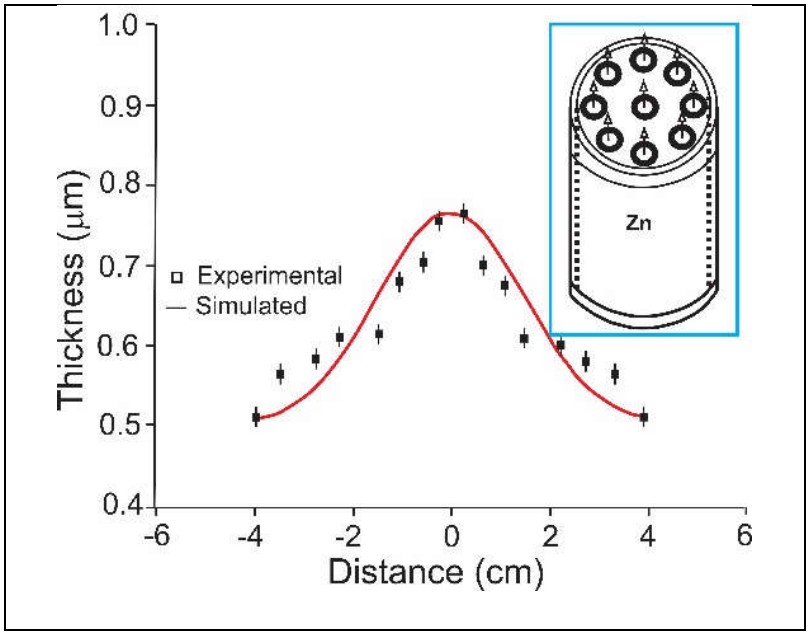

Figure 3.6 Experimental and simulated final film thickness profile of a typical ZnO film. The inset shows a Knudsen cell with a design that allows to improve the homogeneity in the thickness of the ZnO films.

Figure 3.7 presents the variations of the measured values of the ZnO thickness layer (using a thickness monitor) and the model simulation results from Eq. 26. It can be seen that the predictions fit very well the measurements highlighting here again the high accuracy of the model.

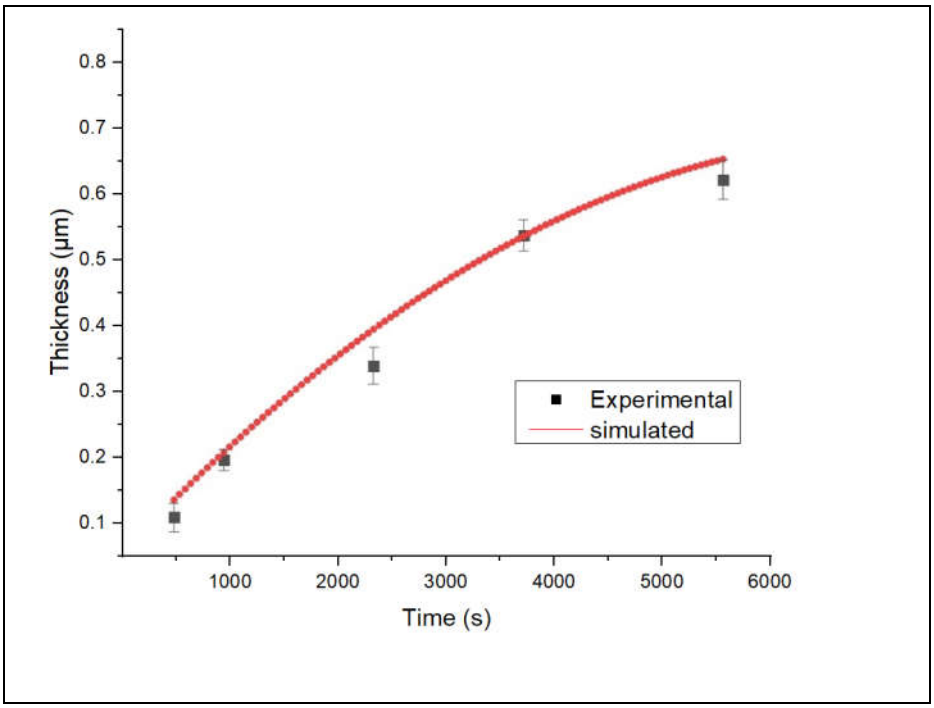

Figure 3.7 Comparison of the experimental measurements of the thickness of ZnO films prepared by reactive evaporation in dependence of the deposition time, with their corresponding simulated values.

The mathematical model predicts that the use of a Zn evaporation source with a design as shown in Fig. 3.6, not only improves the homogeneity of the ZnO layer thickness, but also significantly increases its deposition rate.

Based on the results obtained, it can be concluded that the PARE model developed exhibits very good prediction performances of the main state variables. Furthermore, the model applied here can be used in dynamic optimization of the process, or in studies of process control in order to determine and implement the optimal profiles of main operating variables (i.e. flow rates, temperature and pressure for the PARE process), and then reach the desired end-use properties of the manufactured ZnO films.

It is worth mentioning that the growth process of ZnO films deposited by plasma assisted reactive evaporation method was modeled using a two-dimensional unsteady-state model that takes into account the diffusive and convective mass transfer, bulk and surface reactions, as well as non-uniform fluid flow and plasma electron density profiles. The simulation results show that the ZnO films grow with a non-uniform film thickness profile. They were then implemented within a pilot reactor that is being operated for the growth of ZnO thin films used for the manufacture of different kinds of solar cells.

The experimental measurements of the ZnO film thickness carried out using a thickness monitor, were very well predicted by the PARE model. Furthermore, the simulation tool developed allowed also to compute the

film thickness as a function of the deposition time. The results obtained exhibited a very good agreement with the experimentally measured values.

From this chapter it is possible to summarized that the growth process of ZnO films deposited by plasma assisted reactive evaporation method was modeled using a two-dimensional unsteady-state model that takes into account the diffusive and convective mass transfer, bulk and surface reactions, as well as non-uniform fluid flow and plasma electron density profiles. The simulation results show that the ZnO films grow with a non-uniform film thickness profile. They were then implemented within a pilot reactor that is being operated for the growth of ZnO thin films used for the manufacture of different kinds of solar cells.

The experimental measurements of the ZnO film thickness carried out using a thickness monitor, were very well predicted by the PARE model. Furthermore, the simulation tool developed allowed also to compute the film thickness as a function of the deposition time. The results obtained exhibited a very good agreement with the experimentally measured values.

Finally, he outcomes of this work show that the PARE process model developed is so accurate that it can readily be used to optimize the design and operation of the reactor. More specifically, the objective is to achieve significant improvements in the opto-electrical properties of the ZnO films, as well as of the reproducibility, thickness homogeneity and deposition rate, which would lead to costs reduction mainly in mass production processes.

Chapter 4

Opto-electrical Characterization of ZnO thin films prepared using Plasma Assisted Reactive Evaporation process

4.1 Thin film characterization fundamentals

Thin films can be characterized by many different ways, depending on the desired application; however. in the case of ZnO thin films and its use in photovoltaic applications, the interest is focused in optical and electrical properties as well as in its thickness. In this work we have studied the optical and electrical properties of ZnO through measurements of transmittance (T) and electrical resistivity (ρ).

These measurements were done using a Varian-Cary 5000 spectrophotometer and the 4 point probe method respectively. The film thickess was determined using a Veeco Dektak 150 surface profiler. In Figures 4.1 and 4.2 are shown the setup we used to measure the resistivity and the transmittance of the ZnO films.

The characterization of ZnO thin films have two mains goals, the first one is to determine the influence of the main parameters of the process (Ionization current, Zinc flow and Oxygen flow) on the opto-electrical properties of the ZnO thin films. The second goal is to use this information to construct an empiric model equation to give additional information to that of the process model developed in chapter 3 and to help with the definition of the operating constraints and quality criteria that will be use in the dynamic optimization. The studies were carried out by the preparation of different samples varying the operation conditions with the purpose to find conditions that allow deposit ZnO thin films with resistivity less than 10^{-3} Ωcm and transmittance greater than 85%.

4.1.1 Electric Characterization

The resistivity of the ZnO thin films is the electrical property of interest, its measurement were made using the four probe method, the setup used for this experimental method is shown in fig. 4.1

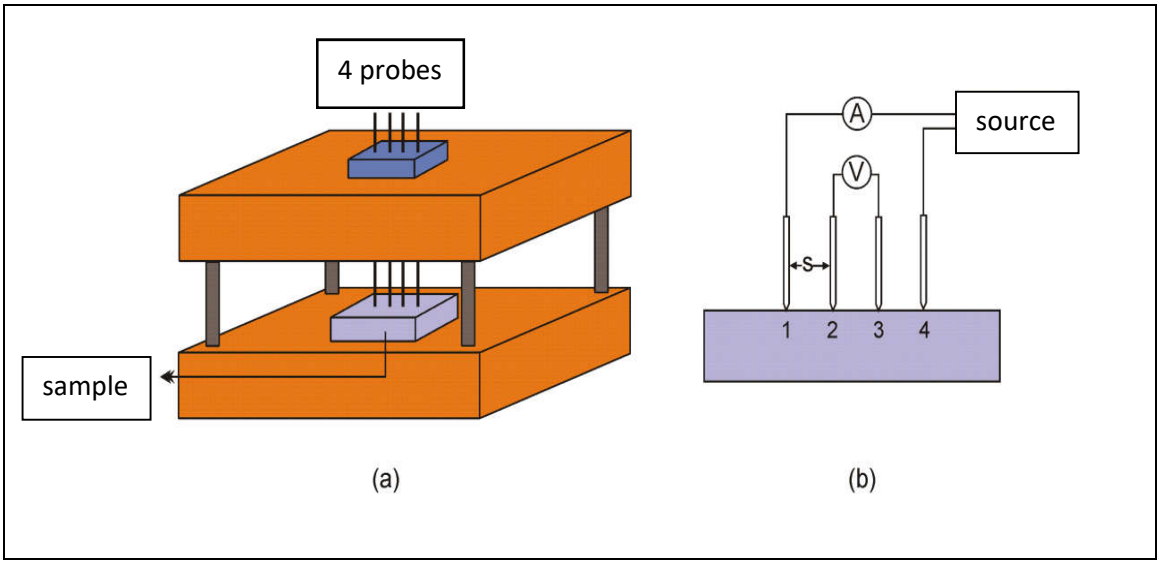

Figure 4.1 a) Scheme of the system used to measure resistivity, b) distribution of the four probes.

To measure the resistivity, four metal probes separated distance S_{23} (a distance of 5 mm was used) are placed on the surface of the thin film. A current (I_{14}) is flowed through probes 1 and 4 and the voltage difference (V_{23}) is measured between probes 2 and 3. The surface resistance is given by the ratio V_{23} / I_{14} and the resistivity of the films is determined by the following equation [71]:

$$\rho = \frac{\pi\omega}{Ln2}\left(\frac{V_{23}}{I_{14}}\right) \tag{4.1}$$

Where ω represents the thickness of the film, V_{23} is the voltage difference measured with a Keithley-189 digital micro-voltmeter and I_{14} is the current measured with a Keithley-185 self-programmable pico-amperimeter.

4.1.2 Optical characterization

The optical properties of thin films are very important for many applications, including interference devices (such as antireflection coatings, laser mirrors, and monochromatic filters), as well as optoelectronics, Integrated optics, solar power engineering, microelectronics, and optical sensor technology. The end application of a film determines the reflectance and transmittance properties required during fabrication. Spectrophotometric methods determine the spectral dependencies of reflectance and transmittance for thin films within the spectral regions of interest [72,73]. Reflectance and transmittance are measured at near-normal incidence and normal incidence, respectively, using various types of spectrophotometers.

Luminous transmittance is a measure of the amount of light that passes through a transparent material. The total light transmittance through a material is equal to the total incident light less the light that is absorbed and light that is scattered. In this work transmittance measurements were made in a range of 300-1200 nm using a Varian-Cary 5000 spectrophotometer.

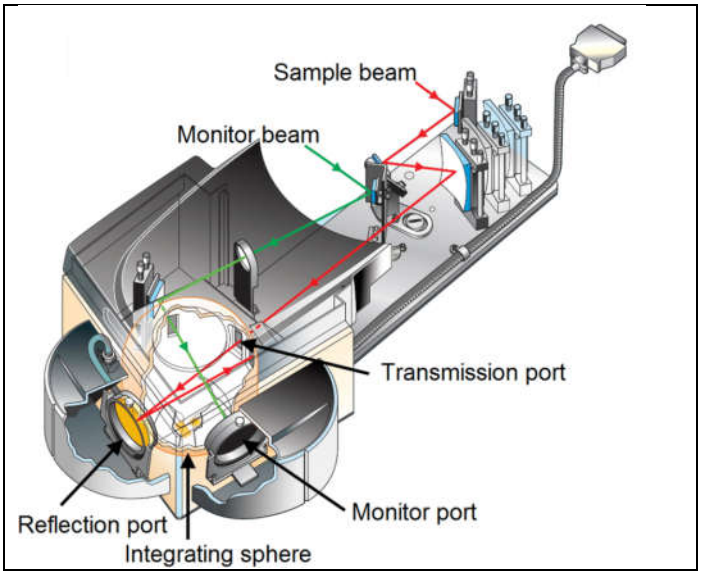

Figure 4.2 Setup of the Varian-Cary 5000 spectrophotometer.[74]

4.2 Influence of deposition conditions on transmittance and resistivity

4.2.1 Influence of the ion current of the glow discharge

To determine the influence of the glow discharge ion current on the transmittance and the resistivity of the thin ZnO films, different samples were deposited in which the oxygen flow and the Zn flow were kept constant and the ion current varied from 2 mA to 20 mA. Additionally, a quality criterion was established through the definition of a merit figure $\Phi_{T\rho} = -1/(\rho * lnT)$ that allow to obtain a good balance between the ρ and T.

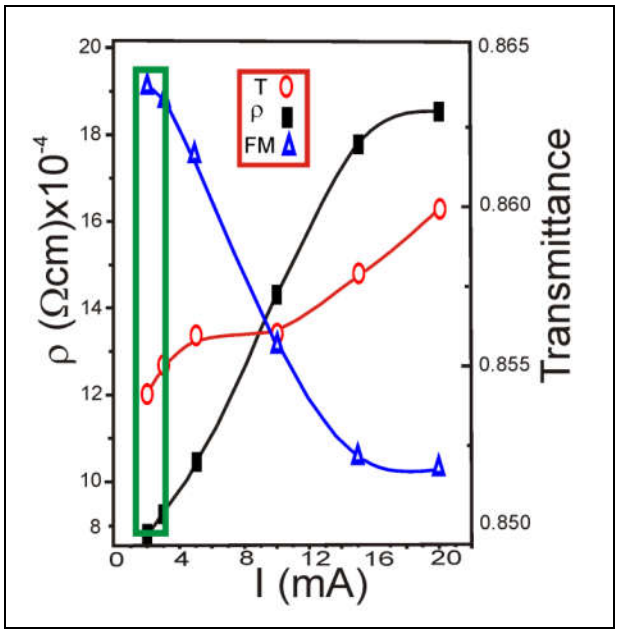

Figure 4.3 Variation of resistivity, transmittance (at 700 nm) and merit figure (quality criteria $\boldsymbol{\Phi_{T\rho}}$) of ZnO thin films as a function of the glow discharge ion current.

Figure 4.3 shows the effect of the glow discharge ion current on the resistivity and on the transmittance of thin films of ZnO. These results show that thin films of ZnO deposited under ion currents of the order of 2 mA present very low values resistivity and transmittance values around of 85%. The increase in the Ion current caused by an increase in the glow discharge voltage leads to an increase in the resistivity of the ZnO films; this behavior is attributed to an increase of the ratio of oxygen ions with respect to the zinc ions and therefore to a reduction of oxygen vacancies. The best figure of merit FM is obtained for ion current values around 2 mA.

From the variation of the FM observed with the variation of the ion current, it can be concluded that the figure of merit of ZnO thin films deposited by reactive evaporation is maximized $\boldsymbol{\Phi_{T\rho}}$ using low values of ion current.

4.2.2 Influence of the oxygen flow

To determine the influence of the oxygen flow on the transmittance and the resistivity of the thin ZnO films, different samples were deposited in which the ion current and the Zn flow were kept constant and f the oxygen flow varied from 10 to 20 ml/min. Additionally a quality criterion or merit figure was established $\boldsymbol{\Phi_{T\rho}} = -\mathbf{1}/(\boldsymbol{\rho} * \boldsymbol{lnT})$ that allow to obtain a good balance between the **ρ** and **T**.

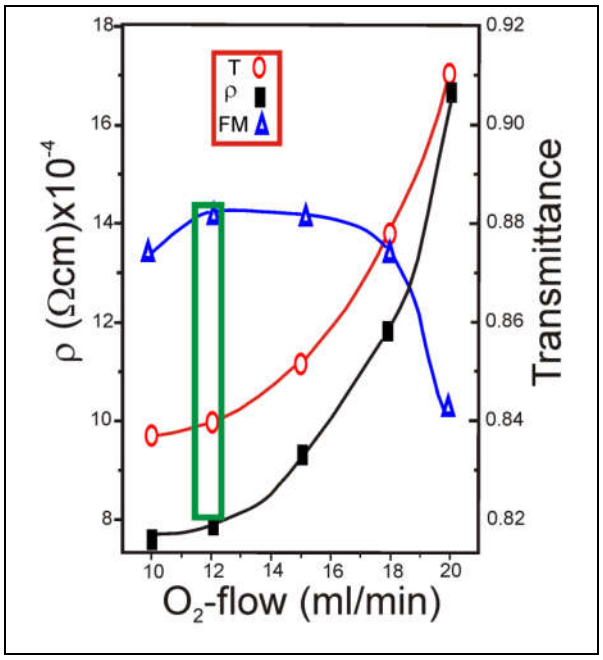

Figure 4.4 Variation of resistivity, transmittance (at 700 nm) and figure of merit (quality criteria $\boldsymbol{\Phi_{T\rho}}$) of ZnO thin films as a function of O2-flow.

Figure 4.4 show the variation of the transmittance and resistivity of the ZnO thin film, in function of the Oxygen flow. These results show that ZnO thin films deposited O_2-flow around of 10 ml/min present very low values of resistivity; this phenomenon is due to the fact that the decrease of O_2-flow has an impact on the increase in the Zn^+/O^- ratio that leads to an increase in the density of oxygen vacancies, which in turn results in an increase in the concentration of free carriers and therefore in the conductivity of the thin ZnO films.

The low transmittances observed for O_2-flow greater than 14 ml/min indicate that in this type of samples the density of donor states associated with oxygen vacancies is sufficiently high to contribute significantly to the absorption of photons with lower energies than the one of the gap; This is due to the fact that when O_2-flow

decrease, a high density of donor defects is produced, which generate absorption centers that give rise to a decrease in transmittance.

From the variation of the $\boldsymbol{\Phi_{T\rho}}$ observed with the variation of oxygen flow it can be concluded that to deposit ZnO thin films which simultaneously exhibit high transmittance and high conductivity, it is necessary to use low oxygen flows due that is for this values were the $\boldsymbol{\Phi_{T\rho}}$ is maximized.

.

4.2.3 Influence of the Zn flow

To determine the influence of the Zn flow on the transmittance and the resistivity of the thin ZnO films, different samples were deposited in which the ion current and oxygen flow were kept constant and variations of the Zn flow were made from 0.6 to 2.6 Å/s. Additionally a quality criterion or merit figure was established $\boldsymbol{\Phi_{T\rho} = -1/(\rho * lnT)}$ that allow to obtain a good balance between the **ρ** and **T**.

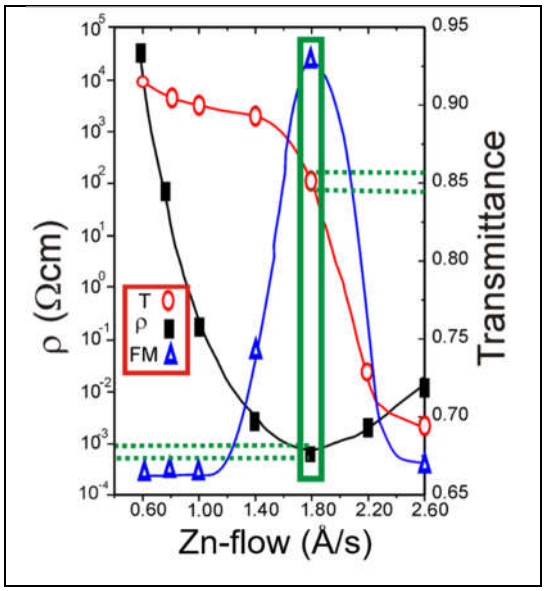

Figure 4.5 Variation of resistivity, transmittance (at 700 nm) and figure of merit (quality criteria $\boldsymbol{\Phi_{T\rho}}$) of ZnO thin films as a function of Zn-flow.

Finally a study was done to determinate the influence of Zn flow in the transmittance (T) and resistivity (ρ) of the ZnO thin film; for that, the ion current was kept constant at 2 mA and the oxygen flow at 15 ml/min. The results of Figure 4.5 indicate that the variation of the Zn flow is the parameter that most strongly influences

both the transmittance and the resistivity of the ZnO thin films. It is observed that the resistivity decreases as Zn-flow increases; this phenomenon is due to the fact that the increase in Zn-flow is associated with an increase in the supply of zinc, which has an impact on the increase in the Zn^{+}/O^{-} ratio that leads to an increase in the density of oxygen vacancies, which in turn results in an increase in the concentration of free carriers and therefore in the conductivity of the thin ZnO films.

In samples prepared with excess Zn, the conductivity and the transmittance strongly decrease as the amount of Zn increases over values corresponding to Zn flow = 1.8 Å/s. This behavior has been associated to generation of a high density of defects caused by the presence of Zn in interstitial positions. These defects give rise to active states within the gap which contribute to photon absorption in the entire spectral range studied. On the other hand, the decrease of conductivity observed when Zn flow is greater than 1.8 Å/s, has been attributed to a decrease of the mobility, apparently due to scattering of free carriers with defects generated by Zn in interstitial positions.

The low transmittances observed for Zn flow greater than 1.8 Å/s indicate that the density of donor states associated with oxygen vacancies is sufficiently high to have a significantly contribution in the absorption of photons with lower energies than the gap one; This is due to the fact that when the zinc supply increase, a high density of interstitial defects is produced, which generate absorption centers that give rise to a decrease in transmittance. From the variation of the $\boldsymbol{\Phi_{T\rho}}$ observed with the variation of Zn flow it can be concluded that to deposit ZnO thin films which simultaneously exhibit high transmittance and high conductivity, it is necessary to use Zn flow around 1.8 Å/s that results in a maximized $\boldsymbol{\Phi_{T\rho}}$.

Figure 4.6 shows the spectral transmittance of a typical thin film of ZnO deposited under optimal conditions (I=2 mA, O2-flow= 12 ml/min. and Zn-flow=1.8A/s), which exhibits simultaneously high transmittance (90% at 700 nm) and low electrical resistivity ($8x10^{-4}$ Ωcm).

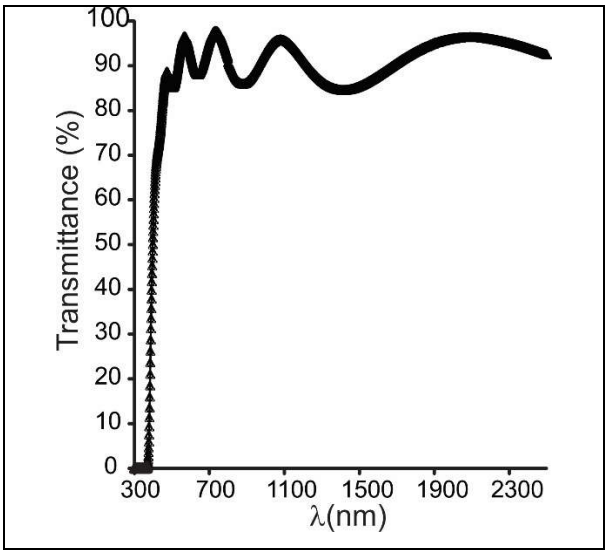

Figure 4.6 Spectral transmittance of a typical sample of ZnO, deposited under optimal conditions.

Were study the influence of the main deposition parameters of both, the electric resitivity $\boldsymbol{\rho}$ and transmittance T of the ZnO films. The best influence in the deposition conditions was quantified through a quality criteria that includes both the transmittance and resistivity, defined by the relation $\boldsymbol{\Phi_{T\rho} = -1/(\rho * lnT)}$. The study revealed that the amount of Zn-flow, the O_2-flow and the Ionization current (I) affect both the transmittance and the resistivity of the ZnO films. The influence of Zn-flow, O_2-flow and I on ρ, T and $\boldsymbol{\Phi_{T\rho}}$ *was* presented. The transmittance measurements were carried out using a Varian-Cary 5000 spectrophotometer and the electrical conductivity was measured using the four-probe method.

The PARE process have an special characteristic that make it a very good option for ZnO thin film preparation, this is that during the process it is possible modified the final properties of the thin films by adding or removing oxygen vacancies by controlling the relation Zn^+/O^- ratio. Based on the results presented in this chapter we can highlight the following facts: The three studied parameters affect both the transmittance and the resistivity of the ZnO films, being Zn-flow the parameter that most strongly affects these two properties, However the influence O_2-flow is also very notorious due that the fact that both Zn-flow and O_2-flow affect Zn^+/O^- ratio which is directly associated with oxygen vacancies, which has an impact in the opto-electrical properties. In all the experimental results it is possible to observe that there is an ideal Zn^+/O^- ratio, by properly selecting the values of Zn-flow and O_2-flow in order to keep this ratio in the ideals values and programming the deposition system following an optimal deposition routine, it is possible to grow highly transparent ZnO films with resistivities less than 10^{-3} Ωcm and transmittance greater than 85%.

Those studies will be use in the next chapter to give additional information at process model and help with the definition of the operating constraints and quality criteria in the dynamic optimization problem.

Chapter 5

Dynamic optimization and control of Plasma Assisted Reactive Evaporation process

In chemical engineering, dynamic optimization approaches are used in optimal design and operation of processes that are transient in nature, e.g. semi-batch or batch reactors [75,76]. These approaches are based on process models that are very often described by means of algebraic-differential equations derived from mass and energy balances and thermodynamic and physical relations. The models should be accurate enough and not too complex in order to avoid numerical difficulties during their numerical integration [77].

Different methods are used to solve dynamic optimization problems. They include simultaneous (or full discretization) and sequential (or faisable-type) methods (Biegler, 1990). Moreover, they allow the determination of time-varying profiles of decision variables in open loop. These optimal profiles are then used as set points in the design of advanced control laws,

In this study, the dynamic optimization of the PARE process is considered. The objective is to determine the time-varying profile of temperature and zinc flowrate that minimize the batch time while meeting some quality product specifications, mainly on transmittance, resistivity and film thickness.

5.2 Dynamic optimization fundamentals

5.1 Problem definition

In dynamic optimization problems, there are two types of variables: *state* variables and *decision* variables. The state variables depend on the decision variables through the set of differential equations that constitute the process model, expressed as:

$$\dot{x} = f\,(x(t),\, u(t),\, t) \tag{5.1}$$

Frequently, state as well as control variables are subject to equality or inequality constraints, respectively $h(\cdot)$ and $g(\cdot)$, that should be satisfied in the optimization problem solution. They can be written respectively as

$$h\,(t,\, x(t),\, u(t),\, p) = 0$$
$$g\,(t,\, x(t),\, u(t),\, p) \leq\, 0 \tag{5.2}$$

Typically, the values that the decision variables can take in a dynamic optimization problem should be restricted to a control interval given as

$$u(t)\ \in [u^L(t), u^U(t)] \tag{5.3}$$

In addition, some unknown parameters p may also be involved in the process model equations as well as in the constraints. Their values lie also in an interval defined by a lower and an upper bound as

$$p \in [p^L, p^U] \tag{5.4}$$

Dynamic optimization problems can be written in terms of a performance index $J(u)$ (also known as cost f*unctional*) to be minimized subject to constraints under the following form

$$min_{u(t),p} \qquad J(u) = G\left(x(t_f)\right) + \int_{t_o}^{t_f} F(x(t),\, u(t),\, p, t)dt \vee$$

$$
\begin{aligned}
s.t \qquad & \dot{x} = f\,(x(t),\, u(t),\, t) \quad \forall t \in [t_o, t_f] \\
& x(t_0) = x_0 \\
& h\,(t,\, x(t),\, u(t),\, p) = 0 \\
& g\,(t,\, x(t),\, u(t),\, p) \leq 0 \\
& u(t) \in [u^L(t), u^U(t)] \\
& p \in [p^L, p^U]
\end{aligned} \tag{5.5}
$$

The performance index can always be represented as the sum of two terms, an algebraic term $G(\cdot)$ evaluated at initial and final conditions and the integral over a time interval of the function $F(\cdot)$ called a functional. x is the state vector. The constraints constitute a system of differential and algebraic equations (DAEs) that can be solved by different approaches.

The objective is to calculate such a continuously differentiable control function $u(t),\ t_o \leq t \leq t_f$, that will drive the system to some desired terminal condition.

The performance index depends on the problem that will be solved. In the following, some examples of the performance index forms typically used are given:

– Time minimization

$$J = \int_{t_o}^{t_f} dt = t_f \tag{5.6}$$

– State error variance minimization

$$J = \int_{t_o}^{t_f} (x(t) - x^{ref}(t))^2 dt \tag{5.7}$$

Where x^{ref} is the reference state.

– A combination of performance indexes

$$J = \int_{t_o}^{t_f} dt + \mu \int_{t_o}^{t_f} (x(t) - x^{ref}(t))^2 dt \tag{5.8}$$

-Lagrange form :

$$J = \int_{t_o}^{t_f} F(x(t), u(t), t)dt \tag{5.9}$$

The solution of the optimal control problems can be found by means of two main approaches, analytical methods and numerical methods.

5.1.1 Analytical methods

The most important analytical methods are derived from variational calculus for continuous systems, and dynamic programming (Bellman optimality principle) for discrete systems.

Variational calculus

Variational calculus is a field of mathematics that, given a functional $f = f(x, y, y')$, is focused on finding a function $y(x)$ which optimizes (minimizes or maximizes) the value of an integral J known as the *criterion or cost function or objective function*

$$J = \int_{x_1}^{x_2} F(x, y, y')dt \tag{5.10}$$

Subject to the boundary conditions

$$\begin{cases} y(x_1) = y_1 \\ y(x_2) = y_2 \end{cases} \tag{5.11}$$

Methods that use variational calculus are based on the first order necessary conditions for optimality obtained according to one of the three following main approaches: Euler equations, Hamilton-Jacobi equation and Pontryagin's Maximum (*or minimum*) principle. For the constraints, the method follows Euler-Lagrange differential equation which is used also for the formulation of the necessary conditions for the optimization problem. In that case, the necessary condition for the integral J to be optimal subjected to the boundary conditions (5.11) is that the function $y(x)$ satisfies the following *Euler-Lagrange* equation

$$\frac{\partial f}{\partial y} - \frac{d}{dx}\left(\frac{\partial f}{\partial y'}\right) = 0 \tag{5.12}$$

In principle, second order necessary conditions should be verified, such as Legendre-Clebsch equations. However, in practice, their verification is often difficult and consequently they are omitted.

Pontryagin's Maximum (or minimum) principle

Pontryagin's maximum (or minimum) principle (PMP) is another efficient approach to solve the optimization problem. The first order necessary conditions involve the optimality condition for the control variable, the definition of the adjoint variables and their terminal conditions [78,79]. There are some important issues to be considered in Pontryagin's Maximum principle [77] :

– It is not necessary to consider two neighbourhood controls in the whole admissible control domain.
– Control variables u_i
– The optimal control vector is composed of piecewise continuous functions. The main conclusion of the Pontryagin's minimum principle is that, at the optimal conditions, the control minimizes the Hamiltonian at each point in the time interval [79].

Dynamic Programming

Dynamic Programming is a general method used for dynamic optimization of systems described in discrete time. This method is based on the principle of optimality formulated by Bellman establishing that "*any subpolicy extracted from an optimal policy is itself optimal*". Here, the optimization problem is formulated as a sequence of decisions [80]. Dynamic programming technique was applied in several applications in chemical engineering, e.g. oil refineries, batch and semi-batch reactors, tubular reactors, among others [77]. The use of this method has been limited because of its high dimensionality. The problem of dimensionality is normally treated by using a very coarse grid sufficiently accurate for the calculation purpose. Although dynamic programming method is slower than some gradient-based algorithms, it can be used to cross-check results of small problems [75,80].

5.1.2 Numerical methods

Generally, in dynamic optimization problems, the equations of the performance index, constraints and dynamic model are nonlinear and as a consequence, it is difficult to obtain analytical solutions. The numerical methods are therefore used and can be classified into two main categories: *indirect methods* and *direct methods*.

However, there exist also other approaches like *dynamic programming* methods for discrete systems and *stochastic* methods for uncertain systems that are not discussed in this document.

Indirect Methods

This kind of methods search for a minimum of the objective function indirectly, by solving the first order necessary conditions of optimality obtained from Pontryagin's Maximum Principle. For this reason, these methods are also known as *variational methods* [81,82]. The two most well known methods in this category are the *Boundary Condition Iteration (BCI)* and *Control Vector Iteration (CVI)*. In the CVI method, the initial control vector is chosen and the system of state equations is integrated. Then the equations of the adjoint variables are also integrated with respect to time [77]. Finally, using a gradient method, it is possible to estimate the new control vector according to the expression

$$u^{k+1}(t) = u^{k}(t) + \propto \frac{\partial H}{\partial u} \tag{5.13}$$

In the case of problems without inequality constraints, the conditions can be written as a set of DAEs. Special attention should be drawn to the boundary conditions. Normally, initial conditions are specified for the state differential equations, whereas only final conditions are available for the adjoint system. As a result, a two-point boundary value problem (TPBVP) is obtained whose solution can be addressed using different techniques, including single shooting, invariant embedding, collocation on finite elements or finite differences [75,83].

Direct Methods

In order to avoid the difficulties associated to the indirect methods, *direct optimization* methods have been extensively studied and used over the last 40 years showing high efficiency in the solution of practical dynamic optimization problems. This kind of methods use only control and/or state variables as optimization variables. The principle of the method is the *discretization* of the control problem, and then Nonlinear Programming (NLP) techniques are used to solve the resulting finite-dimensional nonlinear optimization problem [81, 84,85]. Direct methods that use NLP solvers can be divided into two categories, *sequential* and *simultaneous* strategies. The *sequential* strategy, also known as *control vector parameterization* (CVP), consists in an approximation of the control trajectory by a function of few parameters and maintaining the state equations in the form of the original ODE/DAE system [86]. Reliable DAE solvers (e.g., DASSL, DASOLV, DAEPACK) as well as NLP solvers (NPSOL, SNOPT) can be used in the sequential strategies [75,87]. Some of the

disadvantages of the sequential methods are related to the repeated numerical integration of the DAE model, which may become time consuming for large-scale problems. In addition, the sequential approach has properties of single shooting methods that cannot handle open loop instability.

The *simultaneous method* also known as *multiple shooting*, uses the discretization of both the control and state variables in time using collocation on finite elements or finite differences. For this reason, this approach is also known as *full discretization* techniques [75,81, 84]. This method can be considered as a connection between sequential and simultaneous approaches. The simultaneous approach leads to large-scale NLP problems that require more sophisticated optimization strategies. As a consequence, the optimization problem and the solution of the DAE system are coupled and the DAE system is solved only once, at the optimal point, in order to avoid intermediate solutions that may require excessive computational effort [80, 81]. In this work, the sequential method was used to solve the dynamic optimization problem. Initially, it is important to find a suitable way to parameterize the control variables [86,88]. One alternative is to subdivide the optimization horizon $[t_0, t_f]$ into $n_t \geq 1$control intervals

$$t_0<t_1<t_2< \ldots <t_{n_t} = t_f,$$

and then to use low-order polynomials on each interval of the form

$$u(t) = U^k(t, w^k), \qquad t_{k-1} \leq t \leq t_k,$$

Lagrange polynomials are commonly applied to approximate the control variables into the intervals [79, 84, 88]. In interval k, the *j*th control variable is given by

$$u_j(t) = U_j^k(t, w^k) = \sum_{i=0}^{M} w_{ij}^k \, \emptyset_i^{(M)}(\tau^{(k)}), for\ t_{k-1} \leq t \leq t_k \tag{5.14}$$

Where $\tau^{(k)} = \frac{t-t_{k-1}}{t_k-t_{k-1}} \epsilon [0,1]$ is the normalized time stage k and $\emptyset_i^{(M)}(\cdot)$ is the Lagrange polynomial of order *M*

$$\emptyset_i^{(M)} = \begin{Bmatrix} 1, & if\ M = 0 \\ \prod_{\substack{q=0 \\ q \neq i}}^{M} \frac{\tau-\tau_q}{\tau_i-\tau_q}, & if\ M \geq 1, \end{Bmatrix} \tag{5.15}$$

With collocation poins $0 \leq \tau_0 < \tau_1 < \cdots < \tau_M \leq 1$. If $M = 0$, piecewise constant constrols are obtained, and if $M = 1$, picewise linear controls are considered. Figure 5.1 shows examples of differents types of picewise constrols used in dynamic optimization.

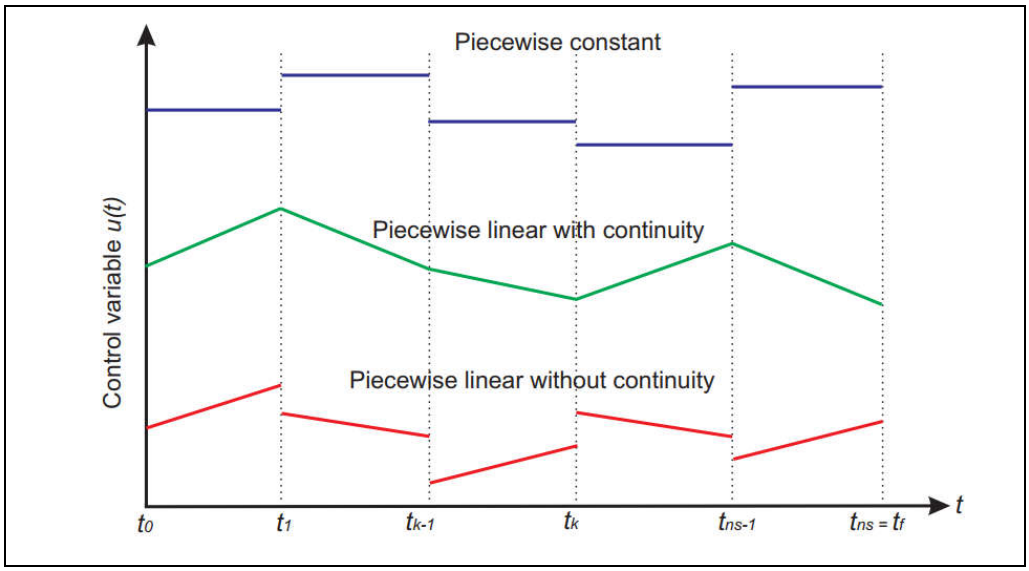

Figure 5.1 Example of different types of piecewise controls

5.2 Dynamic optimization of Plasma Assisted Reactive Evaporation process

The most important objective in thin film industry for solar energy technology is to maximize the productivity taking into account the quality and environmental constraints. For this reason, the optimization and control of the PARE reactors used in this industry are of great interest. The formulation of an optimization problem for the PARE reactor requires the definition of an objective function or performance index and some constrains that describe the process model equations and the final thin film properties.

In this work, the objective is to determine the time-varying profiles of zinc and oxygen flowrates that minimize the batch period while keeping Zn^+/O^- ratio in a specified interval (i.e. quality constraint) and achieving a final thickness of the film of 750nm. To our knowledge, this optimization problem has never been studied or reported in the open literature. The computation of its solution will be carried out by means of the CVP optimization method described above and will be based on the process model presented in chapter 3 and experimental studies discussed in chapter 4.

5.2.1 Case study: plasma assisted reactive evaporation process

The case study considered here corresponds to a pilot reactor for a Plasma Assisted Reactive Evaporation (PARE) process operated at the Semiconductor Materials and Solar Energy Research Group (SM&SE) of the Universidad Nacional de Colombia. More specifically, the dynamic optimization of a pilot reactor for synthesis and deposition of Zinc Oxide (ZnO) thin films is developed. The PARE process consists in evaporating Zn in the presence of oxygen, so that a chemical reaction occurs which leads to the formation of the ZnO thin films. Since Zn oxidizes very slowly in the presence of O_2 at room temperature, it is therefore necessary to ionize both Zn and O_2 to accelerate the chemical reaction between these two species. The ionization process is achieved through a glow discharge (GD). When zinc vapor enters the region where the oxygen plasma is confined, the precursor ionized species (Zn^+, O^-) react to form ZnO molecules. The resulting ZnO molecules and the unreacted excess of Zn are then transported by convection and diffusion on the substrate surface where they condense and form the thin film, leading to a sharp decrease of the partial pressure inside the chamber.

In the previous chapters the modeling and simulation of this reactor was performed. The state space dynamic model $\dot{x} = f\ (x(t),\ u(t),\ t)$ describing the process corresponds to

$$\boldsymbol{v_{r,i}(z,r) = \frac{V_{w,i}}{L} r\left[-\frac{3}{4}\psi^2 + \frac{3}{4} + Re_{w,i}\left(-\frac{1}{160}\psi^6 + \frac{3}{32}\psi^4 + \frac{1}{4}\psi^3 - \frac{117}{1120}\psi^2 - \frac{1}{4}\psi + \frac{19}{1120}\right)\right]}$$

$$\boldsymbol{v_{z,i}(z) = V_{w,i}\left[-\frac{1}{4}\psi^3 + \frac{3}{4}\psi + \frac{1}{2} + Re_{w,i}\left(-\frac{1}{1120}\psi^7 + \frac{3}{160}\psi^5 + \frac{1}{16}\psi^4 - \frac{39}{1120}\psi^3 - \frac{1}{8}\psi^2 + \frac{19}{1120}\psi + \frac{1}{16}\right)\right]}$$

$$\boldsymbol{i = 1\ and\ 4} \tag{5.16}$$

$$\boldsymbol{\frac{\partial c_i}{\partial t} = D_i\left(\frac{\partial^2 c_i}{\partial r^2} + \frac{1}{r}\frac{\partial c_i}{\partial_r} + \frac{\partial^2 c_i}{\partial z^2}\right) - \left(v_{r,O_2} + v_{r,Zn}\right)\frac{\partial c_i}{\partial_r} - \left(v_{z,O_2} + v_{z,Zn}\right)\frac{\partial c_i}{\partial_z} + r_{x,i}\ (n_e, C_1, C_2, C_3\ , C_4, C_5, C_6)\ \ i = 1, \dots, 6} \tag{5.17}$$

$$\boldsymbol{R_{dep}(t,r) = \frac{1}{\rho_{ZnO}}\left[\sum_{i=1}^{6} s_i\, D_i \frac{\partial c_i}{\partial_z}(t, r, L)\right]} \tag{5.18}$$

$$\boldsymbol{R_{avg}} = \frac{\sum_{r=0}^{r} \boldsymbol{R_{dep}}}{\mathbf{75}} \quad (5.19)$$

$$\boldsymbol{T} = \boldsymbol{t_t}/\boldsymbol{N_u} \quad (5.20)$$

$$\boldsymbol{S} = \frac{\boldsymbol{V_{w,Zn}^{n} - V_{w,Zn}^{n-1}}}{\boldsymbol{T(N_u^n - N_{u,}^{n-1})}} \qquad \boldsymbol{n} = \mathbf{1}, \dots, \boldsymbol{N_u} \quad (5.21)$$

$$\boldsymbol{\Phi_{T\rho}} = \mathbf{665} + \frac{\mathbf{4740}}{\mathbf{0.6627}\sqrt{\boldsymbol{\pi}/\mathbf{2}}}\boldsymbol{e}^{-\mathbf{2}*(\frac{\boldsymbol{V_{w,Zn}}-\mathbf{1.8}}{\mathbf{0.6627}})^{\mathbf{2}}} \quad (5.22)$$

Where:

$[x_1, x_2, x_3, x_4, x_5, x_6, x_7, x_8, u_1, u_2, u_3\ P_1] = [C_1, C_2, C_3, C_4, C_5, C_6, R_{dep}, R_{avg}, \Phi_{T\rho}, V_{w,Zn}, V_{w,O_2}, S]$.

The resulting dynamic optimization problem is transformed into a non-linear programming (NLP) problem using the CVP method, i.e. the control variables are approximated by means of piecewise constant functions. It is then implemented within Matlab and solved using *fmincon* optimizer.

Two different optimization problems are considered. In the first problem, only Zn flow rate $(V_{w,Zn})$ is taken as control or decision variable $u(t)$, whereas in the second problem, both Zn flow rate $(V_{w,Zn})$ and Oxygen flow rate V_{w,O_2} are considered. Quality constraints are deduced from experimental studies that were performed in order to determine the final product properties such as Transmittance, Resistivity and Thickness of the zinc oxide film.

5.2.2 Operating conditions: plasma assisted reactive evaporation process

In PARE process, the source of Zn is obtained by evaporation of zinc in solid state, using a Knudsen cell,It is noteworthy that Zn flowrate is directly linked to the Knudsen cell temperature (experimental results were presented in chapter 2). The best way to control the amount of Zn arriving in the GD region is to control the evaporation of Zn carried in two steps. In the first one, the temperature ramp of the Knudsen cell is controlled up to reaching a temperature of 400°C in order to prevent the obstruction of the exit whole of the cell due to the high vapor pressure of Zn. At the same time, the chamber is fed with an O_2 flowrate of 12 mil/min, which is controlled through a flow mass controller reaching a partial pressure of around 0.040 mBar. When this temperature is reached, the second step, which mainly consists in the control of the zinc , begins. An indirect measurement of Zn flowrate is achieved through a pressure sensor which indicates the change in pressure

due the reaction of Zn and O_2. Figure 5.2 shows the typical profiles of the Knudsen cell temperature and partial pressure DP to deposit thin ZnO films.

.

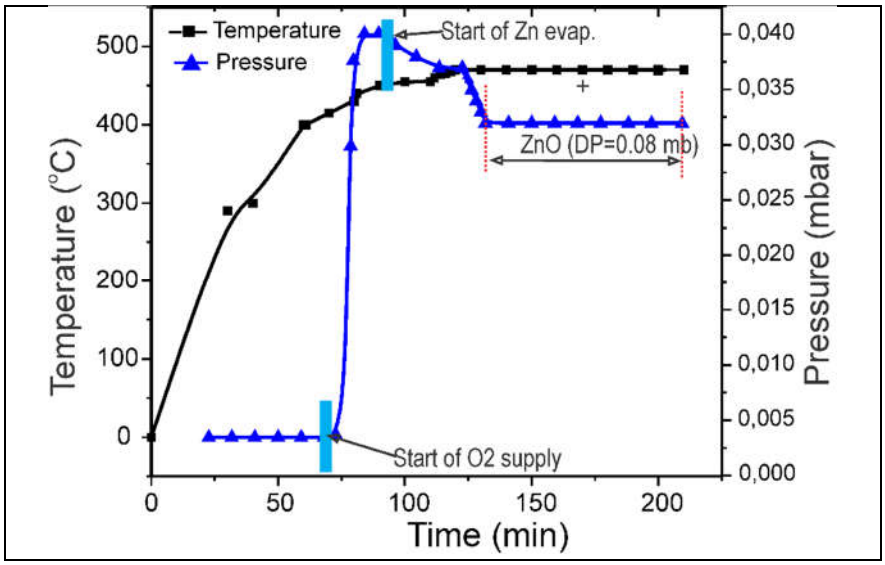

Figure 5.2 Typical profiles of the Knudsen cell temperature and the partial pressure change DP that allow depositing ZnO with thicknesses, transmittances and resistivities suitable to be used as optical window of solar cells.

In dynamic optimization computations carried out in this study, the pre-heating step is not taken into account. At the end of this step, the Knudsen cell temperature and Zn flowrate reach the values of 440 °C and $0.4\ (\text{Å}/s)$ respectively. Under these conditions, the reaction is assumed to start thus corresponding to the initial reaction time $t = 0$ which is difficult to determine precisely. On the other hand, since the zinc flowrate is raised by increasing the temperature of the Knudsen cell, a constraint on the rate of change of the zinc flowrate is imposed in order to account for the temperature inertia. The process ends when the ZnO thin film reaches a thickness value of 750 nm.

5.2.3 Batch time minimization with Zn flow as control variable

In order to minimize the final batch time of the PARE reactor, the optimal Zn flow rate is calculated. $V_{w,Zn}$ is chosen because its large influence on the optoelectrical properties of the ZnO films. The formulation of the optimization is presented below

$min_{V_{w,Zn},t}$ t_f

$s.t$ $\dot{x} = f_i\left(x(t), V_{w,Zn}(t), t\right)$ $i = 1, \dots, 8$ and $\forall t$ $\tau \in [t_0, t_f]$

$x_i(t_0) = c_i^0$, $i = 1, \dots, 8$ initial conditions

$R_{avg}(t_f) = 750\ nm$ Final thickness

$V_{w,O_2} = 12\ (mil/min)$

$S \leq 12.5 \times 10^{-3}$

$\Phi_{T\rho} \geq 4.00 \text{ x}10^3$

$0.4\ (\text{Å}/s) \leq V_{w,Zn}(t) \leq 1.9\ (\text{Å}/s)$ Zn flow rate Interval

Table 5.1 – Optimization results for time minimization using as a control variable the Zn flow rate.

N_u	$t_f\ (s)$	$\Phi_{T\rho}\ (1\text{x}10^3)$	$Final\ thickness\ (nm)$
5	5255	4.0401	750
10	5169	4.4697	750
25	4937	4.8518	750

The influence of the number of time segments is investigated. Moreover, three different values of N_u are considered, i.e. 5, 10 and 25. Values higher than 25 does not show significant differences.

Table 5.1 presents the results obtained for the values of the number of time segments considered. It compares the final time, the quality criterion $\Phi_{T\rho}$ and the thin film thickness. As expected, when the number of discretization segments increases, the batch time is reduced and the quality index Φ_{TR} of the ZnO thin film increases. The last column of the table shows that the thickness constraint is always fulfilled. It is noteworthy that 25 discretization segments achieve the lowest final time (t_f) and highest Φ_{TR}. This is due to the fact that the Zn flowrate reaches its maximum value in the shortest time thus increasing the deposition rate.

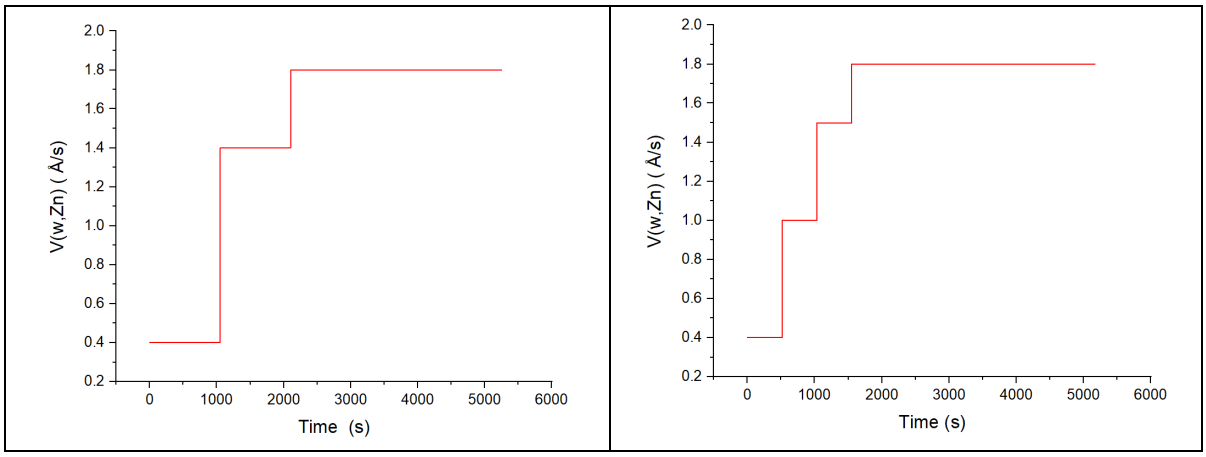

(a) $N_u = 5$ **(b) $N_u = 10$**

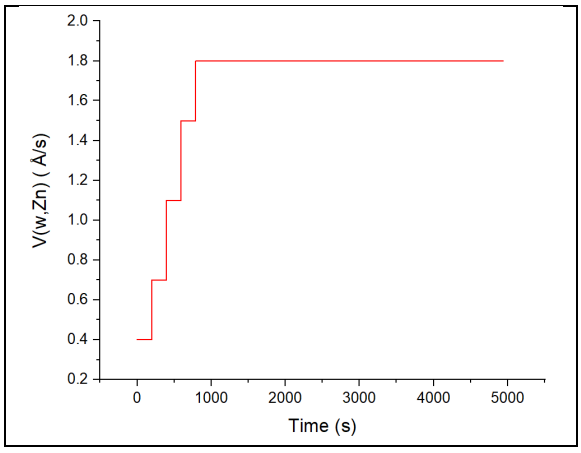

(c) $N_u = 25$

Figure 5.3 Optimal Zn flow profile for the time minimization

.

The optimal profiles of Zn flowrate for different values of N_u are presented in figure 5.3. It can be seen that in the three optimization cases, the value of the decision variable in the first segment is 0.4 $(\text{Å}/s)$. This is due to the fact that the reaction is assumed to start at this value which corresponds to the instant when the Knudsen cell temperature reaches 440°C, i.e. initial time t_0. It can also be seen that the constraint imposed on the rate of change of Zn flowrate results in a gradual increase in each interval until it reaches the maximum value of 1.8 $(\text{Å}/s)$. The final time t_f is then achieved when the thin film thickness constraint is satisfied.

5.2.4 Batch time minimization with Zinc flow and 0xygen flow as control variables

In order to minimize the final batch time of the PARE reactor, i.e. maximize the productivity, the optimal profiles of zinc and oxygen flowrates are determined. $V_{w,Zn}$ and V_{w,O_2} are chosen because their large influence on the thin film opto-electrical properties. The optimization problem is formulated as

$$min_{V_{w,Zn},V_{w,O_2},t} \qquad t_f$$

$$s.t \qquad \dot{x} = f_i\left(x(t), V_{w,Zn}(t), t\right) \qquad i = 1,\dots,8 \ and \ \forall t \quad \tau \in [t_0, t_f]$$

$$x_i(t_0) = c_i^0, \ \ i = 1,\dots,8 \ \text{initial conditions}$$

$$R_{avg}(t_f) = 750\ nm \quad \text{Final thickness}$$

$$S \leq 12.5 \times 10^{-3}$$

$$V_{w,Zn}/V_{w,O_2} \leq 0.15$$

$$0.4\ (\text{Å}/s) \leq V_{w,Zn}(t) \leq 1.9\ (\text{Å}/s) \quad \text{Zn flow rate Interval}$$

$$10\ (mil/min) \leq V_{w,O_2}(t) \leq 20\ (mL/min) \quad \text{Oxygen flow rate Interval}$$

The values of the Zn flow rate Interval $(V_{w,Zn})$ and Oxygen flow rate Interval (V_{w,O_2}) are determinated by the operational conditions of the reactor, in the case of Oxygen flow rate, $10\ (mL/min)$ and $20\ (mL/min)$ are respectively the minimum and maximum values that could be fixed in the flow mass controller. In the case Zn flow rate $0.4\ (\text{Å}/s)$ and $1.9\ (\text{Å}/s)$ are respectively the minimum and maximum values that could be achieved in function of the Knudsen cell temperature control.

Table 5.2 Optimization results for time minimization using as a control variables Zn flow rate and oxygen flow rate.

N_u	$t_f\ (s)$	$V_{w,Zn}/V_{w,O_2}$	$Final\ thickness\ (nm)$
5	5222	0.1211	750
10	5159	0.1299	750
25	4905	0.1370	750

Here also, the influence of the number of time segments is investigated. Moreover, three different values of N_u are considered, i.e. 5, 10 and 25. Values higher than 25 do not show significant differences.

Table 5.2 presents the results obtained for the values of the number of time segments considered. It compares the final time, the ratio $V_{w,Zn}/V_{w,O_2}$of zinc and oxygen flowrates, the quality criterion $\Phi_{T\rho}$ and the thin film thickness. As expected, when the number of discretization segments increases, the batch time is reduced and the ratio $V_{w,Zn}/V_{w,O_2}$ and quality index Φ_{TR} of the ZnO thin film increase. The last column of the table shows that the thickness constraint is always fulfilled. It is noteworthy that the ideal value of the ratio $V_{w,Zn}/V_{w,O_2}$ was determined from experimental studies presented in chapter 4 and was around 0.15. On the other hand, the number of 25 discretization segments achieve the lowest final time (t_f) and highest values Φ_{TR} and $V_{w,Zn}/V_{w,O_2}$.

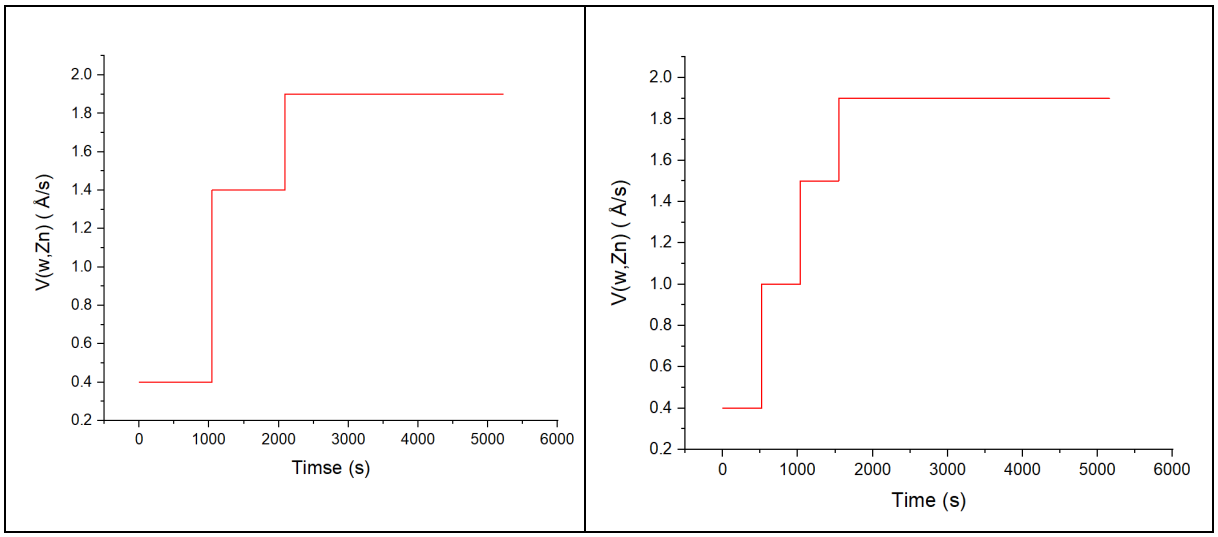

(a) $N_u = 5$ **(b) $N_u = 10$**

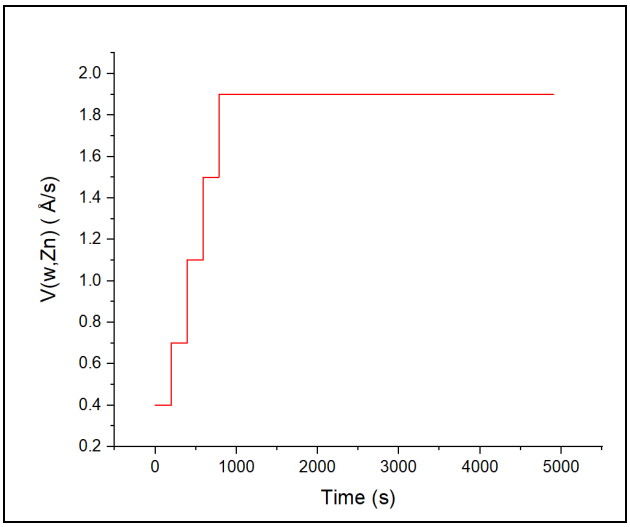

(c) $N_u = 25$

Figure 5.4 Optimal Zn flow profile for the time minimization

.

The optimal profiles of Zn flowrate for different values of N_u are presented in figure 5.4. It can be seen that in the three optimization cases, the profiles exhibit the same behavior as in the previous section in terms of initial value and gradual increase. However, the zinc flowrate hits the constraint upper bound of $1.9\ (\text{Å}/s)$. This can be explained by its interaction with the oxygen flowrate which increases in order to keep the ideal value of $V_{w,Zn}/V_{w,O_2}$ratio, i.e. 0.15. The use of zinc and oxygen flowrates as decision variables achieve the lowest value of the final time t_f obtained when the thin film thickness constraint is satisfied.

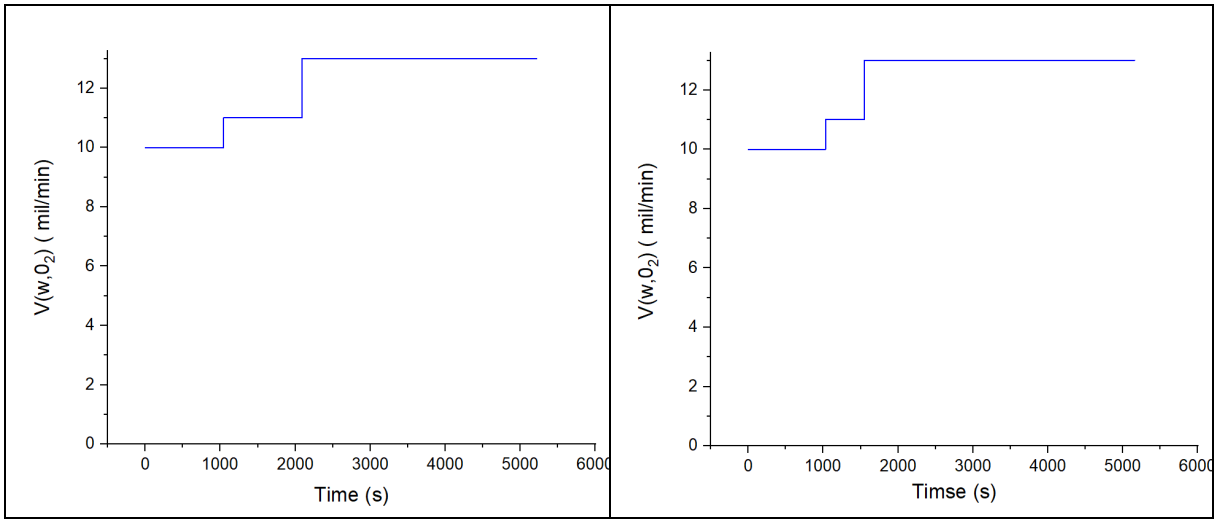

(a) $N_u = 5$ **(b) $N_u = 10$**

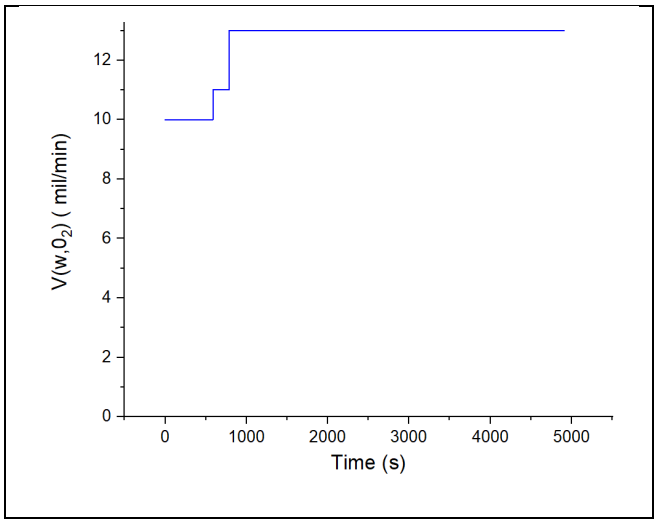

(c) $N_u = 25$

Figure 5.5 Optimal O2 flow profile for the time minimization

In this chapter, the dynamic optimization of Plasma Assisted Reactive Evaporation process was studied. In the first section of the chapter a fundamental review of dynamic optimization was

presented. This review included typical objective functions used and different numerical and analytical methods to solve the optimization problem. Two different optimization problems where the goal was to minimize the reaction time were considered. The simple one using only one decision variable and a more complex one with two decision variables. From the results it was concluded that the most efficient results were obtained when both zinc $V_{w,Zn}$ and oxygen V_{w,O_2} flowrates were used at the same time as decision variables. 15% of reduction in the batch time with respect to the normal operating conditions applied at the semiconductor material and solar cell research group was achieved. From those results it was also concluded that it was possible to reduce the batch time while keeping the thin film qualities (Transmittance, Resistivity and thickness) in the desired values

The dynamic optimization results will be used in the next chapter as setpoint trajectories to design an advanced controller in order to accurately control the reactor zinc and oxygen flowrates.

Chapter 6

Regulatory Control of Plasma Assisted Reactive Evaporation process

The control of the of Plasma Assisted Reactive Evaporation process is a difficult task due to the complexity of the physico-chemical phenomena involved in the process and the sensitivity to the disturbances that the system presents. As the thin films of ZnO are planned to be used as optical window in solar cells, the final properties are related to the resistivity and the transmittance. In the PARE process, there are disturbances associated with changes in raw materials and unexpected environmental conditions, such as the fact that the temperature at which the Zn evaporates changes significantly with the absorbed humidity. Accurate and reproducible control of the amount of Zn that reaches the glow discharge zone is very difficult to obtain, mainly due to the high vapor pressure of Zn. Taking into account the difficulties associated with the control of Plasma Assisted Reactive Evaporation process which are related to the disturbances in the feed stream of the Zn flow and the necessity to keep an ideal oxygen flow/zinc flow ratio, a regulatory control (RC) architecture is developed. In this section, a control simulation in Simulink of the optimal conditions obtained in Chapter 5 is presented.

6.1 Regulatory Control

The regulatory control architecture is used to maintain the flow rate of one stream in a process at a defined or specified ratio with respect to another. This control strategy is normally used when one of the flows is

sensitive to disturbances. Therefore, in order to keep a desired flow ratio in the process, the second flow is going to change an a function of the first flow changes. A common application of ratio control is to combine or blend two feed streams to produce a mixed flow with a desired composition or physical property [90]. It is a particular type of feed forward control that has had widespread applications in the process industries. Typical applications of regulatory control include:

- Setting the relative amounts of components in blending operations.
- Maintaining a stoichiometric ratio of reactants in a reactor.
- Keeping a specified reflux ratio for a distillation column.
- Holding the fuel-air ratio at the optimum value in a furnace.

In this chapter we are going to discuss two different possible methods to develop a regulatory control architecture. The conceptual diagram presented in figure 6.1 shows the Method I. In this case, the flow rate of one of the streams feeding the mixed flow, is designated as the ***disturbance stream (d)*** and is the stream that normally presents unexpected changes during normal operation.

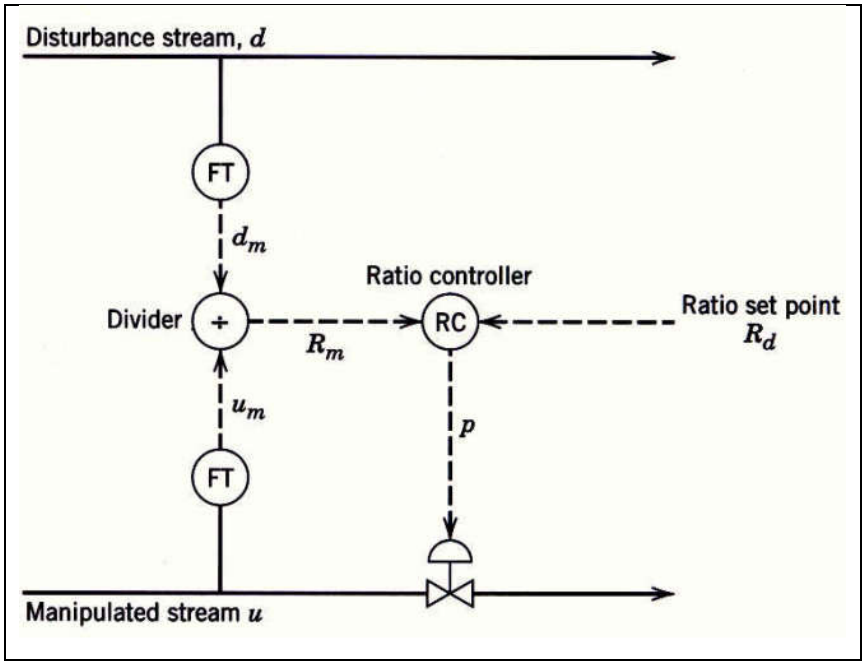

Figure 6.1 Conceptual diagram for regulatory control (Method I) [90].

The other stream feeding the mixed flow is designated as the ***manipulated stream (u)***. In this method the two streams are linked through a divider element whose output goes to the ratio control element where it is compared to the ratio set point. This comparation results in a signal error which drives the action of the control. Thus, the ratio is controlled rather than the individual variables.

$$R = u/d \tag{6.1}$$

The main advantage of Method I is that the actual ratio R is calculated using Eq. 6.1. A key disadvantage is that the divider element must be included in the control loop, varying thus the process gain in a nonlinear manner. From Eq. 6.1, the process gain is inversely proportional to the disturbance flow rate $\boldsymbol{d}$. Because of this significant disadvantage, the preferred scheme for implementing regulatory control is Method II, which is shown in Fig. 6.2

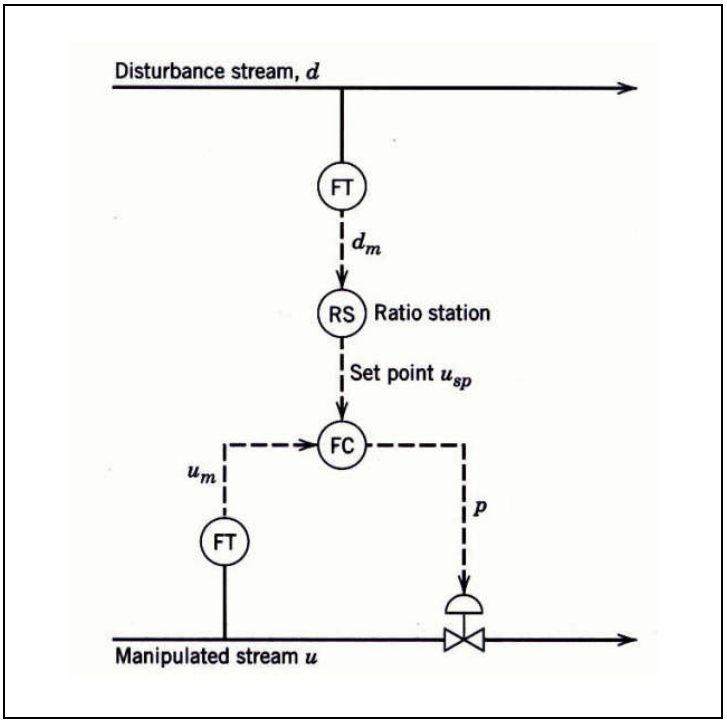

Figure 6.2 Conceptual diagram for regulatory control (Method II) [90].

Regardless of regulatory control is implemented, the process variables must be scaled appropriately. For example, in Method II the gain setting for the ratio station K_d must take into account the spans of the two flow transmitters. Thus, the correct gain for the ratio station is

$$K_R = R_d \frac{S_d}{S_u} \tag{6.3}$$

where R_d is the desired ratio, S_u and S_d are the spans of the flow transmitters for the manipulated and disturbance streams, respectively.

Taking into account the characteristics of Plasma Assisted Reactive Evaporation process in which is necessary to achieve a control that allows to get an optimal value of the Oxygen flow/Zinc flow ratio, the regulatory control (RC) is a great option for this process. In order to implement the regulatory control for the

Plasma assisted reactive evaporation process, first it is necessary to understand the feedback effects which are commonly used for any control strategy.

6.2 Feedback effects

A system with a process that acts on the input signal and produces an output signal depending only on the input, is known as open-loop system. On the contrary, when the output signal is fed back to a controller that produces specific control actions which modify the response of the system, the system is referred to as closed-loop system. In the development of processes, it is generally required that certain variables (temperature, velocity, pressure, etc.) meet specific ranges or values to achieve optimal conditions in the outcome of the process. This is usually achieved through the implementation of electronic control strategies that allow to fulfill these conditions. It is therefore necessary that the system has information on the state of the variables at the exit, which implies that a feedback is involved.

Considering that many control systems are multivariable, the characteristics and advantages of feedback can be illustrated by considering a simple feedback loop, and these can be extended to more complex control loops. Figure 6.3 shows the schematic representations of open-loop and closed-loop systems.

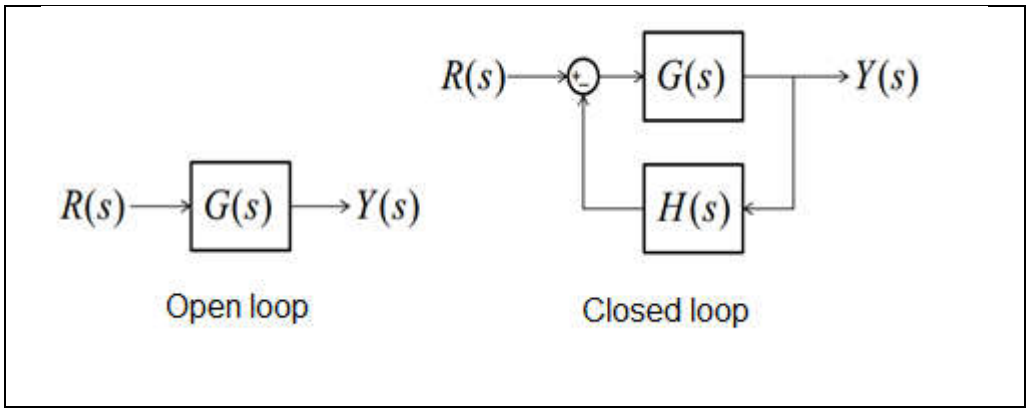

Figure 6.3 Open and closed loop systems [92].

The main difference between an open-loop and a closed-loop system is the generation and use of the error signal. The closed-loop system operates in such a way that the error is reduced to a minimum value. The signal $E(s)$ is a measurement of the error acting on the system and is equal to the error $E(s) = R(s) - Y(s)$ when $H(s) = 1$ [92].

The output in open-loop is expressed as

$$Y(s) = G(s)R(s) \tag{6.4}$$

In closed-loop, it is given by

$$Y(s) = G(s)E_a(s) = G(s)[R(s) - H(s)Y(s)] \tag{6.5}$$

And,

$$Y(s) = \frac{G(s)}{1+GH(s)}R(s) \tag{6.6}$$

The acting error signal is represented by the following relationship:

$$E_a(s) = \frac{1}{1+GH(s)}R(s) \tag{6.7}$$

It is then clear that in order to reduce the error in the control system, the magnitude of $1 + GH(s)$ must be much greater than one in the entire range of importance of $\boldsymbol{s}$. It is also observed that the total gain of the closed-loop system is reduced by the factor $(1 + \mathrm{GH}(\mathrm{s}))$ and the corresponding poles are given by the roots of $1 + \mathrm{GH}(\mathrm{s}) = 0$.

6.2 Modeling and Identification

Before proceeding to the design of a control algorithm, it is necessary to analyze the static and dynamic characteristics of the plant to be controlled in the temporal domain, which is achieved by applying different methods and/or technique. In linear systems, the transfer function can be obtained from the experimental response obtained. Moreover, the systems can be classified in first order and second order:

i) First Order Systems

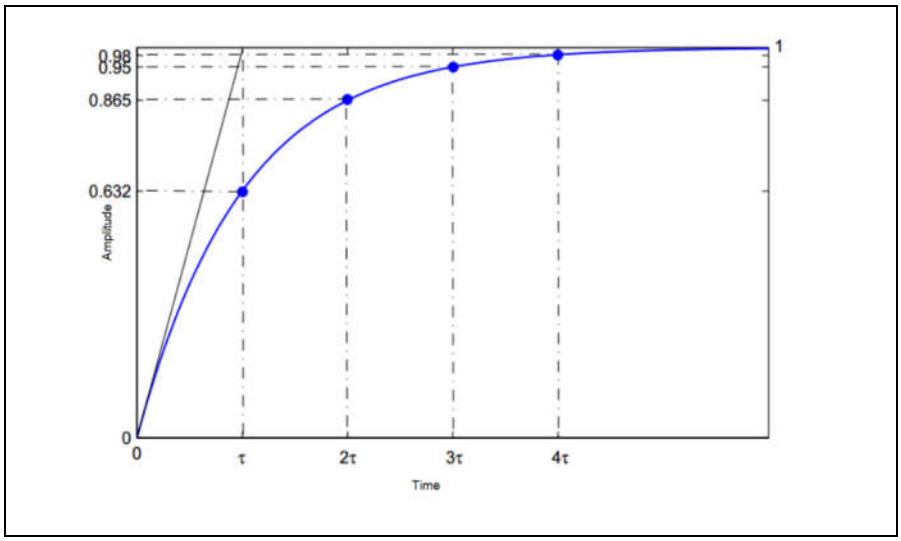

Figure 6.4 First order systems response [93].

The step type of signal is the most commonly used signal to excite the dynamics of the systems. The first order systems can be generally described by the following transfer function [92,93]:

$$G(s) = \frac{Y(s)}{R(s)} = \frac{k}{\tau s+1} \tag{6.8}$$

where k, is the static gain of the system. It is determined by the ratio of variations of output and input at steady-state as :

$$k = \frac{\Delta output_{ss}}{\Delta input_{ss}} \tag{6.9}$$

$\boldsymbol{\tau}$ is the duration it takes for the response of the system to reach 63.2% of its final value and represents the system time constant (see Figure 10).

Assuming that $\mathrm{R}(s)$ is a unit step, the inverse Laplace transform is applied to $\mathrm{Y}(s)$, as a result the response of the system is obtained in time domain is given as $Y(t) = k(1 - e^{t/\tau})$. Figure 6.4 shows that the response is an exponential curve whose stabilization time can be approximated to 4τ taking into account a tolerance band of 2%.

ii) Second Order Systems

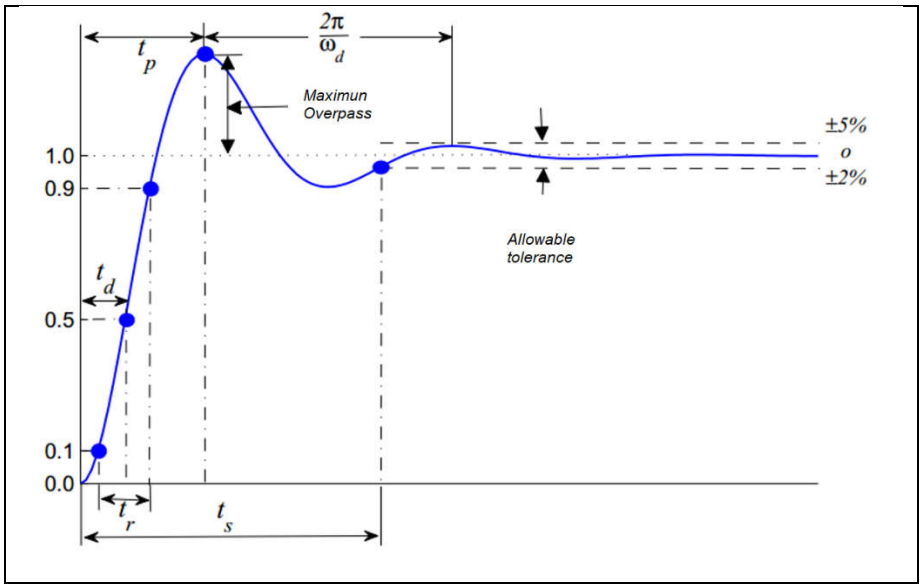

Figure 6.5 Second order system response [93].

The second order systems can be generally described by the following relationship [92-94]:

$$G(s) = \frac{Y(s)}{R(s)} = \frac{k{\omega_n}^2}{s^2+2\xi\omega_n+{\omega_n}^2} \tag{6.10}$$

where k, is the static gain of the system, ω_n is the natural undamped frequency of the system and ξ is the damping coefficient of the system ($0 < \xi < 1$).

The response of a second-order system when it is excited with a step type signal can be seen in Figure 6.5. From the experimental response, certain characteristics over time can be obtained, such as:

Time delay t_d: Time it takes the response to reach half of the final value for the first time. This time can be expressed by the following relationship:

$$t_d \cong \frac{1+0.7\xi}{\omega_n}, 0 < \xi < 1 \tag{6.11}$$

Rise time t_r: difference between the times that the response takes to reach 90% and 10% of the final value. This time can be expressed by the following relationship:

$$t_r \cong \frac{0.8+2.5\xi}{\omega_n}, 0 < \xi < 1 \tag{6.12}$$

Stabilization time t_s: is defined as the time when the response is no longer changing or is no longer changing significantly between ±2%. This time can be expressed by the following relationship:

$$t_s \cong \frac{3.2}{\xi \omega_n},\ 0 < \xi < 0.69 \tag{6.13}$$

$$t_s \cong \frac{4.5\xi}{\omega_n},\ \xi > 0.69 \tag{6.14}$$

Peak time t_p: Time in which the system reaches the first peak of the response. This time can be expressed by the following relationship:

$$t_p = \frac{\pi}{\omega_d} \tag{6.15}$$

Overpass M_p: is the percentage of maximum rebound of the response with respect to the total change in steady state output and is related to the cushioning coefficient as follows:

$$M_p = \frac{Maximun\ overpass}{\Delta y_{ss}} \tag{6.16}$$

$$M_p = e^{\frac{-\pi\xi}{\sqrt{1-\xi^2}}} \tag{6.17}$$

Natural damped frequency ω_d: The exponential term defines how quickly the system "damps" down – the larger the **damping** ratio, the quicker it damps to zero. It can be expressed by the following relationship:

$$\omega_d = \omega_n\sqrt{1-\xi^2} \tag{6.18}$$

$$\xi = cos\,\theta \tag{6.19}$$

6.3 PID controller

Once the dynamic and static characteristics in the temporal domain of the plant to be controlled is known, the algorithm could be chosen., In the control of industrial processes, PID controllers (proportional (P), integral (I) and derivative (D)) are the most used. To understand the operation of a PID controller, it is necessary to consider the feedback system presented in Fig. 6.6:

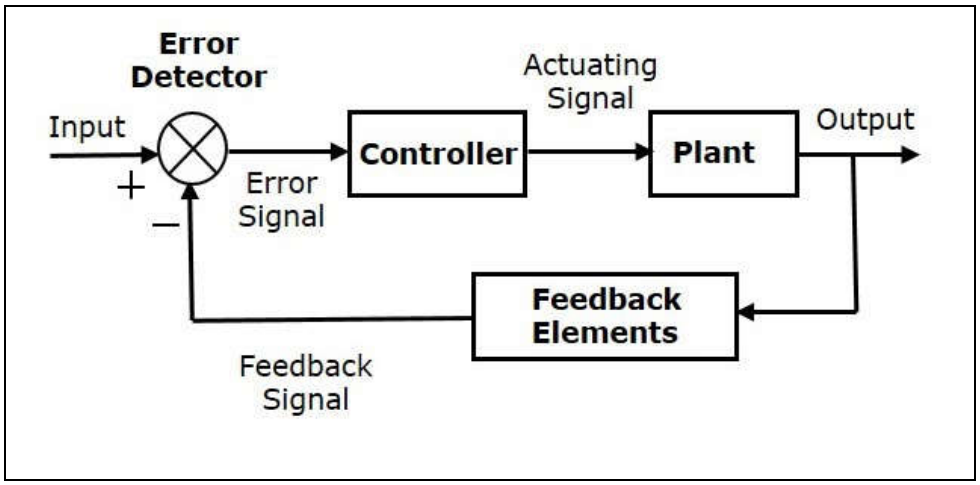

Figure 6.6 Diagram of the feedback system. Plant: system to be controlled. Controller: Provides the excitement of the plant; It is designed to control the behavior of the entire system.

The transfer function of the PID controller is expressed as:

$$K_p + \frac{K_i}{S} + K_d s = \frac{K_d s^2 + K_p S + K_i}{S} \tag{6.20}$$

To determine the parameters of the PID controller in a closed loop system as shown in figure 6.3, the following variables must be taken into account: $E(s)$ represents the tracking error, which is the difference between the desired value input $R(s)$, and the actual output $Y(s)$. This error signal $E(s)$ is sent to the PID controller where its derivative and integral functions are computed. The signal $u(t)$ that represents the output of the controller is given by the sum of three terms, i.e. proportional, integral and derivative terms with respectively the gains K_p, K_i and K_d , as shown by the following relation:

$$u(t) = K_p e + K_i \int e dt + K_d \frac{de}{dt} \tag{6.21}$$

The signal $U(s)$ is then sent to the plant, and the new output $Y(s)$ is obtained and fed back to compute the new error signal $E(s)$, in order to make it tend to zero.

In the first three sections of this chapter, the main theoretical concepts necessary to design and implement,by simulation, the control of the PARE process were introduced. The regulatory control was first introduced, followed by the presentation of the feedback system and how to model and identify them. Finally, the PID controller was conceptually defined. In the next section, the control simulation of the PARE process is presented.

6.4 Control simulation of Plasma Assisted Reactive Evaporation process

In this section, a control simulation within Simulink of the optimal operating conditions of the PARE process obtained in Chapter 5 is presented. The zinc flow and oxygen flow control loops are simulated using a RC control architecture designed in this section. Figure 6.7 shows a schematic representation of the control loop. In order to introduce the feed mixture in ideal proportions, the ratio of the flow rates (Zn/O_2) should be 1.9:13. The Zn flow rate is considered to be the disturbance. Note that the ratio station is merely a device with an adjustable gain. The input signal to the ratio station is d_m, the measured Zn flow rate. Its output signal u_{sp} serves as the set point for the O_2 flow control loop. It is calculated as $u_{sp} = K_d d_m$. From Eq. 6.1, it follows that the desired ratio is $R_d = u/d = 6.84$.

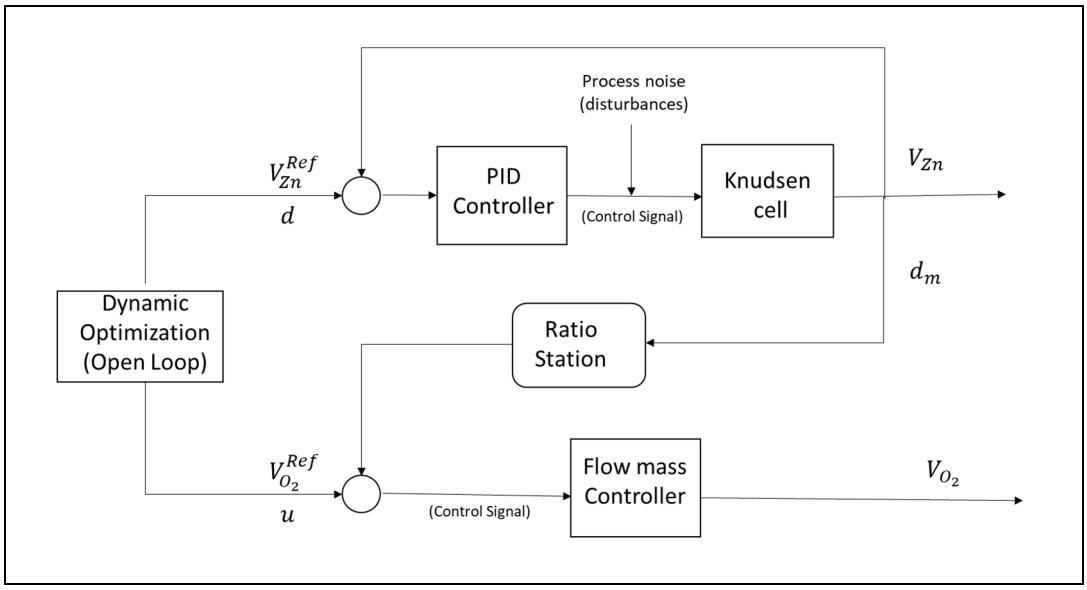

Figure 6.7 : Schematic representation of the simulation RC control of the of Plasma Assisted Reactive Evaporation process.

The schematic diagram of the pilot reactor to grow ZnO thin films by plasma assisted reactive evaporation was presented in Figure 2.6. It shows that the Zn flow feed is a result of evaporation of Zn using a Knudsen cell whereby there is a direct relation between Zn flow rate and Knudsen cell temperature. In order to identify

the characteristics of the Knudsen cell system (first or second order, stabilization time), an open-loop step signal was applied to the variable we want to control (Zn flow/Knudsen cell temperature). A constant voltage of 35 Vdc and a constant current of 5 Amp were applied and the system response is presented in Figure 6.8.

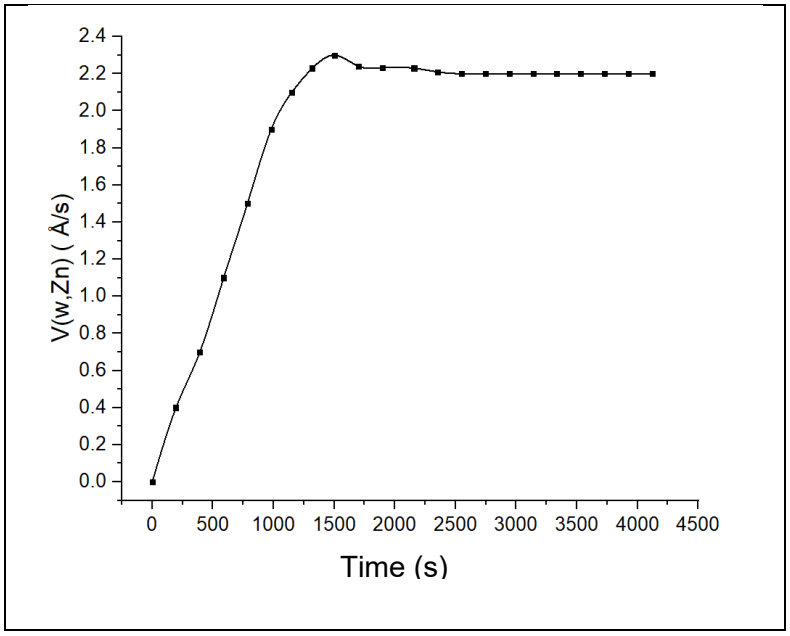

Figure 6.8 Knudsen cell open-loop response.

It can be seen that the response of the system is of first order for which the transfer function is determined using equations 6.8 and 6.9.

$$G(s) = \frac{0.45Å/Amp}{688.6s+1} \tag{6.22}$$

Nominal case

In the nominal, the advance regulatory control is simulated with the scheme presented in figure 6.7. The closed-loop profiles of the Zn flow rate, oxygen flow rate and Knudsen current are shown in Figures 6.9a, 6.9b and 6.9c, respectively. It can be seen that advanced regulatory control with a PI implementation achieves very good performances. It was used PI instead of PID controller due that the fact that the Knudsen cell system has a response of first order.

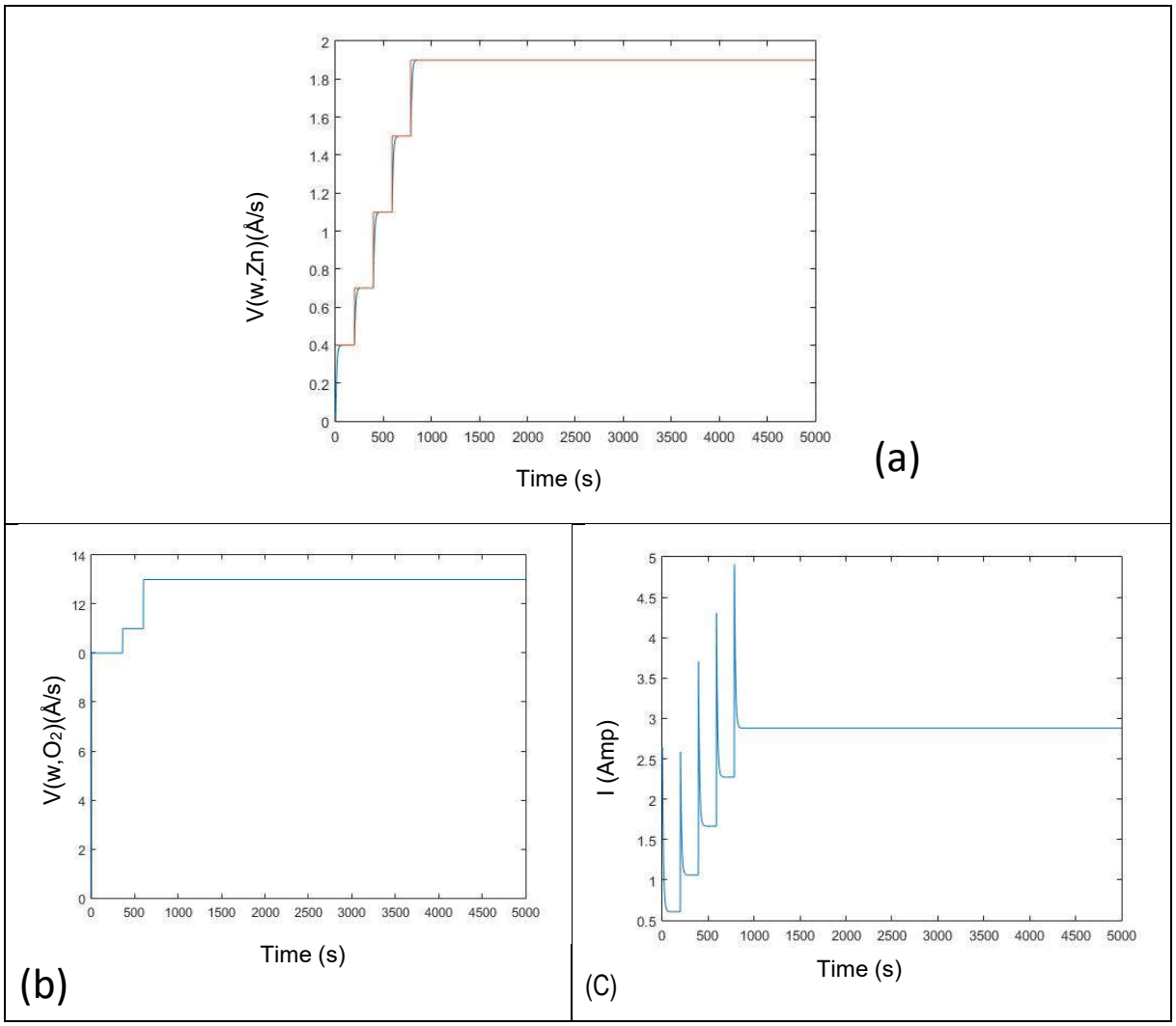

Figure 6.9 (a) Zn flow rate control : Zn flow set point in orange (optimal profile) and Zn flow rate reactor values in blue, (b) Optimal oxygen flow rate (c) Manipulated variable (current of the Knudsen cell).

Robustness with sublimation error

Robustness tests are carried out to check the control law performance under significant changes in the Zn flow. This is done by adding a disturbance in the closed-loop simulation. More specifically, it is assumed that the Knudsen cell undergoes an abrupt sublimation of Zn flow gas thus increasing the Zn flow rate by 10% compared with its actual value. The disturbed Zn flow (Figure 6.10a) is very rapidly corrected by means of the manipulated variable. The corresponding changes in the oxygen flow rate and in the current of Knudsen cell are shown in Figures 6.10b and 6.10c respectively.

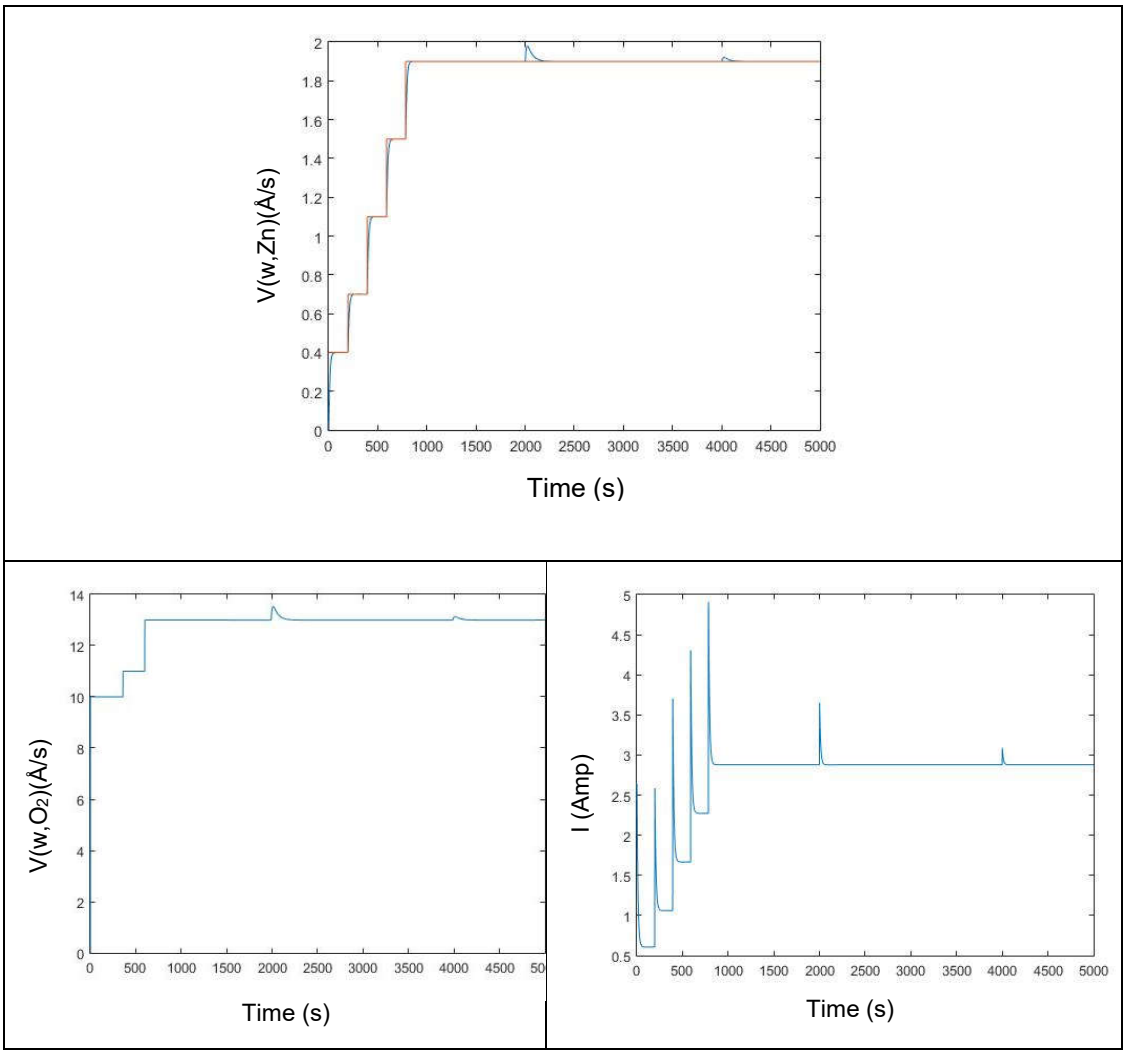

Figure 6.10 (a) Zn flow rate control : Zn flow set point in orange (optimal profile) and Zn flow rate reactor values in blue, with 10% of disturbance load (b) Flow rate of oxygen affected by the disturbance, (c) Manipulated variable (current of the Knudsen cell).

A regulatory control was designed to follow the Zn flow rate in the Plasma Assisted Reactive Evaporation reactor in spite of a possible disturbance such as Knudsen cell sublimation. After the simulation in the nominal case and verification of the controller performances by the robustness test, it can be concluded that the regulatory control is an adequate strategy to control the PARE process used in the semiconductor materials and solar energy group in order to improve the process productivity and ZnO thin film quality. The optimal Zn flow and Oxygen flow profiles, that were obtained in dynamic optimization studies were used as the set points for the regulatory control and the results show that the controller designed is appropriate to track the optimal Zn and oxygen flow keeping the ideal ratio previously calculated.

Chapter 7
Conclusions and perspectives

The present work was motivated by the idea to improve a pilot reactor based on Plasma Assisted Reactive Evaporation (PARE) process. More specifically, the objectives were to minimize the operating costs and improve the quality and productivity of the pilot. The methodology adopted to reach these objectives was based on :

(i) the development of a first principles dynamic model of the PARE process,

(ii) the validation of the model by means of experimental measurements,

(iii) the formulation and resolution of appropriate dynamic optimization problem using the process model,

(iv) the design of a suitable control law to track, in a closed-loop, the optimal profiles provided by dynamic optimization and used as set-point trajectories.

1. Conclusions

The first part of the work was thus devoted to the modelling of the PARE process. The model developed is based on transient charge, momentum and mass balances taking into account diffusion, convection and bulk and surface reactions in isothermal conditions. The objective is to determine the space-time varying of the concentration of the species ($O_{2(g)}$, $O_{(g)}^{\cdot}$, $O_{(g)}^{-}$, $Zn_{(g)}$, $Zn_{(g)}^{+}$ and $ZnO_{(g)}$) present throughout the reactor and compute the final zinc oxide film thickness. The model was simulated within Matlab® using finite difference method. The simulation results were compared to those obtained using COMSOL Multyphisics software. The comparison shows a very good agreement validating hence the finite difference method. The latter were used in the rest of the work since it offers more flexibility in dynamic optimization and control of the process.

The simulation results obtained were then corroborated by the experimental measurements of the ZnO film thickness carried out using a thickness monitor. The comparison between the model predictions and the simulation results exhibits a very good agreement. Furthermore, the simulation tool developed allowed also to

compute the film thickness as a function of the deposition time. The results obtained were satisfactory and allowed us to use that model in the rest of the research. On the other hand, an experimental characterization of the opto-electrical properties of the ZnO thin films were carried out. They showed that that both Zn-flow and O_2-flow affect Zn^+/O^- ratio which is directly associated with oxygen vacancies and has an impact in the opto-electrical properties. Moreover, in all the experimental results, it was observed that there is an ideal value of the Zn^+/O^- ratio which is obtained by properly selecting the values of Zn-flow and O_2-flow. Furthermore, by programming the deposition system following an optimal deposition routine, it was possible to grow highly transparent ZnO films with resistivities less than 10^{-3} Ωcm and transmittance greater than 85%.

The results obtained in the modelling and experimentation of the process were then used in the definition of dynamic optimization and control problems. Two different optimization scenarios were then formulated using Zn and oxygen flow rates decision variables. In both cases, the objective was to minimize the batch time (i.e. maximize productivity). A reduction of 15% in the batch time was achieved with respect to the normal operating conditions used by the semiconductor materials and solar energy research group. In the first scenario only Zn flow rate was considered as a decision variable, keeping constant the oxygen flow rate as the process was normally operated in the semiconductor materials and solar energy research group. In the second optimization problem, the oxygen flow rate was added as the second decision variable. In both cases, the optimization results show that the best way to reduce the batch time while keeping the ideal properties of the thin film is to operate at constant Zn flow rate with the highest possible value. This could be explained by the fact that the model does not include the transmittance and resistivity of the thin films as state variables.

Finally, a regulatory control architecture for the process was simulated. This control strategy was able to track the optimal profiles of oxygen and zinc flow rates keeping into account the ideal Zn/O ratio, and to reject the Zn flow disturbances. More generally, it is important to point out that the control of Plasma Assisted Reactive Evaporation process was a challenging task because of the complexity of the physico-chemical phenomena involved, and to the difficulties related to the availability of hardware sensors to provide on-line measurements of the end-used thin film properties. The performances of the controller were satisfactory for tracking the set-point trajectories provided by dynamic optimization and capable to keep the ideal value of oxygen to zinc ratio in spite of possible disturbances present in the Knudsen cell such as Zn sublimation.

2. Further works

As mentioned above, the optimal way to run the PARE process is to operate at the highest constant value of Zn flow rate since the transmittance and resistivity of the thin films were not included in the model as state variables. For this reason, in future works, we recommend to consider them in order to have additional

constraints that depend of these state variables. This will certainly allow to compute new operating strategies in a short time and with less required experiments.

On the other hand, one of the most obvious work outlook to carry out is to experimentally implement the designed control law. This implementation will allow to validate the dynamic optimization results as well as the regulatory controller. Furthermore, it would be more interesting to develop a dynamic real-time optimization (DRTO) method in order to simultaneously optimize and track the optimal profiles by means of a non-linear model predictive control (NMPC) approach. The DRTO will avoid the two-step approach of dynamic optimization and control which may not stay optimal when disturbances are involved.

8. References

[1] D.A. Miranda. Breve descripción de celdas fotovoltaicas de mono unión y de banda intermedia, Universidad Industrial de Santander. (2009)

[2] M. A. Rodríguez, J.L. Cervantes. El efecto fotoeléctrico. Redalyc. 13, núm. 3, 303–311 (2006).

[3] Ohl. R. S., US Patent 2402662

[4] Chapin, D. M., Fuller, C. S. and Pearson, G. L. 1954. A new silicon p-n junction hotocell for converting solar radiation into electrical power, J. Appl. Phys. 25, 676. (1954).

[5] Wolf. M. Limitations and possibilities for improvement of photovoltaic solar energy converters. Proc. IRE 48, 1246. (1960).

[6]W.Shockley, and H. Queisser. Detailed balance limit of efficiency of p-n junction solar cells. J. Appl. Phys., 32, 510. (1961).

[7] T. Tiedje, E.Yablonovitch, D. Cody y Bonnie G. Limiting efficiency of silicon solar cells, IEEE Trans. Electron Dev. 31, No 5, p711. (1984).

[8] A.Martí, and G.Araujo. Limitting efficiencies for photovoltaic energy conversion in multigap systems. Solar Energy Materials and Solar Cells, 43 (2), 203, (1996).

[9] A. Luque, and A. Martí. Increasing the efficiency of ideal solar cells by photon induced transitions at intermediate levels. Phys. Rev. Lett. 78, 5014, (1997)

[10] Woo Hyeon Jo, Dooho Choi, Optimization of ZnO/Ag/ZnO Transparent Conductive Electrodes Fabricated by Magnetron Sputtering, Korean Journal of Metals and Materials 57(2), (2019), 91-96.

[11] Zohra N. Kayani, Iqra Shah, Bareera Zulfiqar Aneeqa Sabah, Structural, Optical and Magnetic Properties of Nanocrystalline Co-Doped ZnO Thin Films Grown by Sol–Gel, Zeitschrift fur Naturforschung (2017), 73(1), DOI:10.1515/zna-2017-0302.

[12] David Winarski, Farida Seim, Synthesis of Conductive Sol-Gel ZnO Films and Development of ZnO Printed Electronics,intechopen, (2019) DOI: 10.5772/intechopen.82041

[13] Byeong RyongLee, Ji SooGoo, Yong Woon Kim, Young-JunYou, Sang-Kwon Lee, Jae Won Shim, Tae GeunKim, Highly efficient flexible organic photovoltaics using quasi-amorphous ZnO/Ag/ZnO transparent electrodes for indoor applications, Journal of Power Sources, 417, (2019), 61-69, DOI: 10.1016/j.jpowsour.2019.02.015

[14] M.M.Islama, S. Ishizuka, A. Yamada, K. Matsubara, S. Niki, T. Sakurai, K. Akimoto, Thickness study of Al:ZnO film for application as a window layer in Cu(In1−xGax)Se2 thin film solar cell, Applied Surface Science. 257, (2011), 4026–4030.

[15] Hakan Karaagac, Mehmet Parlak, Emre Yengel, M. Saif Islam, Heterojunction solar cells with integrated Si and ZnO nanowires and a chalcopyrite thin film, Materials Chemistry and Physics, 140, (2013), 382–390, DOI: 10.1016/j.matchemphys.2013.03.053

[16] D. Aaron R. Barkhouse, Oki Gunawan, Tayfun Gokmen, Teodor K. Todorov and David B. Mitzi,Device characteristics of a 10.1% hydrazine-processedCu2ZnSn(Se,S)4 solar cell, Prog. Photovolt: Res. Appl. 20, (2012) 6–11.

[17] Jing-Jing Dong, Jian Wu, Hui-Ying Hao, Jie Xing, Hao Liu, Hua Gao, Synthesis of ZnO Nanocrystals and Application in Inverted Polymer Solar Cells, Nanoscale Research Letters, 12, (2017), 529, DOI: 10.1186/s11671-017-2283-6

[18] Ju Won Lima, Do Kyung Hwanga , Keun Yong Limb , Mingi Kangc , Sang-Chul Shinc , Hyun-Seok Kimc, Won Kook Choib , Jae Won Shimc, ZnO-morphology-dependent effects on the photovoltaic performance for inverted polymer solar cells, Solar Energy Materials and Solar Cells 169, (2017), 28–32, DOI: 10.1016/j.solmat.2017.04.046
[19] Youngjun Kim, Byoungnam Park, Understanding Charge Trapping/Detrapping at the Zinc Oxide (ZnO)/MAPbI3 Perovskite Interface in the Dark and Under Illumination Using a ZnO/Perovskite/ZnO Test Platform, Nanoscale 10, (2018), 6194, DOI: 10.1039/C8NR06820H
[20] Heng Liu, Xingwang Zhang, Liuqi Zhang, Zhigang Yin, Denggui Wang, Junhua Meng, Qi Jiang, Ye Wang, Jingbi You , A high-performance photodetector based on an inorganic perovskite–ZnO heterostructure, Journal of Materials Chemistry C 5(25), (2017), DOI: 10.1039/C7TC01998J
[21] R. Menner, D. Hariskos, V. Linss, M. Powalla, Low-cost ZnO:Al transparent contact by reactive rotatable magnetron sputtering for Cu(In,Ga)Se2 solar modules, Thin Solid Films, 519, (2011) 7541–7544.
[22] C. H. Chen, Y. C. Chen, S. F. Hong, C. L. Wang, W. C. Shih, Room-temperature fabrication of highly transparent conductive aluminum-doped zinc oxide films, proc. 35th IEEE photovoltaic Specialist Conf., Hawaii, (2010) 2413.
[23] M. Kauk, K. Muska, M. Altosaar, M. Danilson, K. Õunpuu, T. Varema and O. Volobujeva, ZnO grown by chemical solution deposition, proc. 35th IEEE photovoltaic Specialist Conf., Hawaii (2010) 2452.
[24] Shafinaz Sobihana Shariffudin, Sukreen Hana Herman, Mohamad Rusop, Self-Catalyzed Thermal Chemical Vapor Deposited ZnO Nanotetrapods, Advance Materials Research, 832, (2013), 670-674, DOI: 10.4028/www.scientific.net/AMR.832.670
[25] N.R More, U.B Chanshett, Review Article on ZnO thin films by Spray Pyrolysis, International Journal of Chemical and Physical Sciences, (2018), 51-54.
[26] Tatyana Ivanova, A Harizanova, Anna Petrova Petrova, Morphological and optical investigation of Sol-Gel ZnO films, Journal of Physics Conference Series, 700, (2017), DOI: 10.1088/1742-6596/700/1/012047
[27] T Magorian Friedlmeier, Philip Jackson, Andreas Bauer, Dimitrios Hariskos, Oliver Kiowski, Roland Wuerz, and Michael Powalla, Improved Photocurrent in Cu(In,Ga)Se2 Solar Cells:From 20.8% to 21.7% Efficiency with CdS Buffer and 21.0% Cd-Free, IEEE Journal of photovoltaics, 5, (2015), 1487-1491.
[28] Gerardo Gordillo , Asdrubal Antonio Ramirez Botero, Edwin Alexander Ramirez, Development of novel control system to grow ZnO thin films by reactive evaporation, J mater res technol. 5, (2016) 219–225.
[29] Christofides, P.D., Armaou, A., 2006. Control and optimization of multiscale processsystems. Comput. Chem. Eng. 30, 1670–1686.
[30] S. Rasoulian, L.A. Ricardez-Sandoval. A robust nonlinear model predictive controller for a multiscale thin film deposition process Chemical Engineering Science 136 (2015) 38–49
[31] Mc ginn. D, et al. Renewables 2013 global status report 2013. (2013).
[32] J. Zhao, A. Wang and M.A. Green, Prog. In Photovoltaics, 2 (1994)227
[33] K. Saito et al., J. Non Cryst. Solids, Vols. 164-166(1993)689.
[34] D.E. Carlson et al., J. Materals Research, Vol.13(10) 2754 , (1998)
[35] X. Wu, Proc. 17th European PV Solar Energy Conf., Munich 995, (2001)
[36] B. Dimmler, M. Powala and H.W. Schock, Progres in Photovoltaics, Res. Appl., Vol.10149, (2002)
[37] M. Powala, et al. Proc. 29th IEEE PV Specialist Conf., New Orleáns 571, (2001)
[38] U. Rau and H.W.Schock, Appl. Phys. A, Vol.69, 191, (1999)
[39] Delbos, S. Këster ite thin films for photovoltaics: a review. EPJ Photovoltaics 3, 35004 (2012).
[40] A. Weber et al. Multi-stage evaporation of Cu_2ZnSnS_4 thin films, Thin Solid Films 517, 2524-2526, (2009)
[41] Di Giacomo, F., Razza, S., Matteocci, F., D'Epifanio, A., Licoccia, S., Brown, T. M., & Di Carlo, A.. High efficiency CH3NH3PbI(3−x)Clx perovskite solar cells with poly(3-hexylthiophene) hole transport layer. Journal of Power Sources, 251, 152–156. doi:10.1016/j.jpowsour.2013.11.053, (2014)
[42] Boix, P. P., Nonomura, K., Mathews, N., & Mhaisalkar, S. G. Current progress and future perspectives for organic/inorganic perovskite solar cells. Materials Today, 17(1), 16–23. doi:10.1016/j.mattod.2013.12.002, (2014).
[43] M.S. Ryu, H.J. Cha and J. Jang. Improvement of operation lifetime for conjugated polymer:fullerene organic solar cells by introducing a UV absorbing film. Solar Energy materials and Solar Cells, (2012)

[44] C.J. Brabec, V. Diakonov, J. Parisi and N.S. Sariciftci. Organic photovoltaicsa: concepts and realization. Vol. 60, Springer, Berlin, Germany, (2003).
[45] NREL2019
[46] https://www.ossila.com/pages/perovskites-and-perovskite-solar-cells-an-introduction
[47] https://www.sciencedirect.com/search/advanced?qs=ZnO%20photovoltaics&show=25&sortBy=relevance
[48] K. Ellmer, A. Klein, B. Rech, "Transparent conductive Zinc Oxide", ISBN 978-3-540-73611-0 Springer Berlin Heidelberg New York, (2008)
[49] Hadis Morkoç and Ümit Özgür, "Zinc Oxide Fundamentals, Materials and Device Technology" ISBN 978-3-527-40813-9 WILEY-VCH Verlag GmbH & Co. KGaA,Weinheim, (2009)
[50] Faÿ, S., Steinhauser, J., Nicolay, S., & Ballif, C. Polycrystalline ZnO: B grown by LPCVD as TCO for thin film silicon solar cells. Thin Solid Films, 518(11), 2961–2966. doi:10.1016/j.tsf.2009.09.189, (2010).
[51] Lee, C.-H., & Kim, D.-W. Thickness dependence of microstructure and properties of ZnO thin films deposited by metal-organic chemical vapor deposition using ultrasonic nebulization. Thin Solid Films, 546, 38–41. doi:10.1016/j.tsf.2013.05.029, (2013).
[52] Shirazi, M., Hosseinnejad, M. T., Zendehnam, a., Ghorannevis, Z., & Ghoranneviss, M.. Deposition of ZnO multilayer on LiNbO3 single crystals by DC-magnetron sputtering. Applied Surface Science, 257(23), 10233–10238. doi:10.1016/j.apsusc.2011.07.027 (2011)
[53] K. Ellmer, R. Wendt, R. Cebulla, ZnO/ZnO: Al window and contact layer for thin film solar cells: high rate deposition by simultaneous RF and DC magnetron sputtering, Proceedings of the XXVth IEEE PV Specialist Conference, Washington, D.C., May, (1996) 881
[54] H. Spanggaard, F.C. Krebs, Solar Energy Materials & Solar Cells 83 (2004) 125–146
[55] Cephas E. Small, et al., Adv. Energy Mater. (2012).
[56] Yong-JinNoh, Seok-InNa, Seok-SoonKim. Inverted polymer solar cells including ZnO electron transport layer fabricated by facile spray pyrolysis, Solar Energy Materials & Solar Cells. (2013)
[57] Von Engel A. Electric plasmas their nature and uses. NewYork: Taylor and Francis Ltd.; 1983.
[58] S. Rasoulian, L.A. Ricardez-Sandoval. A robust nonlinear model predictive controller for a multiscale thin film deposition process Chemical Engineering Science 136 (2015) 38–49
[59] Antonios Armaou, Panagiotis D. Christofides, Plasma enhanced chemical vapor deposition: Modeling and control Chemical Engineering Science 54 (1999) 3305-3314
[60] J.van Deelen, A. Illiberi, B. Kniknie, E.H.A. Beckers, P.J.P.M. Simons, A. Lankhorst. Atmospheric pressure chemical vapor deposition of ZnO: Process modeling and experiments, Thin solid Films, Vol 555, 163-168
[61] T. M. Barnes, J. Leaf, C. Fry, C. A. Wolden, Room temperature chemical vapor deposition of c-axis ZnO, Journal of Crystal Growth 274 (2005) 412-417
[62] Antonios Armaou, Panagiotis D. Christofides, Plasma enhanced chemical vapor deposition: Modeling and control Chemical Engineering Science, 54, (1999), 3305-3314.
[63] J.van Deelen, A.Illiberi, B.Kniknie, E.H.A.Beckers, P.J.P.M.Simons, A.Lankhorst, Atmospheric pressure chemical vapor deposition of ZnO: Process modeling and experiments, Thin Solid Films, 555, (2014), 163-168
[64] Chen, X., et al., Vapor Pressure Characterization of Several Phenolics and Polyhydric Compounds by Knudsen Effusion Method. J. Chem. Eng. Data, 51, (2006), 386-391.
[65] Jin He, Yuantao T Zhang, Modeling Study on the Generation of Reactive Oxygen Species in Atmospheric, Plasma Process. Polym. Radio-Frequency Helium–Oxygen Discharges. 9, (2012)n 919–928.
[66] S. V. Berezhnoj, C. B. Shin, U. Buddemeier and I. Kaganovich. Charged species profiles in oxygen plasma, Appl. Phys. Lett. 77, (2000), 6
[67] Colin A. Wolden, The Role of Oxygen Dissociation in Plasma Enhanced Chemical Vapor Deposition of Zinc Oxide from Oxygen and Diethyl Zinc, Plasma Chemistry and Plasma Processing, 25, (2005), DOI: 10.1007/s11090-004-8841-6
[68] Jin He, Yuantao T Zhang, Modeling Study on the Generation of Reactive Oxygen Species in Atmospheric, Plasma Process. Polym. 9, (2012), 919–928

[69] Geraldo Roberson, Marisa Roberto, John Verboncoeur, and Patrick Verdonck, Global Model Simulations of Low-Pressure Oxygen Discharges, Brazilian Journal of Physics, 37, (2007)
[70] Mark Davis, Finite Difference Methods, Department of Mathematics Imperial College London, 2011
[71] W. Vallejo, tesis de maestría "desarrollo de materiales fotovoltaicos usados como ventana óptica en celdas solares. Universidad nacional de Colombia, Bogotá (2011).
[72] H. E. Bennett, J. M. Bennett, Precision measurements in thin film optics, Physics of Thin Films, Vol: 4, pp. 1-96, 1967.
[73] L. Ward, The Optical Constants of Bulk Materials and films, 1994.
[74], Malte Ruben Vogt Development of Physical Models for the Simulation of Optical Properties of Solar Cell Modules Thesis for: PhD, 2015
[75] L. Biegler. An overview of simultaneous strategies for dynamic optimization. Chemical Engineering and Processing, 46 :1043–1053, 2007..
[76] A. Cervantes and L. T. Biegler. Optimization strategies for dynamic systems, Encyclopedia of Optimization, pages 216–227. Springer, Second edition, October 2008.
[77] J. P. Corriou. Commande des Proc´ed´es. Lavoisier, Tec. & Doc., Paris, France, 2nd edition, 2003.
[78] R. Paulen, M. Fikar, and M. A. Latifi. Dynamic optimization of a polymerization reactorIn 18th Mediterranean Conference on Control & Automation, Congress Palace Hotel, Marrakech, Morocco, 2010a
[79] S. R. Upreti. Optimal control for chemical engineers. CRC Press, Boca Raton, Florida, 2012.
[80] D. N. Burghes and A. Graham. Introduction to Control Theory including Optimal Control. Ellis Horwoood Limited, Chichester, England, 1980
[81] B. Chachuat, A. B. Singer, and P. I. Barton. Global methods for dynamic optimization and mixed-integer dynamic optimization. Ind. Eng. Chem. Res., 45 :8373–8392, 2006.
[82] S. Kameswaran and L. T. Biegler. Simultaneous dynamic optimization strategies : recent advances and challenges. Comp. Chem. Engng., 30 :1560–1575, 2006
[83] A. E. Bryson. Dynamic Optimization. Addison-Wesley Longman, Inc, Menlo Park, California, USA, 1999.
[84] L. Biegler, A. M. Cervantes, and A. W¨ achter. Advances in simultaneous strategies for dynamic process optimization. Chemical Engineering Science, 57 :575–593, 2002.
[85] W. Hong, S. Wang, P. Li, G. Wozny, and L. T. Biegler. A quasi-sequential approach o large-scale dynamic optimization problems. AIChE Journal, 52 :255–268, 2006.
[86] C. J. Goh and K. L. Teo. Control parametrization : a unified approach to optimal control problems with general constraints. Automatica, 24 :3–18, 1988.
[87] P. Araujo and R. Giudici. Optimization of semicontinuous emulsion polymerization reactions by IDP procedure with variable time intervals. Comp. Chem. Engng, 27 : 1345–1360, 2003.
[88] A. Flores, S. Terrazas, and L. T. Biegler. Global optimization of highly nonlinear dynamic systems. Ind. Eng. Chem. Res., 47 :2643–2655, 2008.
[89] R. Russell Rhinehart, *Advanced regulatory control (ARC) or advanced process control (APC)?*. Distributed with permission of author by ISA 2010 Presented at ISA Automation Week; 5-7 October 2010;
[90] Harold L. Wade, Basic and Advance Regulatory Control, Third Edition, Isa, 2017, ISBN: 978-0-87664-013-5
[91] Iván López Moreda, Dinámica y Control de Procesos, Consulted February 2019 https://www.fing.edu.uy/iq/cursos/dcp/teorico/18_OTROS_SISTEMAS_DE_CONTROL.pdf
[92] Dorf, Richard C. ; Bishop, Robert H.: Modern control systems. 12th. Prentice Hall : Pearson, 2010. {xxi, 1082 p. p.
[93] Golnaraghi, M. F. ; Kuo, Benjamin C.: Automatic control systems. 9th. Hoboken, NJ : Wiley, 2010. 786 p. p.
[94] Ogata, Katsuhiko: Modern control engineering. 5th. Boston : Prentice-Hall, 2010 (Prentice-Hall electrical engineering series Instrumentation and controls series) x, 894 p. p.